Alma Mater Studiorum - Università di Bologna

DIPARTIMENTO DI INGEGNERIA DELLE COSTRUZIONI MECCANICHE, NUCLEARI, AERONAUTICHE E DI METALLURGIA

Corso di Dottorato di Ricerca in Meccanica Applicata

Ciclo XXI

Settore Scientifico ING-IND/13

Numerical and analytical vibro-acoustic modelling of porous materials: the Cell Method for poroelasticity and the case of inclusions

Autore:
Marco Seppi

Coordinatore:
Ch.mo Prof. Vincenzo Parenti Castelli

Tutore:
Ch.mo Prof. Giorgio Dalpiaz

Esame finale anno 2009

Abstract

Porous materials are widely used in many fields of industrial applications, to achieve the requirements of noise reduction, that nowadays derive from strict regulations.

The modeling of porous materials is still a problematic issue. Numerical simulations are often problematic in case of real complex geometries, especially in terms of computational times and convergence. At the same time, analytical models, even if partly limited by restrictive simplificative hypotheses, represent a powerful instrument to capture quickly the physics of the problem and general trends.

In this context, a recently developed numerical method, called the Cell Method, is described, is presented in the case of the Biot's theory and applied for representative cases. The peculiarity of the Cell Method is that it allows for a direct algebraic and geometrical discretization of the field equations, without any reduction to a weak integral form. Then, the second part of the thesis presents the case of interaction between two poroelastic materials under the context of double porosity. The idea of using periodically repeated inclusions of a second porous material into a layer composed by an original material is described. In particular, the problem is addressed considering the efficiency of the analytical method. A analytical procedure for the simulation of heterogeneous layers based is described and validated considering both conditions of absorption and transmission; a comparison with the available numerical methods is performed.

Abstract

I materiali porosi sono ampiamente utilizzati per diverse applicazioni industriali, al fine di raggiungere gli obiettivi di riduzione del rumore, che sono resi impegnativi da norme al giorno d'oggi sempre più stringenti.

La modellazione dei materiali porori per applicazioni vibro-acustiche rapprensenta un aspetto di una certa complessità. Le simulazioni numeriche sono spesso problematiche quando siano coinvolte geometrie di pezzi reali, in particolare riguardo i tempi computazionali e la convergenza. Allo stesso tempo, i modelli analitici, anche se parzialmente limitati a causa di ipotesi semplificative che ne restringono l'ambito di utilizzo, rappresentano uno strumento molto utile per comprendere rapidamente la fisica del problema e individuare tendenze generali.

In questo contesto, un metodo numerico recentemente sviluppato, il Metodo delle Celle, viene descritto, implementato nel caso della teoria di Biot per la poroelasticità e applicato a casi rappresentativi. La peculiarità del Metodo delle Celle consiste nella discretizzazione diretta algebrica e geometrica delle equazioni di campo, senza alcuna riduzione a forme integrali deboli. Successivamente, nella seconda parte della tesi viene presentato il caso delle interazioni tra due materiali poroelastici a contatto, nel contesto dei materiali a doppia porosità. Viene descritta l'idea di utilizzare inclusioni periodicamente ripetute di un secondo materiale poroso all'interno di un layer a sua volta poroso. In particolare, il problema è studiando il metodo analitico e la sua efficienza. Una procedura analitica per il calcolo di strati eterogenei di materiale viene descritta e validata considerando sia condizioni di assorbimento, sia di trasmissione; viene effettuata una comparazione con i metodi numerici a disposizione.

Acknowledgements

I am very grateful to Dr. Giuseppe Miccoli from Imamoter Institute (Ferrara, Italy), where I have spent most of my time, who has primarily allowed and supported my activities and the realization of the present work, and to the Imamoter director, Prof. Gianluca Zarotti. Many thanks go to Prof. Giorgio Dalpiaz and to Prof. Vincenzo Parenti Castelli, for their valuable support during the course of the studies.

I am very grateful to Dr. Claudio Bertolini from Rieter Automotive, that inspired and assisted an extensive part of this work, for his patience and good mood during our discussions, and to Prof. Emmanuel Gourdon, who inspired and assisted as well and gave me warm hospitality and support during the pleasant period I have spent in France, at Entpe. I thank Prof. Emmanuel Gourdon and Prof. Kiril Horoshenkov who have been very kind to help me with their feedback and checking of my work.

I would like to thank Prof. Enzo Tonti for the discussions at the initial stage of the present work and in particular Prof. Luigi Bregant, whose help and advices I always consider very precious, both in technical and extra-technical matters.

Last but not least I thank all the researchers, students, assistants that I have met in the several academic institutions where I have been just for a visit or for longer spans of time, who have enriched me and with whom, through pleasant company, discussions and talks, I have shared an intense and rewarding research period.

Contents

1 Introduction

Porous materials are widely used in many fields of industrial applications, to achieve the requirements of noise reduction, that nowadays derive from strict regulations.

Different types of materials are used: felts, foams, granular materials, conglomerations (for example conglomerations of other recycled materials). The physical description that these materials have in common is driven by the presence of two phases: a solid phase, called frame, and a fluid phase inside the pores, the fluid being air for the common vibro-acoustic applications. The interaction between the two phases is responsible for phenomena of absorption and attenuation. Beyond the complexity of the materials, inborn in their biphasic configuration, the various configurations and shapes that they assume and often the presence of a complete vibro-acoustic environment of which the material is a subsystem, let easily picture out the difficulties of providing reliable engineering predictions.

1.1 Background

The modeling of this kind of systems still requires a big effort, in particular when the models are expected to describe properly the systems used for real applications. Different aspects have to be taken into account.

Many theoretical models are available to predict the physical behaviour of porous materials. Empirical and theoretical models have been developed over the years, leading to the investigation and definition of a number of parameters. The most complex models require the definition of more than ten parameters to model the physical system of a porous absorbing material, built up of a network of pores and characterized by the interaction between its the solid and its fluid parts. It is the case, for example, of the Biot's theory of poroelasticity, that allows to take into account the mechanical properties of the material, simultaneously to its acoustical behavior, provided by the

model of Johnson-Champoux-Allard. Moreover, in some cases an even larger number of parameters would be necessary to model the system. For example when anisotropy is considered, even for the simpler situation of transverse anisotropy, theoretical models require the knowledge of additional parameters, as the elastic moduli in the transverse directions.

Each of the parameters that are present in the different theoretical models, has a specific physical meaning, however it is clear that a complex model is complex to be manipulated. Moreover, some of the parameters are very difficult to measure. For example, the direct measurement of parameters like the characteristic lengths represents in most cases an academic topic and for common applications indirect characterization techniques are often used. In general, the measurements of all the necessary parameters, that constitute the first step in the construction of a reliable model, represent by themselves a specific issue.

In this context, analytical and numerical models are used to simulate real systems. Numerical methods, like Finite Element Methods (FEM) provide a powerful instrument to predict the behavior of layers or multilayers of porous materials, characterized by various shapes; the prediction should be done possibly in the context of real applications, like for example the interior volume of a car.

However, the description given here shows how the key issue is represented by the complexity of numerical FE models for porous materials, especially when poroelasticity is concerned. Several works underline mainly two problematic aspects: the computational time and the convergence rate. Both represent critical parameters that still restrict the practical use of numerical methods in this field. Nevertheless, analytical models are much faster when computational time is concerned, but are limited by simplificative hypotheses.

1.2 Research objectives

Considering the described background, the present work rises under two different points of view. At first, a recently developed numerical method, called the Cell Method, is described, is presented in the case of the Biot's theory and applied for representative cases. The study aims at the definition of the method for the specific case of poroelastic materials, pointing out the characteristics, advantages and disadvantages of the method.

The peculiarity of the Cell Method is that it allows for a direct algebraic and geometrical discretization of the field equations, without any reduction to a weak integral form. The consequent conceptual simplification provides, in general, a simplification of the implementation in comparison to classical Finite Element Methods, with advantages that will be described in the present document. Essentially, the research is oriented to explore a more efficient way to solve the numerical problem in the case of Biot's theory.

Secondly, it can be observed that numerical methods are necessary when real diversified geometries are concerned. However, numerical elements are time consuming and simulation methods based on the analytical description of simplificative cases, like for example the Transfer Matrix Method, represent often a valuable help for a first framing of the problem. Often in practice, simulations are limited to the use of analytical methods. The present work addresses the problem of the interaction between two poroelastic materials under the context of double porosity. The idea of including periodical repetitions of a second porous material into a layer composed by an original material is described. In particular, the problem is addressed considering the efficiency of the analytical method. A analytical procedure for the simulation of heterogeneous layers based on restrictive hypotheses is described; its validation and comparison to numerical methods represent a key aspect of the present study.

In summary, the research work carried out in this context aims at investigating numerical and analytical methods useful to simplify and fasten the simulation of specific cases of application in the context of porous materials for vibro-acoustic applications.

1.3 Overview of the thesis

Chapter 1.4 provides an overview of the most important theoretical aspects and the references that are recalled in the following chapters, as far as the vibro-acoustic modeling of porous materials is concerned. After this preliminary chapter, the present work is divided mainly in two parts. Chapter 2 and 3 are devoted to the application of the Cell Method to the case of Biot acoustic materials. The Cell Method is presented at first in its generalities, then the interpretation of the Tonti diagram for the specific case under study is given. Two kind of elements are presented: linear and quadratic tetrahedra. The Method is validated against theoretical models, for the case of a layer infinitely extended in the in-plane directions.

The peculiar theoretical association of variables to the algebraic and geometric elements is twofold. From one side, the Tonti diagram represents the natural chassis that sustains the numerical implementation of the Method. Secondly, a rigorous description of the links between the parameters involved in the theoretical model, is helpful to clarify the physical relations and classifications. In the context described above, simplicity can be seen as an important issue to provide efficient numerical methods.

Chapter 3 describes one of the key issues of the Cell Method: the management of boundary and interface conditions, that are in most cases treated naturally and quite easily, if compared to the case of Finite Elements. In particular, the case of an interface between two poroelastic materials is presented and validated against theoretical models, for the case of a layer infinitely extended in the in-plane directions.

The second part of the present work describes the analytical method for the calculation of layers of porous materials characterized by porous inclusions and presents in detail its application. The advantages expected by using the configuration with inclusions are described and verified experimentally; the analytical method is then validated against measurements for the case of sound absorption. A comparison between experimental, analytical and numerical results is given, highlighting the different hypotheses that are assumed for the different methods and discussing advantages and disadvantages. Chapter 6 extends the model of Chapter 4 to the case of sound transmission. The extended analytical model is described and validated against experiments.

General conclusions are given in Chapter 7.

1.4 Recall of the main theoretical aspects

The present Section recalls the theoretical concepts that are used in the following parts of the thesis. More details can be found in the bibliographic references.

Many authors have developed empirical and theoretical models to describe the vibroacoustics of porous materials. The different models involve physical parameters, relying mainly on experimental measurements or on theoretical definitions.

1.4.1 Acoustical and mechanical parameters

Among the mechanical parameters, two elastic constants are used to characterize the structural behavior, for example the *Young's modulus* E and the *Poisson's ratio* ν (or equivalently the *shear modulus* N and the Poisson's ratio). In addition, the structural frame density ρ_1 and the structural loss factor η are necessary for a complete description of the solid phase.

Among the acoustical parameters, the *open porosity* is defined is the fraction of air volume in the pores of the considered material and can assume values between 0 and 1 (for common acoustic materials it is in most of the cases above 0.95):

$$\phi = \frac{V_f}{V_{tot}}. \tag{1.1}$$

The *airflow resistivity* is a measure of the resistance that the air flow encounters when crossing the material:

$$\sigma = \frac{\Delta P}{Vd} \tag{1.2}$$

where ΔP is the pressure difference, V is the mean flow of air per unit area of the material and d is the thickness of the material. The *tortuosity* is a geometrical parameter that takes into account the sinuosity of the pores and hence is linked to the inertial coupling between the solid and fluid phase. The tortuosity can be equal or greater than 1 and is equal to 1 in the case of parallel cylindrical pores oriented in the direction of propagation. In general, the tortuosity is theoretically defined as the ratio between the microscopic kinetic energy of the fluid particle and the macroscopic kinetic energy of a perfect fluid moving into the pores:

$$\alpha_\infty = \frac{< v^2 >}{< v >^2} \tag{1.3}$$

where $<>$ is the average operator. At the end, the *viscous characteristic length* is related to viscous effects at high frequency and is linked to the minimum size of the pores, while the *thermal characteristic length* is related to thermal exchanges at high frequency and is linked to the maximum size of the pores.

1.4.2 Theoretical models

In general, three different kinds of porous materials can be distinguished. The most general theoretical model is based on Biot's theory of poroelasticity and takes into account the interactions between the solid and fluid phases of the medium (Section 1.4.3).

When the frame of the porous medium can be assumed to be motionless, a reduction to a rigid frame model can be used. If an acoustic excitation acts on a constrained and rigid, heavy solid frame or if the solid-fluid coupling is negligible for the elastic frame, only the acoustic compression wave propagates in the medium, that can be described as an equivalent rigid frame fluid medium. The following Helmoltz equation can be written in this case:

$$\frac{1}{\omega^2 \rho_{eq}} \nabla^2 p + \frac{1}{K_{eq}} p = 0 \tag{1.4}$$

involving the equivalent dynamical density ρ_{eq} and the equivalent bulk modulus K_{eq}.

If the structural frame has no bulk stiffness, i.e. in the case of elastic "soft" materials, the density of the air can be modified to take into account the inertia effect of the solid phase. It is the case of a limp material and, as for the rigid frame model, only the acoustic compression wave exists.

1.4.3 Biot's theory

Let us consider an open-cell porous medium, made up of an elastic solid phase (the frame) and a fluid phase. The Biot's theory states that three waves propagate simultaneously in the medium: two compressional waves (one elastic and one acoustic wave) and an elastic shear wave. In the original work of Biot [8], two sets of equations are combined together to obtain the wave equations for the poroelastic material. A set of 6 Lagrangian coordinates is defined: the six displacement components of the solid phase and the fluid phase (u_x^s, u_y^s, u_z^s, u_x^f, u_y^f and u_z^f). Only macroscopic average displacements and deformations are considered; i.e. the quantities involved are not defined at the microscopic scale but are locally averaged.

At first the stress tensor is defined; for an homogeneous and isotropic material it reads:

$$[\sigma] = \begin{bmatrix} \sigma^s \\ \sigma^f \end{bmatrix} = \begin{bmatrix} \mathbf{E}^{ss} & \mathbf{E}^{sf} \\ \mathbf{E}^{fs} & \mathbf{E}^{ff} \end{bmatrix} \begin{bmatrix} \varepsilon^s \\ \varepsilon^f \end{bmatrix} = \begin{bmatrix} \mathbf{E} \end{bmatrix} \begin{bmatrix} \varepsilon \end{bmatrix} \tag{1.5}$$

where $[\sigma^s] = \begin{bmatrix} \sigma_x^s & \sigma_y^s & \sigma_z^s & \tau_{xy}^s & \tau_{yz}^s & \tau_{zx}^s \end{bmatrix}^\mathsf{T}$ and $[\sigma^f] = \begin{bmatrix} \sigma_x^f & \sigma_y^f & \sigma_z^f & \tau_{xy}^f & \tau_{yz}^f & \tau_{zx}^f \end{bmatrix}^\mathsf{T}$ are the components of the solid and fluid stress tensors, $[\varepsilon^s] = \begin{bmatrix} \epsilon_x^s & \epsilon_y^s & \epsilon_z^s & \gamma_{xy}^s & \gamma_{yz}^s & \gamma_{zx}^s \end{bmatrix}^\mathsf{T}$ and $[\varepsilon^f] = \begin{bmatrix} \epsilon_x^f & \epsilon_y^f & \epsilon_z^f & \gamma_{xy}^f & \gamma_{yz}^f & \gamma_{zx}^f \end{bmatrix}^\mathsf{T}$ are the solid and fluid deformations, and the following elastic matrices are involved:

$$\begin{bmatrix} \mathbf{E}^{ss} \end{bmatrix} = \begin{bmatrix} 2N+A & A & A & 0 & 0 & 0 \\ A & 2N+A & A & 0 & 0 & 0 \\ A & A & 2N+A & 0 & 0 & 0 \\ 0 & 0 & 0 & N & 0 & 0 \\ 0 & 0 & 0 & 0 & N & 0 \\ 0 & 0 & 0 & 0 & 0 & N \end{bmatrix} \tag{1.6}$$

$$\begin{bmatrix} \mathbf{E}^{sf} \end{bmatrix} = \begin{bmatrix} \mathbf{E}^{fs} \end{bmatrix} = \begin{bmatrix} Q & Q & Q & 0 & 0 & 0 \\ Q & Q & Q & 0 & 0 & 0 \\ Q & Q & Q & 0 & 0 & 0 \\ 0 & 0 & 0 & 0 & 0 & 0 \\ 0 & 0 & 0 & 0 & 0 & 0 \\ 0 & 0 & 0 & 0 & 0 & 0 \end{bmatrix} \qquad \begin{bmatrix} \mathbf{E}^{ff} \end{bmatrix} = \begin{bmatrix} R & R & R & 0 & 0 & 0 \\ R & R & R & 0 & 0 & 0 \\ R & R & R & 0 & 0 & 0 \\ 0 & 0 & 0 & 0 & 0 & 0 \\ 0 & 0 & 0 & 0 & 0 & 0 \\ 0 & 0 & 0 & 0 & 0 & 0 \end{bmatrix}.$$

The parameters A, N, Q, R are elastic parameters that take into account the solid elastic behavior of the medium and the coupling between the solid and elastic phase. They are linked to the solid Lamé constants, to the solid and fluid bulk modulus and to the medium porosity. A detailed description is given in [1].

Secondly, the mechanical behavior is considered by Biot. The kinetic energy is defined as

$$T = \sum_{\xi=x,y,z} \left[\frac{1}{2}\rho_{11}\left(\frac{\partial u_\xi^s}{\partial t}\right)^2 + \rho_{12}\frac{\partial u_\xi^s}{\partial t}\frac{\partial u_\xi^f}{\partial t} + \frac{1}{2}\rho_{22}\left(\frac{\partial u_\xi^f}{\partial t}\right)^2 \right] \tag{1.7}$$

and a dissipation function, taking into account viscous effects, is introduced:

$$D = \frac{1}{2} b \sum_{\xi=x,y,z} \left(\frac{\partial u_\xi^s}{\partial t} - \frac{\partial u_\xi^f}{\partial t} \right)^2. \tag{1.8}$$

Lagrange's equation are formalized for the dynamics of the system:

$$\begin{aligned} \frac{\partial}{\partial t}\left(\frac{\partial T}{\partial v_x^s}\right) + \frac{\partial D}{\partial v_x^s} &= q_x^s \\ \frac{\partial}{\partial t}\left(\frac{\partial T}{\partial v_x^f}\right) + \frac{\partial D}{\partial v_x^f} &= q_x^f \end{aligned} \tag{1.9}$$

considering the total forces q_x^s and q_x^f acting on the solid and fluid volume (i.e. elastic forces). Equation 1.9 is similarly written for the y and z coordinates. In this way, the dynamic equations are given:

$$\begin{aligned} \frac{\partial \sigma_x^s}{\partial x} + \frac{\partial \tau_{xy}^s}{\partial y} + \frac{\partial \tau_{zx}^s}{\partial z} &= \frac{\partial^2(\rho_{11} u_x^s + \rho_{12} u_x^f)}{\partial t^2} + b\frac{\partial(u_x^s - u_x^f)}{\partial t} \\ \frac{\partial \sigma_x^f}{\partial x} &= \frac{\partial^2(\rho_{12} u_x^s + \rho_{22} u_x^f)}{\partial t^2} - b\frac{\partial(u_x^s - u_x^f)}{\partial t} \end{aligned} \tag{1.10}$$

with corresponding expressions for the y and z coordinates. Bringing together elastic and dynamic equations, the general expressions for waves propagation are derived:

$$\begin{aligned} N\nabla^2\mathbf{u}^s + \nabla\left[(A+N)\nabla{\cdot}\mathbf{u}^s + Q\nabla{\cdot}\mathbf{u}^f\right] &= \frac{\partial^2(\rho_{11}\mathbf{u}^s + \rho_{12}\mathbf{u}^f)}{\partial t^2} + b\frac{\partial(\mathbf{u}^s - \mathbf{u}^f)}{\partial t} \\ \nabla\left[Q\nabla{\cdot}\mathbf{u}^s + R\nabla{\cdot}\mathbf{u}^f\right] &= \frac{\partial^2(\rho_{12}\mathbf{u}^s + \rho_{22}\mathbf{u}^f)}{\partial t^2} - b\frac{\partial(\mathbf{u}^s - \mathbf{u}^f)}{\partial t} \end{aligned} \tag{1.11}$$

The equations recalled here for the Biot's theory are considered in Chapter 2.2.1 and analyzed for the case of the Cell Method.

2 The Cell Method for Biot's theory of poroelasticity

The Finite Elements Method has been extensively used to solve vibro-acoustic problems involving poroelastic materials [5, 22, 44]. In the literature, two basic sets of FE formulations for poroelastic materials can be found: the first one (the so-called *(u-U)* formulation) makes use of the displacements of the solid and of the fluid phase of the porous material as basic variables, following the original developments of Biot [8]. The second one (the so called "mixed" or *(u-p)* formulation) describes the fluid phase of the porous material by means of its acoustic pressure field. Several successful works have been published about the application of these FE implementations to coupled structure-fluid systems [21], that show how such implementations can properly model, in most cases at least, the physical behaviour of poroelastic materials. Nevertheless, some issues still remain concerning their convergence rate [26, 27, 47] and the computational effort that is in any case needed for their application. Both these issues have limited, so far, the application of these FE implementations to industrial cases, for which very few works have been published [7, 58].

The Cell Method (CM) is a numerical method based on a direct discretization of the field conservation and constitutive equations, without any reduction to a weak integral form. Instead of variational operations, simple algebraic and direct operations are used to get a solution of the physical problem at hand. The method was developed by Tonti [53, 54, 55] and has already been successfully applied to several engineering fields. In [53, 54, 55] the method is presented in his entireness. Linear metric triangular and tetrahedral elements are presented, with reference to acoustics [53] and electromagnetism [55]. In [54] a quadratic discretization for a bi-dimensional case is used too.

Some theoretical aspects of the method and in general discussions about algebraic topology with reference to numerical methods are presented in [38], [25] and [15]. The method has been applied to several electromagnetic problems ([55], [25], [15], [56]) and

elasticity problems ([16], [19], [42]). The group of Zovatto have investigated two important issues of the Cell Method: the convergence aspects ([32]) and the extension of the method to natural meshless grids ([59], [33], [51]).

The big advantage, compared to FE Methods, is noted in the direct physical and therefore easier implementation, which allows also a much better understanding of the physical meaning of the quantities that are involved in the implementation itself. For large systems, the combination of those aspects leads to a more efficient numerical calculation, in some cases in terms of computational times and in general in terms of simplicity. Furthermore, some literature papers [59] seem to indicate how the CM over performs FEM as far as the convergence rate is concerned and is also a good candidate for mesh less numerical applications.

All these aspects led to the research work presented here that basically consists in an implementation of Biot's equations by means of the CM, with the final purpose of analyzing its advantages/disadvantages compared to classical FEM, for what concerns in particular implementation procedure and convergence rates.

2.1 Review of the Cell Method

The aim of the Cell Method is to provide a discretization of the field equations starting only from considerations in the finite domain. In fact, the passage to continuum implies the use of variational operators, that lead to differential equations that cannot be solved on generic domains. Classical Finite Methods act on the differential equations to obtain an approximate finite discretization. With the Cell Method instead, the physical equations are obtained directly in a finite form starting from experimental laws without resorting to the differential formulation. For this reason, global (i.e. integral) quantities are sistematically used.

The peculiarities of the Cell Method can be summarized as follows.

- Two *cell complexes* are defined: a primal complex and a dual complex (Fig. 2.1), that express the geometry of the system and result to be interconnected; an analogous duality applies to the time domain also. The principle of duality states that each element in the primal complex is associated to an element in the dual complex. For geometrical elements in the tri-dimensional case, if the primal elements

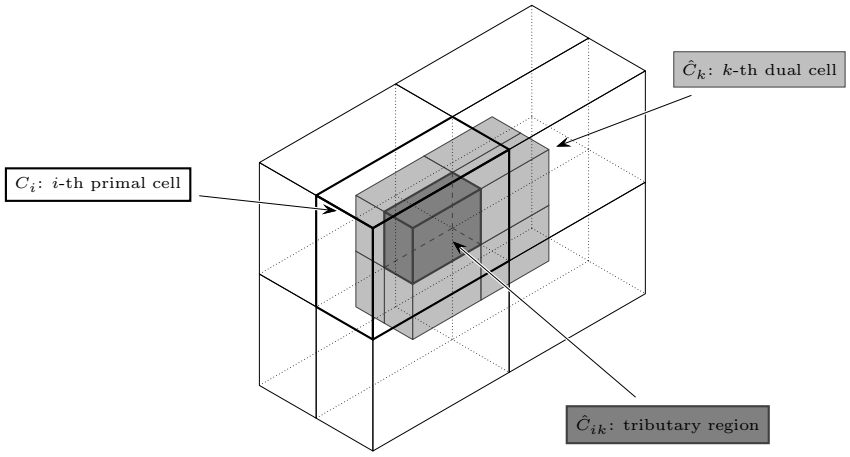

Figure 2.1: Primal and dual cell complexes

are indicated by P, L, S, V (point, line, surface, volume) and the dual elements by $\tilde{P}$, $\tilde{L}$, $\tilde{S}$, $\tilde{V}$, the following associations hold: $P \leftrightarrow \tilde{V}$, $L \leftrightarrow \tilde{S}$, $S \leftrightarrow \tilde{L}$, $V \leftrightarrow \tilde{P}$.

- Physical quantities can be divided in 3 sets: configuration, source and energetic variables. Configuration variables express a configuration of the system (displacement, velocity, strain), source variables express sources of the field (force, momentum). Relations between configurations variables only and between source variables only are topological equations and do not contain physical constants. Physical constant are contained into constitutive or phenomenological equations, that relate configuration variables to source variables and can be tipically verified through experiments. Energetic variables express the energy of the system in its forms, and are given by the product of a configuration variable and a source variable.

- Physical quantities are associated to geometric elements and time elements. The geometrical association is crucial in the case that will be considered. Configuration variables are associated to the primal complex and source variables to the dual complex. Each variable is then associated to its characteristic geometrical element, not only on points, like in the usual differential formulation. For example, in the tridimensional case, displacements and velocities are associated to points, strains to lines (in the primal complex); forces are associated to volumes, stresses to surfaces (in the dual complex).

The result of these considerations is the Tonti diagram, that will be described in detail in 2.2.1 for the case of Biot's theory. The Tonti diagram is a representation of a physical theory through the physical quantities that are involved. Starting from the considera-

tions above, each variable occupies a specific place in the Tonti diagram. Variables are represented by boxes and equations by lines. For each box, a spatial and a time element is defined. Two sides of the diagram are separated: the configuration and the source variables. The lines connecting a variable in the left side with a variable in the right side are constitutive equations. In this way, for example, the displacement is represented in a box in the "primal side" of the diagram, referred to points and instants; the force is represented in a box in the "dual side" of the diagram, referred to volumes and intervals. In each floor of the diagram the reference to a spatial element is fixed. In this way, a very general frame can be created, where boxes are referred to all the possible spatial and time elements. Each physical theory fills part of this diagram with the interested quantities.

Starting from the Tonti diagram, it is possible to solve the field equations in a direct discrete way. In fact, phenomenological equations do not imply the use of differential operators; topological relations between configurations variables only and between source variables only can be expressed in a discrete shape. For example, the gradient of a quantity can be calculated in an algebraic way, as the difference of two values with reference to a distance.

Similarly to Finite Methods, unknowns are defined on a set of points called nodes. The geometrical domain is divided into elements (primal cells) to which nodes are associated. For example, displacements are defined on nodes of the primal complex and forces on volumes of the dual complex. In this configuration, primal cells act as elements and the dual cells act as control volumes for the solution of equations, for example to fix the balance of forces in a structural problem. A peculiarity of the Cell Method is that the solution can be obtained independently from the shape of the dual complex.

In the case of application of the Biot's theory, equations are written in the domain of frequency and a temporal dependency of the kind $e^{j\omega t}$ is assumed, thus the time association is not necessary. The Tonti diagram and Cell Method work in the same way. The only difference is in the relations that involve time operations: in that cases, variables are simply related through a factor $j\omega$.

2.2 Implementation of Biot's Equations with the Cell Method

In this Section, a numerical solution of Biot's Equations with the Cell Method is presented. At first, the Tonti diagram described in Section 2.1 is presented; then it is applied to write the equilibrium equations in a direct discrete form. At the end, the numerical solution is presented for 2 kind of elements: the linear metric tetrahedron and the quadratic metric tetrahedron.

2.2.1 Review of the Biot's theory according to Tonti diagram

The Biot's theory is here recalled from a different point of view, compared to the original presentation in [8]. As observed in Section 1.4.3, Biot starts from the stress-strain phenomenological relations (Eq. 1.5) and from the dynamic equations (Eq. 1.10) to obtain the waves equations (Eq. 1.11). In this derivation, three phenomenological assumptions are involved:

- the first is represented by the stress-strain relations (Eq. 1.5);
- the second is the relation that defines kinetic energy (Eq. 1.7);
- the third is the relation that defines dissipation (Eq. 1.8).

A direct discretization can be obtained instead, through the definition of primal and dual variables. In the case of Biot's theory, the configuration (primal) variables are the displacements and the quantities immediately (i.e. by simple operations) connected to the displacements: velocities and strains. The source (dual) variables are the forces and the quantities immediately connected: momenta and stresses.

The aim at this point, is to construct the Tonti diagram for the Biot's theory in the continuum, with reference to the differential formulation. In this way, we will obtain a meaning for each connection line between the physical quantities that are involved. Secondly, we will use the Tonti diagram in its discrete shape, i.e. when quantities are connected by discrete algebraic operations only in a finite domain.

Variables are first defined as in Section 1.4.3. Differently from the original Biot derivation, it is possible to obtain the waves equations (Eq. 1.11) starting from two different phenomenological assumption:

- the first is represented by the stress-strain relations (Eq. 1.5);
- the second is the phenomenological law for momentum;
- the third is the phenomenological law for dissipation.

The momentum is a dual quantity. The usual definition of momentum is mass times velocity. On the contrary, it is preferable to define the momentum of a particle as the impulse released by the particle in motion when it is stopped. In this way, the relation $\mathbf{p} = m\mathbf{v}$ is a phenomenological law, derived from experiments. In fact, with those definitions, momentum and velocity can be measured and the parameter m can be obtained through measurements.

It follows, for the Biot's theory, that momentum and velocity are bonded by the phenomenological law:

$$\mathbf{p} = [\rho] \cdot \mathbf{v} = \begin{bmatrix} \rho_{11} & \rho_{12} \\ \rho_{21} & \rho_{22} \end{bmatrix} \cdot \begin{bmatrix} [v^s] \\ [v^f] \end{bmatrix} \tag{2.1}$$

where $\mathbf{p}$ is a 6-component vector, $[v^s]$ and $[v^f]$ are 3-component vectors and, in the case of Biot's theory, $\rho_{21} = \rho_{12}$. Tonti [54] observes that energetic variables are always a product of a configuration variable by a source variable, as in case of kinetic energy (per volume unit) of a particle: $T = \int \mathbf{v} \cdot \mathrm{d}\mathbf{p} = \frac{1}{2}\rho v^2$ where $\mathbf{p} = \rho \cdot \mathbf{v}$. It is very easy to verify that the phenomenological law for momentum Eq. 2.1 gives the same result in term of kinetic energy (per volume unit) as Biot [8] obtains:

$$T = \int \mathbf{v} \cdot \mathrm{d}\mathbf{p} = \int \begin{bmatrix} [v^s] \\ [v^f] \end{bmatrix} \cdot \mathrm{d} \begin{bmatrix} \rho_{11}[v^s] + \rho_{12}[v^f] \\ \rho_{21}[v^s] + \rho_{22}[v^f] \end{bmatrix} =$$
$$= \frac{1}{2}\rho_{11}\left|[v^s]\right|^2 + \rho_{12}[v^s] \cdot [v^f] + \rho_{21}[v^f] \cdot [v^s] + \frac{1}{2}\rho_{22}\left|[v^f]\right|^2$$

where, in the case of Biot's theory, $\rho_{21} = \rho_{12}$.
Dissipation in this case can be directly defined as:

$$\mathbf{f} = \begin{bmatrix} [f^s] \\ [f^f] \end{bmatrix} = [B] \cdot \mathbf{v} = \begin{bmatrix} +b & -b \\ -b & +b \end{bmatrix} \cdot \begin{bmatrix} [v^s] \\ [v^f] \end{bmatrix} \tag{2.2}$$

bonding a source term (viscous force) to a configuration term (velocity).

Finally, quantities in the source part of Tonti diagram have to be balanced:

$$\nabla \cdot [\sigma] = \frac{\partial \mathbf{p}}{\partial t} + \mathbf{f} \qquad \text{with } [\sigma] = \begin{bmatrix} [\sigma^s] \\ [\sigma^f] \end{bmatrix} = \begin{bmatrix} \sigma_x^s & \tau_{xy}^s & \tau_{xy}^s \\ \tau_{yx}^s & \sigma_y^s & \tau_{yz}^s \\ \tau_{zx}^s & \tau_{zy}^s & \sigma_z^s \\ \sigma_x^f & \tau_{xy}^f & \tau_{xy}^f \\ \tau_{yx}^f & \sigma_y^f & \tau_{yz}^f \\ \tau_{zx}^f & \tau_{zy}^f & \sigma_z^f \end{bmatrix} \tag{2.3}$$

that corresponds to the equation of momentum balance. Applying Eq. 2.3 to the x-coordinate of the solid phase:

$$\nabla \cdot [\sigma^s]_x = \nabla \cdot \begin{bmatrix} \sigma_x^s & \tau_{xy}^s & \tau_{xz}^s \end{bmatrix} = \frac{\partial}{\partial t} [p_x^s] + [f_x^s] \Rightarrow$$
$$\Rightarrow \frac{\partial}{\partial x} (\sigma_x^s) + \frac{\partial}{\partial x} (\tau_{xy}^s) + \frac{\partial}{\partial x} (\tau_{xz}^s) = \frac{\partial}{\partial t} \left(\rho_{11} v_x^s + \rho_{12} v_x^f\right) + b \left(v_x^s - v_x^f\right)$$

to the x-coordinate of the fluid phase:

$$\nabla \cdot [\sigma^f]_x = \nabla \cdot \begin{bmatrix} \sigma_x^f & \tau_{xy}^f & \tau_{xz}^f \end{bmatrix} = \frac{\partial}{\partial t} [p_x^f] + [f_x^f] \Rightarrow$$
$$\Rightarrow \frac{\partial}{\partial x} (\sigma_x^f) + 0 + 0 = \frac{\partial}{\partial t} \left(\rho_{21} v_x^s + \rho_{22} v_x^f\right) - b \left(v_x^s - v_x^f\right)$$

and, with analogous derivations, to the remaining 2 solid and 2 fluid coordinates, Eq. 1.10 is obtained. At the end, it is sufficient to insert the stress-strain relations Eq. 1.5 to get the original shape of the waves equations Eq. 1.11.

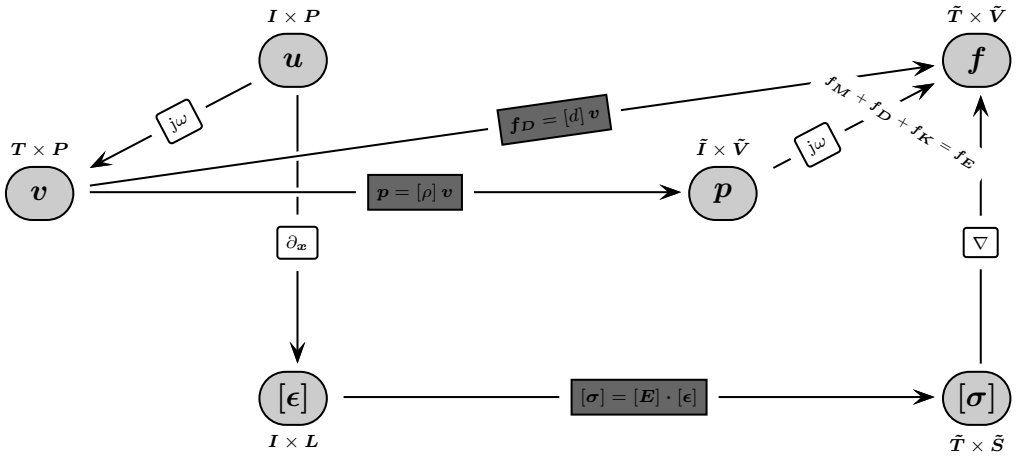

Figure 2.2: Tonti diagram for the Biot's theory

For the case of Biot's theory, the distribution of variables into Tonti diagram is thus verified and is represented in Fig. 2.2. Tonti diagram can now be used in its discrete shape. This means that we will use algebraic operations only, directly on a discrete domain, to fix relations between physical quantities and to obtain the equilibrium equations that solve the system.

2.2.2 Equilibrium equations

According to Tonti diagram (Fig. 2.2), the equilibrium of the source terms (forces) has to be guaranteed. Three terms must be included:

- stiffness force;
- damping force;
- inertial force.

In the Cell Method, when solving the system of physical equations, it is only required to satisfy the equilibrium equations, written in a discrete form. This fact represent a peculiarity of the method. The equilibrium must be satisfied for every dual cell. In fact, the sources (forces) are referred to the right part of the diagram, that contains the dual variables. The principle is that *if equilibrium is guaranteed on a domain, it is also satisfied on every subdomain, provided that the former is contained in the union of all tributary regions* [33]. In our case, the dual cells are not overlapping and the union of all tributary regions (i.e. dual cells) corresponds exactly to the entire domain.

Let i be the global index for the generic primal cell C_i, k the global index for the generic dual cell D_k, $\mathcal{P}$ the set of all the primal cells of the domain, $\mathcal{D}$ the set of all the dual cells of the domain and $\mathcal{P}_k$ the set of primal cells to which the k-th node belongs. All the forces acting on the generic k-th dual cell must be taken into account. They are related to the tributary regions (portions of primal cells) that constitute the generic dual cell ($\hat{C}_{i,k}$, like for example in Fig. 2.1. The cell complexes are still generic and will be specified later. The forces related to $\hat{C}_{i,k}$ must be summed up for every generic $i \in \mathcal{P}_k$ and must be in equilibrium. Therefore, the equilibrium equation for the k-th dual cell is:

$$\sum_{i \in \mathcal{P}_k} (\mathbf{f}_{\mathbf{K}i,k} + \mathbf{f}_{\mathbf{D}i,k} + \mathbf{f}_{\mathbf{M}i,k} - \mathbf{f}_{\mathbf{E}i,k}) = 0, \quad \forall k \in \mathcal{D} \tag{2.4}$$

where $\mathbf{f_K}$ is the stiffness force, $\mathbf{f_D}$ the damping force, $\mathbf{f_M}$ the inertial force and $\mathbf{f_E}$ the sum of the external forces (for example due to the loading conditions), all being six-component forces vectors, acting on the three solid and the three fluid DOFs. As indicated in Eq. 2.4, these forces are calculated starting from the characteristics of the i-th primal cell (geometry, displacements, etc.) and are taken into account for the equilibrium of the k-th dual cell. The equilibrium equations must be valid for every dual cell belonging to $\mathcal{D}$.

2.2.3 Forces calculation

Given a primal and a dual complex, let us consider a primal cell indexed bi i. The shape of $\hat{C}_{i,k}$ depends on the element type and is described in the following Sections 2.2.4 and 2.2.5. If the focus is on the elementary matrix, the dual cell index changes from the global k to the local α. Some relations are independent from the shape of $\hat{C}_{i,\alpha}$ and are useful for the forces calculation.

Shape functions

Let $\mathbf{u}$ be the displacement vector in the i-th primal cell, discretized in an algebraic way depending on the shape of the element. However, some considerations are independent from the element type. The displacement can be expressed in terms of shape functions, as in the case of Finite Elements:

$$\mathbf{u} = \begin{bmatrix} u_x^s \\ u_y^s \\ u_z^s \\ u_x^f \\ u_y^f \\ u_z^f \end{bmatrix} = \left[\begin{array}{ccccccc|ccccccc} N_1 & 0 & 0 & \cdots & N_n & 0 & 0 & & & & & & & \\ 0 & N_1 & 0 & \cdots & 0 & N_n & 0 & & & & 0 & & & \\ 0 & 0 & N_1 & \cdots & 0 & 0 & N_n & & & & & & & \\ \hline & & & & & & & N_1 & 0 & 0 & \cdots & N_n & 0 & 0 \\ & & & 0 & & & & 0 & N_1 & 0 & \cdots & 0 & N_n & 0 \\ & & & & & & & 0 & 0 & N_1 & \cdots & 0 & 0 & N_n \end{array}\right] \cdot \begin{bmatrix} u_{x,1}^s \\ \vdots \\ u_{z,n}^s \\ u_{x,1}^f \\ \vdots \\ u_{z,n}^f \end{bmatrix} \tag{2.5}$$

where n denotes the number of the nodes in the specific element type and the generic displacement in the (primal) cell is given by the product of shape functions by the vector of displacements at the nodes.

Stiffness force

The stiffness force $\mathbf{f}_{\mathbf{K}_{i,\alpha}}^{ph}$ for a single phase ph, solid or fluid, can be expressed via the Cauchy Law in a discrete form. In fact, the relationship between the stress vector and the stress tensor can be written for a finite domain. The areas of $\hat{C}_{i,\alpha}$ must be considered, that are in contact with tributary regions of the primal i-th cell that belong to nodes different from α. These boundary internal areas will be called areas of influence for the node α. In the present derivation their shape is generic and is described in detail in the following Sections 2.2.4 and 2.2.5, depending on the element type. The areas of influence are indexed by $l(\alpha)$ and their cartesian components are indicated as $A_{l(\alpha),p}$ with $p = x, y, z$. The normal vector to the areas of influence will be indicated as $n_{l(\alpha)}$.

The stress vector is dual quantity, referred to a surface $l(\alpha)$, boundary of the tributary region contained in the primal i-th cell i. As well known:

$$\mathbf{t}_{i,l(\alpha)}^{ph} = \begin{bmatrix} t_x^{ph} \\ t_y^{ph} \\ t_z^{ph} \end{bmatrix}_{i,l(\alpha)} = \begin{bmatrix} n_x & 0 & 0 & n_y & 0 & n_z \\ 0 & n_y & 0 & n_x & n_z & 0 \\ 0 & 0 & n_z & 0 & n_y & n_x \end{bmatrix}_{i,l(\alpha)} \cdot \left[\sigma^{ph}\right]_{i,l(\alpha)} \tag{2.6}$$

where $[\sigma^{ph}]=[\sigma_x^{ph}\ \sigma_y^{ph}\ \sigma_z^{ph}\ \tau_{xy}^{ph}\ \tau_{yz}^{ph}\ \tau_{zx}^{ph}]^\mathsf{T}$. The stiffness force is obtained as the product of the stress vector by the area on which the stress acts. Since the stress vector can also not be constant, it has to be integrated on the area $l(\alpha)$ taken into consideration.

$$\mathbf{f}_{\mathbf{K}_{l(\alpha)}}^{ph} = \begin{bmatrix} f_{K,x}^{ph} \\ f_{K,y}^{ph} \\ f_{K,z}^{ph} \end{bmatrix}_{l(\alpha)} = \int_{A_l(\alpha)} \mathbf{t}_{l(\alpha)} \, \mathrm{d}A \tag{2.7}$$

Since $\mathbf{n}_{l(\alpha)} = \frac{\mathbf{A}_{l(\alpha)}}{\|\mathbf{A}_{l(\alpha)}\|}$, combining Eq. 2.6 and 2.7 we have:

$$\mathbf{f}_{\mathbf{K}_{l(\alpha)}}^{ph} = \left[\mathbf{B_1}\right]_{l(\alpha)} \cdot \frac{1}{\|\mathbf{A}_{l(\alpha)}\|} \int_{A_l(\alpha)} \left[\sigma^{ph}\right]_{l(\alpha)} \mathrm{d}A \tag{2.8}$$

where

$$\Big[\mathbf{B_1}\Big]_{l(\alpha)} = \begin{bmatrix} A_x & 0 & 0 & A_y & 0 & A_z \\ 0 & A_y & 0 & A_x & A_z & 0 \\ 0 & 0 & A_z & 0 & A_y & A_x \end{bmatrix}_{l(\alpha)} \tag{2.9}$$

The deformation vector in the primal i-th cell for a single solid or fluid phase ph can be obtained inserting Eq. 2.5 in the definition of deformation $\left(\varepsilon_{pq}=\frac{1}{2}\left(\frac{\partial u_p}{\partial q}+\frac{\partial u_q}{\partial p}\right)\right)$:

$$\varepsilon_i^{ph} = \begin{bmatrix} \varepsilon_x^{ph} \\ \varepsilon_y^{ph} \\ \varepsilon_z^{ph} \\ \gamma_{xy}^{ph} \\ \gamma_{yz}^{ph} \\ \gamma_{zx}^{ph} \end{bmatrix}_i = \begin{bmatrix} \frac{\partial N_1}{\partial x} & 0 & 0 & \cdots & \frac{\partial N_n}{\partial x} & 0 & 0 \\ 0 & \frac{\partial N_1}{\partial y} & 0 & \cdots & 0 & \frac{\partial N_n}{\partial y} & 0 \\ 0 & 0 & \frac{\partial N_1}{\partial z} & \cdots & 0 & 0 & \frac{\partial N_n}{\partial z} \\ \frac{\partial N_1}{\partial y} & \frac{\partial N_1}{\partial x} & 0 & \cdots & \frac{\partial N_n}{\partial y} & \frac{\partial N_n}{\partial x} & 0 \\ 0 & \frac{\partial N_1}{\partial z} & \frac{\partial N_1}{\partial y} & \cdots & 0 & \frac{\partial N_n}{\partial z} & \frac{\partial N_n}{\partial y} \\ \frac{\partial N_1}{\partial z} & 0 & \frac{\partial N_1}{\partial x} & \cdots & \frac{\partial N_n}{\partial z} & 0 & \frac{\partial N_n}{\partial x} \end{bmatrix}_i \begin{bmatrix} u_{x,1}^{ph} \\ \vdots \\ u_{z,n}^{ph} \end{bmatrix}_i = \Big[\mathbf{B_2}(x,y,z)\Big]_i \begin{bmatrix} u_{x,1}^{ph} \\ \vdots \\ u_{z,10}^{ph} \end{bmatrix}_i \tag{2.10}$$

where the matrix $\mathbf{B_2}$ is function of the spatial coordinates and will depend from the element type.

The stiffness force for a generic $\hat{C}_{i,\alpha}$, to be inserted in the equilibrium equations, is calculated as a sum of different contributions, coming from each boundary area of $\hat{C}_{i,\alpha}$. Combining Eq. 1.5, 2.8 and 2.10, considering both solid and fluid phases and summing up for all the areas of influence of $\hat{C}_{i,\alpha}$, the stiffness force acting on the tributary region $\hat{C}_{i,\alpha}$ is calculated in its 6 components:

$$\mathbf{f_{K}}_{i,\alpha} = \begin{bmatrix} f_{K_x}^s \\ f_{K_y}^s \\ f_{K_z}^s \\ f_{K_x}^f \\ f_{K_y}^f \\ f_{K_z}^f \end{bmatrix}_{i,\alpha} = \underbrace{\sum_{l(\alpha)=1}^{n_{tot}(\alpha)} \left(\begin{bmatrix} \Big[\mathbf{B_1}\Big]_{l(\alpha)} & \Big[0\Big] \\ \Big[0\Big] & \Big[\mathbf{B_1}\Big]_{l(\alpha)} \end{bmatrix}_i \cdot \Big[\mathbf{E}\Big]_i \cdot \frac{1}{\|\mathbf{A}_{l(\alpha)}\|} \int_{A_{l(\alpha)}} \begin{bmatrix} \Big[\mathbf{B_2}\Big]_{l(\alpha)} & \Big[0\Big] \\ \Big[0\Big] & \Big[\mathbf{B_2}\Big]_{l(\alpha)} \end{bmatrix}_i \mathrm{d}A \right)}_{\Big[K_{i,\alpha}\Big]} \cdot \begin{bmatrix} u_{x,1}^s \\ \vdots \\ u_{z,n}^s \\ u_{x,1}^f \\ \vdots \\ u_{z,n}^f \end{bmatrix} \tag{2.11}$$

where $\big[\mathbf{B_1}\big]_{l(\alpha)}$ is a 3×6 matrix depending on the boundary areas of $\hat{C}_{i,\alpha}$ only, $\big[\mathbf{E}\big]_i$ is a 12×12 matrix depending on the material characteristics in the i-th cell, $\big[\overline{\mathbf{B_2}}\big]_{l(\alpha)} =$

$\int_{A_l(\alpha)} [\mathbf{B_2}]_{l(\alpha)} \, \mathrm{d}A$ is a $6 \times 3n$ matrix depending on the shape of $\hat{C}_{i,\alpha}$ and on the shape functions. [1]

Damping and inertial forces

The phenomenological laws for damping and for momentum connect velocity, defined at a point of the primal complex, with the force, defined at a volume of the dual complex. Thus, damping and inertial forces derive from an integration of the phenomenological laws over the volume of the dual cell.
Considering that $\mathbf{v} = j\omega\mathbf{u}$, the damping force $\mathbf{f_D}_{i,\alpha}$ acting on the discrete volume $\hat{C}_{i,\alpha}$ is represented by:

$$\mathbf{f_D}_{i,\alpha} = \begin{bmatrix} f^s_{Dx} \\ f^s_{Dy} \\ f^s_{Dz} \\ f^f_{Dx} \\ f^f_{Dy} \\ f^f_{Dz} \end{bmatrix}_{i,\alpha} = \int_{\hat{C}_{i,\alpha}} j\omega \left[d\right]_{i,\alpha} \mathbf{u} \, \mathrm{d}V = j\omega \begin{bmatrix} +b & 0 & 0 & -b & 0 & 0 \\ 0 & +b & 0 & 0 & -b & 0 \\ 0 & 0 & +b & 0 & 0 & -b \\ -b & 0 & 0 & +b & 0 & 0 \\ 0 & -b & 0 & 0 & +b & 0 \\ 0 & 0 & -b & 0 & 0 & +b \end{bmatrix}_{i,\alpha} \cdot \int_{\hat{C}_{i,\alpha}} \begin{bmatrix} u^s_x \\ u^s_y \\ u^s_z \\ u^f_x \\ u^f_y \\ u^f_z \end{bmatrix} \mathrm{d}V \tag{2.12}$$

[1] Concerning this aspect, the following interesting observations can be found in [57]: *"There have been previous efforts in the literature in formulating consistent discrete theories of elasticity. As was mentioned earlier, an example is the so-called 'cell method', which is a numerical method that aims to formulate discrete problems ab-initio, i.e., without any reference to the corresponding continuum formulations. Cosmi [16], Ferretti [19], and Pani [42] extended Tonti's idea [54] for linear elasticity and defined the displacements on primal zero-cells and assumed that deformation is homogeneous within each primal two-cell (for a 2D elasticity problem). Then they associated a strain tensor to each primal two-cell. In other words, they enter a continuous elasticity quantity into the discrete formulation. In this sense, cell method cannot be considered as a geometric discretization of linearized elasticity. With the uniform strain in each primal two-cell, they assumed a uniform stress in each primal two-cell. This is again a direct use of a continuous concept and makes the method not a geometric discretization. In other words, this immediately contradicts the original idea of the cell method. The only geometric idea in the cell method is in writing the equilibrium equations on dual two cells."*

Similarly for the inertial force $\mathbf{f}_{\mathbf{M}i,\alpha}$, that takes into account the contribution of momentum as in the Tonti diagram, considering that $\frac{\partial \mathbf{p}}{\partial t} = j\omega\mathbf{p}$:

$$\mathbf{f}_{\mathbf{M}i,\alpha} = \begin{bmatrix} f^s_{Mx} \\ f^s_{My} \\ f^s_{Mz} \\ f^f_{Mx} \\ f^f_{My} \\ f^f_{Mz} \end{bmatrix}_{i,\alpha} = \int_{\hat{C}_{i,\alpha}} -\omega^2 \left[\rho\right]_{i,\alpha} \mathbf{u}\, \mathrm{d}V = -\omega^2 \begin{bmatrix} \rho_{11} & 0 & 0 & \rho_{12} & 0 & 0 \\ 0 & \rho_{11} & 0 & 0 & \rho_{12} & 0 \\ 0 & 0 & \rho_{11} & 0 & 0 & \rho_{12} \\ \rho_{12} & 0 & 0 & \rho_{22} & 0 & 0 \\ 0 & \rho_{12} & 0 & 0 & \rho_{22} & 0 \\ 0 & 0 & \rho_{12} & 0 & 0 & \rho_{22} \end{bmatrix}_{i,\alpha} \cdot \int_{\hat{C}_{i,\alpha}} \begin{bmatrix} u^s_x \\ u^s_y \\ u^s_z \\ u^f_x \\ u^f_y \\ u^f_z \end{bmatrix} \mathrm{d}V \tag{2.13}$$

The term $\overline{\mathbf{u}}_{\hat{C}_{i,\alpha}} = \int_{\hat{C}_{i,\alpha}} \left[u^s_x\ u^s_y\ u^s_z\ u^f_x\ u^f_y\ u^f_z\right]^{\mathsf{T}} \mathrm{d}V$ can be expressed using Eq. 2.5:

$$\overline{\mathbf{u}}_{\hat{C}_{i,\alpha}} = \underbrace{\left[\begin{array}{ccccccc|ccccccc} \bar{N}^{i,\alpha}_1 & 0 & 0 & \cdots & \bar{N}^{i,\alpha}_n & 0 & 0 & & & & & & & \\ 0 & \bar{N}^{i,\alpha}_1 & 0 & \cdots & 0 & \bar{N}^{i,\alpha}_n & 0 & & & & 0 & & & \\ 0 & 0 & \bar{N}^{i,\alpha}_1 & \cdots & 0 & 0 & \bar{N}^{i,\alpha}_n & & & & & & & \\ \hline & & & & & & & \bar{N}^{i,\alpha}_1 & 0 & 0 & \cdots & \bar{N}^{i,\alpha}_n & 0 & 0 \\ & & & 0 & & & & 0 & \bar{N}^{i,\alpha}_1 & 0 & \cdots & 0 & \bar{N}^{i,\alpha}_n & 0 \\ & & & & & & & 0 & 0 & \bar{N}^{i,\alpha}_1 & \cdots & 0 & 0 & \bar{N}^{i,\alpha}_n \end{array}\right]}_{\left[\bar{N}^{i,\alpha}\right]} \cdot \begin{bmatrix} u^s_{x,1} \\ \vdots \\ u^s_{z,n} \\ u^f_{x,1} \\ \vdots \\ u^f_{z,n} \end{bmatrix} \tag{2.14}$$

where the bar denotes the integral: $\bar{N}^{i,\alpha} = \int_{\hat{C}_{i,\alpha}} N^{i,\alpha}\, \mathrm{d}V$. The integration of the shape functions depend on the shape of the element and is described in Sections 2.2.4 and 2.2.5. In this way, the damping and inertial forces can be written as function of the vector containing the displacement components (both solid and fluid) of the i-th primal cell:

$$\mathbf{f}_{\mathbf{D}i,\alpha} = j\omega \left[d\right]_{i,\alpha} \cdot \left[\bar{N}^{i,\alpha}\right] \cdot \mathbf{u}_i \tag{2.15}$$

$$\mathbf{f}_{\mathbf{M}i,\alpha} = -\omega^2 \left[\rho\right]_{i,\alpha} \cdot \left[\bar{N}^{i,\alpha}\right] \cdot \mathbf{u}_i \tag{2.16}$$

where $\mathbf{u}_i = \left[u^s_{x,1} \cdots u^s_{z,n}\ u^f_{x,1} \cdots u^f_{z,n}\right]$ and we can define

$$\left[D_{i,\alpha}\right] = \left[d\right]_{i,\alpha} \cdot \left[\bar{N}^{i,\alpha}\right] \tag{2.17}$$

$$\left[M_{i,\alpha}\right] = \left[\rho\right]_{i,\alpha} \cdot \left[\bar{N}^{i,\alpha}\right] \tag{2.18}$$

as local matrices that will be used for the calculation of the elementary matrices (matrices of the element).

Elementary matrices

In Sections 2.2.3 and 2.2.3, the forces to be considered for equilibrium equations have been presented, with reference to a local tributary region $\hat{C}_{i,\alpha}$ constructed around the node α of the i-th primal cell. They have been expressed in function of the vector of displacements $\mathbf{u}_i$ of the i-th cell. The vector of displacements at nodes (i.e. points of the primal complex) contains the main primal variables and hence the unknowns of the problem.

With this notation, restoring the global index k, the matrices $\mathbf{K}_{i,k}$, $\mathbf{D}_{i,k}$ and $\mathbf{M}_{i,k}$ represent the link between $\mathbf{f_K}$, $\mathbf{f_D}$ and $\mathbf{f_M}$ respectively and the displacements vector $\mathbf{u}_i$. The matrices $\mathbf{K}_{i,k}$, $\mathbf{D}_{i,k}$ and $\mathbf{M}_{i,k}$ are part of the local elementary stiffness, damping and mass matrices, being the parts of the i-th primal cell elementary matrix whose components are referred to the tributary region $\hat{C}_{i,k}$. $\mathbf{K}_{i,k}$, $\mathbf{D}_{i,k}$ and $\mathbf{M}_{i,k}$ have a shape that depend on the element type and will be derived in Section 2.2.4 for the case of tetrahedral linear elements and in Section 2.2.5 for the case of tetrahedral quadratic elements. From Eq. 2.4 and the equations presented in Sections 2.2.3 and 2.2.3, one obtains:

$$\sum_{i \in \mathcal{P}_k} (\mathbf{K}_{i,k} + j\omega \mathbf{D}_{i,k} - \omega^2 \mathbf{M}_{i,k}) \cdot \mathbf{u}_i = \sum_{i \in \mathcal{P}_k} \mathbf{f}_{\mathbf{E}i,k}, \quad \forall k \in \mathcal{D} \tag{2.19}$$

The simultaneous observance of the equilibrium equations for every dual cell is supplied by the assembly process (Appendix B).

2.2.4 The Linear Tetrahedron

The dual complex is obtained through a baricentric division for both areas and volumes, as already done by Tonti [54] and other authors cited in the introduction of the present Chapter for different physical systems. The construction is shown in Fig. 2.3: the primal tetrahedron is divided into four parts. Now the focus is on the generic primal cell, indexed by i, and its generic node, indexed by the local index α. The local stiffness, damping and inertial forces are calculated on the space region $\hat{C}_{i,\alpha}$, that can be divided in two parts: $\hat{C}'_{i,\alpha}$ and $\hat{C}''_{i,\alpha}$.

The displacement field is supposed linear, therefore for each component p of the vector displacement $\mathbf{u} = \begin{bmatrix} u_x & u_y & u_z \end{bmatrix}^\mathsf{T}$ there exist four parameters a_p, b_p, c_p, d_p such

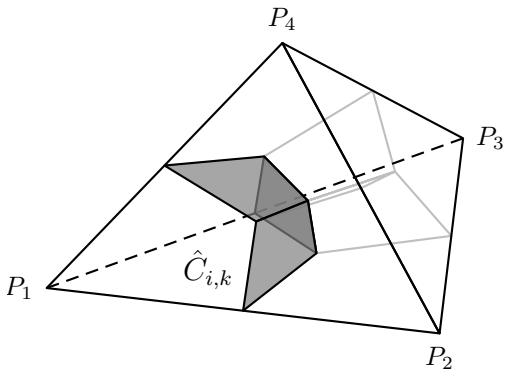

Figure 2.3: Linear tetrahedron and one of the tributary regions obtained through a baricentric subdivision

that:

$$u_p = a_p + b_p x + c_p y + d_p z = \begin{bmatrix} 1 & x & y & z \end{bmatrix} \begin{bmatrix} a_p \\ b_p \\ c_p \\ d_p \end{bmatrix}, \quad p = x, y, z \tag{2.20}$$

Eq. 2.20 is valid for both $\mathbf{u}^s$ and $\mathbf{u}^f$. Details about the well known shape functions are given in Appendix A.2. The following expression for the generic shape function holds:

$$N_q = \frac{1}{6V_C}(6v_q + 2A_{x,q}x + 2A_{y,q}y + 2A_{z,q}z), \quad q = 1, 2, 3, 4 \tag{2.21}$$

where V_C is the volume of the primal cell, v_q is the volume of the tetrahedron whose nodes are the origin O of the coordinate system and the three nodes of the q-th face of the primal cell; $\mathbf{A}_q$ is the vector area of the q-th face of the primal cell.

Stiffness matrix

The matrix $\Big[K\Big]_{i,\alpha}$ is calculated starting from Eq. 2.11. The areas involved in $[\mathbf{B_1}]_{l(\alpha)}$ are the 3 triangular areas of influence of $\hat{C}_{i,\alpha}$. The stress and strain tensors are constant in the linear tetrahedron because the displacement field is linear. Thus, $[\mathbf{B_2}\,(x, y, z)]_i$ is

constant and equal to:

$$\left[\mathbf{B_2}\right] = \frac{1}{3V_{C_i}} \begin{bmatrix} A_{x,1} & 0 & 0 & \cdots & A_{x,4} & 0 & 0 \\ 0 & A_{y,1} & 0 & \cdots & 0 & A_{y,4} & 0 \\ 0 & 0 & A_{z,1} & \cdots & 0 & 0 & A_{z,4} \\ A_{y,1} & A_{x,1} & 0 & \cdots & A_{y,4} & A_{x,4} & 0 \\ 0 & A_{z,1} & A_{y,1} & \cdots & 0 & A_{z,4} & A_{y,4} \\ A_{z,1} & 0 & A_{x,1} & \cdots & A_{z,4} & 0 & A_{x,4} \end{bmatrix}_i \tag{2.22}$$

where $\mathbf{A}_\alpha$ is the area vector of the tetrahedron face opposite to the node α. The integral in Eq. 2.11 is simplified and since the sum of the three areas of influence $l(\alpha)$ for $\hat{C}_{i,\alpha}$ is one third of the area $\mathbf{A}_\alpha$ (Fig. 2.3), the stiffness matrix for the tributary region associated to the node α is:

$$\left[K\right]_{i,\alpha} = \frac{1}{9V_{C_i}} \begin{bmatrix} \left[\mathbf{B_{lin}}_{i,\alpha}\right]^{\mathsf{T}} & \left[0\right] \\ \left[0\right] & \left[\mathbf{B_{lin}}_{i,\alpha}\right]^{\mathsf{T}} \end{bmatrix} \cdot \left[\mathbf{E}\right] \cdot \begin{bmatrix} \left[\mathbf{B_{lin}}\right] & \left[0\right] \\ \left[0\right] & \left[\mathbf{B_{lin}}\right] \end{bmatrix} \tag{2.23}$$

where

$$\left[\mathbf{B_{lin}}_{i,\alpha}\right]^{\mathsf{T}} = \begin{bmatrix} A_{x,\alpha} & 0 & 0 & A_{y,\alpha} & 0 & A_{z,\alpha} \\ 0 & A_{y,\alpha} & 0 & A_{x,\alpha} & A_{z,\alpha} & 0 \\ 0 & 0 & A_{z,\alpha} & 0 & A_{y,\alpha} & A_{x,\alpha} \end{bmatrix}_i \tag{2.24}$$

and $[\mathbf{B_{lin}}] = [[\mathbf{B_{lin}}_{i,1}] \cdots [\mathbf{B_{lin}}_{i,4}]]$. The stiffness matrix $[\mathbf{K}_i]$ for the Cell Method (obtained through a direct discretization of the equations on a finite domain) is identical to the stiffness matrix for Finite Elements. However, this observation applies only for the stiffness matrix and for linear elements. The differences between CM and FE will be shown in the construction of the damping and mass matrices and for higher order elements.

Damping and mass matrices

The integral of the shape functions on the domain $\hat{C}_{i,\alpha}$ can be obtained as the sum of the integral on the domains $\hat{C}'_{i,\alpha}$ and $\hat{C}''_{i,\alpha}$ (Fig. 2.3); $\hat{C}''_{i,\alpha}$ can be divided into 4 tetrahedral-shaped subdomains. With some coordinate transformations, and using repeatedly the

integrals on a single tetrahedron, the following expressions are obtained:

$$\bar{N}_q^{i,\alpha} = \frac{v_q}{24} + \frac{1}{1728}(A_{x,q}S_{x_\alpha} + A_{y,q}S_{y_\alpha} + A_{z,q}S_{z_\alpha}), \quad q = 1,2,3,4 \tag{2.25}$$

where v_q and $\mathbf{A}_q$ have the same meaning as in Appendix A.1 and

$$\begin{aligned} S_{x_\alpha} &= 23(x'_\alpha + x''_\alpha + x'''_\alpha) + 75x_\alpha \\ S_{y_\alpha} &= 23(y'_\alpha + y''_\alpha + y'''_\alpha) + 75y_\alpha \\ S_{z_\alpha} &= 23(z'_\alpha + z''_\alpha + z'''_\alpha) + 75z_\alpha \end{aligned}$$

In Eq. 2.26 x_α, y_α and z_α represent respectively the x, y and z coordinates of the node indexed by α; the symbols $'$, $''$ and $'''$ represent the other three nodes of the tetrahedron that are not the node indexed by α.

It is sufficient to insert Eq. 2.25 into Eq. 2.15 and 2.16 to get the elementary mass and damping matrices. It is clear that the damping and mass matrices for the Cell Method (obtained through a direct discretization of the equations on a finite domain) are not the same as the ones typical of Finite Elements.

2.2.5 The Quadratic Tetrahedron

To the author knowledge, this is the first derivation of a 3D quadratic element for the Cell Method. Quadratic elements have been used by Tonti [54] and Cosmi [16] for plane problems. Zovatto has used higher order elements in the case of the meshless approach [32]. It has been observed for structural elements that the convergence is faster when Gauss points are used for the subdivision of the geometrical domain. For this reason, the geometrical subdivision of the dual complex to fit a 10-nodes element (depicted in Fig. 2.4) has been obtained through a geometrical parameter g. In this study, $g = 0.2113$ represents the Gauss subdivision for the tetrahedron edges, however it can be modified, causing a modification of the dual complex too. Therefore this parameter provides an additional degree of freedom for the convergence of the Cell Method, that can be faster or slower depending also on the volumes involved for the calculation.

As shown in Fig. 2.4, each node is characterized by its tributary volume. The regions are created from the barycenters of the whole tetrahedron and of its faces. The parameter g defines the subdivision for each edge of the tetrahedron associated to the mid-nodes. In this case, the displacement field is supposed quadratic, therefore for each

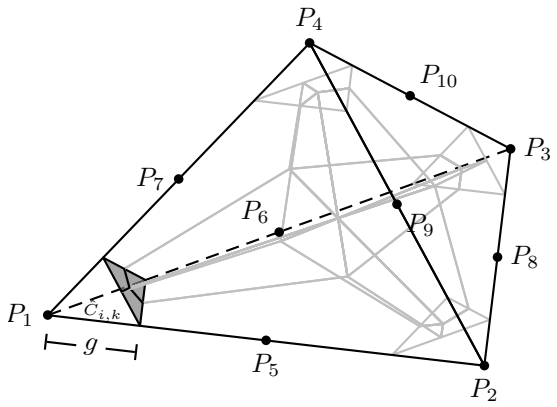

(a) First type of tributary region

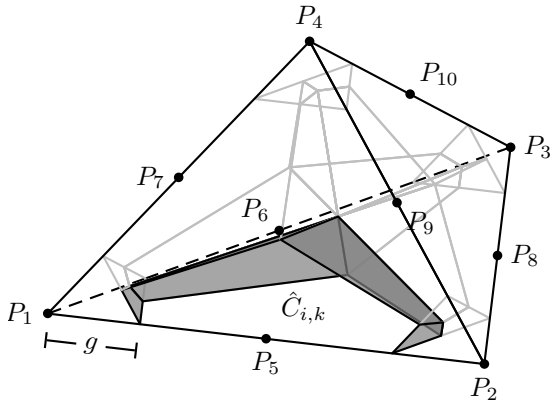

(b) Second type of tributary region

Figure 2.4: Quadratic tetrahedron

component p of the vector displacement $\mathbf{u} = \begin{bmatrix} u_x & u_y & u_z \end{bmatrix}^\mathsf{T}$ there exist ten parameters $a_p \dots d_p$ such that:

$$u_p = \begin{bmatrix} 1 & x & y & z & x^2 & y^2 & z^2 & xy & yz & zx \end{bmatrix} \cdot \begin{bmatrix} a_p & b_p & c_p & d_p & e_p & f_p & g_p & h_p & i_p & l_p \end{bmatrix}^\mathsf{T}, \quad p = x, y, z \tag{2.26}$$

Stiffness matrix

Again, the matrix $\begin{bmatrix} K \end{bmatrix}_{i,\alpha}$ is calculated starting from Eq. 2.11. The areas involved in $[\mathbf{B_1}]_{l(\alpha)}$ are the areas of influence of the triburaty region $\hat{C}_{i,\alpha}$ and are have different shapes if the node α is also a vertex of the tetrahedron or not.

In this case, the stress tensor is linear because the displacement field is quadratic. For $q = 1, \ldots, 10$, the expression of the shape functions derivatives is in the form:

$$\begin{aligned}
\frac{\partial N_q}{\partial x} &= \mathbf{N_{iT}}[q,2] + 2\mathbf{N_{iT}}[q,5]x + \mathbf{N_{iT}}[q,8]y + \mathbf{N_{iT}}[q,10]z \\
\frac{\partial N_q}{\partial y} &= \mathbf{N_{iT}}[q,3] + 2\mathbf{N_{iT}}[q,6]y + \mathbf{N_{iT}}[q,8]x + \mathbf{N_{iT}}[q,9]z \\
\frac{\partial N_q}{\partial z} &= \mathbf{N_{iT}}[q,4] + 2\mathbf{N_{iT}}[q,7]z + \mathbf{N_{iT}}[q,9]y + \mathbf{N_{iT}}[q,10]x
\end{aligned}$$

where

$$\mathbf{N_{iT}} = \left(\begin{bmatrix} 1 & \cdots & z_1 x_1 \\ \vdots & & \vdots \\ 1 & \cdots & z_{10} x_{10} \end{bmatrix}^{-1} \right)^{\mathsf{T}} \tag{2.27}$$

and the square brackets represent the position of the elements of $\mathbf{N_{iT}}$. It is easy to demonstrate that the integral term in Eq. 2.11 assumes the following meaning:

$$\frac{1}{\|\mathbf{A}_{l(\alpha)}\|} \int_{A_l(\alpha)} \Big[\mathbf{B_2}(x,y,z)\Big]_{i,l(\alpha)} \mathrm{d}A = \Big[\mathbf{B_2}(\mathbf{G}_{l(\alpha)})\Big]_{i,l(\alpha)} \tag{2.28}$$

where $\mathbf{G}_{l(\alpha)}$ is the baricenter of the area indexed by $l\,(\alpha)$. Details of all the geometrical elements involved (areas and baricenters) are not presented here for brevity. The calculation is finally completed by the sum among the involved areas of influence, as from Eq. 2.11.

Damping and mass matrix

The coefficients to be inserted into Eq. 2.5 can be written as

$$\bar{N}_q^{i,\alpha} = \Big[\mathbf{N_{iT}}[q,1] \cdots \mathbf{N_{iT}}[q,10]\Big] \cdot \Big[\bar{N}_{gc}^{i,\alpha}\Big], \quad q = 1,2,3,4 \tag{2.29}$$

where V_c represents the primal cell volume, $[\mathbf{N_{iT}}]$ is taken from Eq. 2.27 and $\bar{N}_{gc}^{i,\alpha}$ is a 10-row vector of geometrical coefficients depending on g and on the coordinates of the 10 nodes of the quadratic tetrahedron, as reported in Appendix A.3. With this notation, Eq. 2.15 and 2.16 are complete for this case.

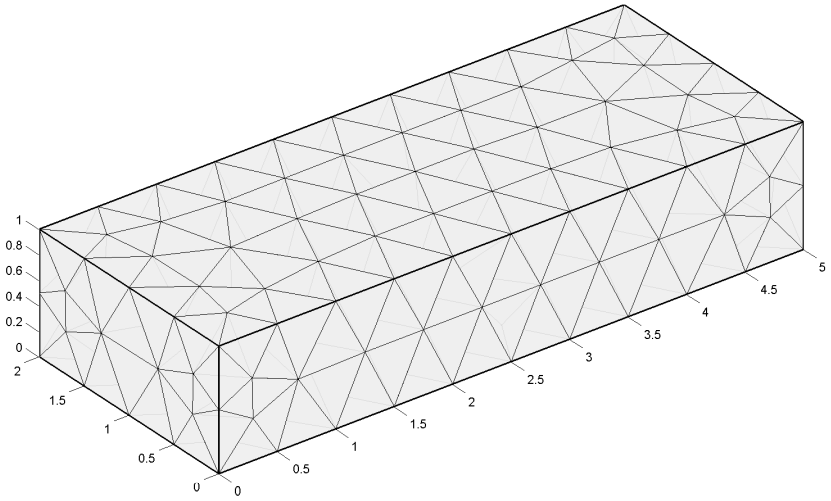

Figure 2.5: Tetrahedral mesh for the simple structural configuration

2.3 Validation of the Cell Method for the Biot theory

In this section, the presented method is validated through comparison with analytical and numerical results.

2.3.1 Dynamical structural case

In this case, only the structural part of the Biot's theory is taken into account, reducing the problem to a simple modal solution of a solid structure. The structure is depicted in Fig. 2.5: a $1 \times 2 \times 5 m^3$ block is meshed with 185 nodes and 532 elements. The material's properties are as in Table 2.1. The fluid displacements are set to zero. Free boundary conditions are applied. The comparison is between simulations carried out with CM and with FE, the last used as reference.

Material	$\rho\,(kg\,m^{-3})$	$E\,(Pa)$	ν	η_s
Solid	7850	200×10^9	0.3	0

Table 2.1: Materials properties for the structural configuration

Table. 2.2 compares the FE and CM calculation results, for linear tetrahedra. The

Nat. frequency n.	1	2	3	4	5	6	7	8	9	10
FE calculation (Hz)	217.6	302.7	310.6	502.0	505.2	593.2	599.9	865.6	896.0	902.7
CM calculation - linear tetrahedron (Hz)	214.9	296.2	308.0	494.1	501.3	584.8	585.6	840.3	874.3	882.7

Table 2.2: Natural frequencies for the structural case

FE calculation is referred to a converged solution obtained with a mesh of quadratic tetrahedra. The small differences can be explained by the following considerations:

- the formulation for the mass matrix is different in CM and FEM; the formulation for the stiffness matrix is equal only in case of linear elements;
- the formulation for the stiffness matrix in commercial FEM codes like the one used normally follows different rules of thumb for the definition of the matrix coefficients;
- the use of different kind of elements (linear tetrahedra not available in the commercial software).

The agreement is satisfactory considering the purposes of the test.

2.3.2 Surface impedance at normal incidence for poroelastic layers

In this case the complete poroelastic material is taken into account. The surface impedance at normal incidence is calculated from the results of the simulation. The poroelastic layer is plane, infinitely extended in the lateral directions and bonded to a rigid impervious wall (Fig. 2.6. The surface impedance calculated by the Cell Method is compared to the analytical solution by Allard [1], that is derived from the theoretical model and hence is used as reference. In order to represent the condition of infinite extent, the degrees of freedom (displacements) in the lateral directions are set to zero and only the axial displacements are taken into account.

A uniform unit acoustic pressure is applied to the external surface of the poroelastic material. The normal incidence surface impedance is calculated from the following Equation:

$$Z_n = \frac{1}{\mathrm{j}\omega \left[(1-\phi)\bar{u}_n^f + \phi \bar{u}_n^s \right]} \tag{2.30}$$

where ϕ is the porosity and $\bar{u}_n$ is the normal displacement on the surface invested by the acoustic pressure, resulting from an appropriate average. In fact, as shown in Fig. 2.7,

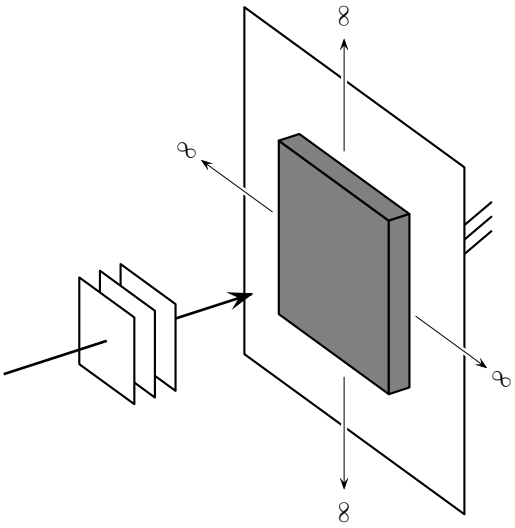

Figure 2.6: Surface impedance at normal incidence for a single poroelastic layer

the system is represented by a mesh composed of tetrahedral cells arranged in groups of three tetrahedra. In this way, a triangular prismatic configuration is obtained, easily refinable by changing the number of groups of three tetrahedra that are considered. On the other hand, with this simple configuration, the tetrahedra assume different shapes and the consequent out-of-direction effects (in terms of elastic, damping, inertial forces) can result in a difference between the nodal displacements of nodes belonging to the external surface invested by the acoustic pressure. For this reason, the average displacement on the surface is calculated, in function of the shape of the element (linear or quadratic), as described in Sections 2.2.4 and 2.2.5.

The load conditions are applied on the external surface of the system: a uniform pressure results in a force applied to the boundary areas of the tributary region $\hat{C}_{i,k}$. The solid and fluid components of the force are calculated as a product of the pressure by the area vector, splitting the result through porosity. In the equilibrium equations of the k-th dual cell, the force has to be summed up for all the boundary areas belonging to the i-th primal nodes associated to the k-th dual cell:

$$\mathbf{f}_{\mathbf{E},k} = \begin{bmatrix} \mathbf{f}_{\mathbf{K}}{}^{s} \\ \mathbf{f}_{\mathbf{K}}{}^{f} \end{bmatrix}_k = \begin{bmatrix} \sum_{i\in\mathcal{P}_k} -(1-\phi)P\mathbf{A}_{i,k} \\ \sum_{i\in\mathcal{P}_k} -\phi P\mathbf{A}_{i,k} \end{bmatrix}_k \tag{2.31}$$

where P is the pressure value, ϕ the porosity and $\mathbf{A}_{i,k}$ the outward normal area vector of the tributary region associated to the k-th dual cell and the i-th primal node. In this

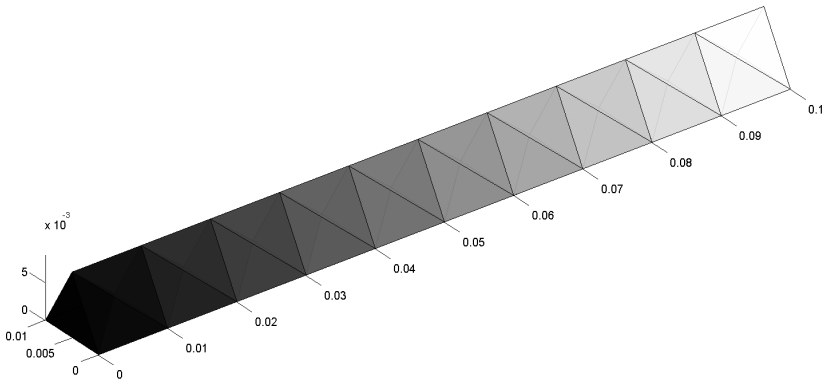

Figure 2.7: Tetrahedral mesh for a single layer configuration

way, the external force due to the acoustic pressure is directly inserted in the equilibrium equations and thus assembled.

The impervious rigid wall is simulated through a clamped boundary condition: the solid displacement is set to zero and the normal fluid displacement is set to zero. In this particular case, the axial solid and fluid displacements are set to zero on the nodes belonging to the rigid wall, because the lateral displacements are already set to zero by the infinite lateral extent boundary condition.

The considerations stated here regarding loading and boundary conditions and impedance calculation can be repeated for the case of a multilayer (Chapter 3).

Single poroelastic layer

The present test-case has already been analyzed for the case of Finite Elements by Panneton [44]. The material's properties are as in Table 2.3. The tetrahedral mesh is depicted in Fig. 2.7 for the case of linear tetrahedra; for the case of quadratic tetrahedra, intermediate nodes are added.

Material	ϕ	$\sigma(N\,s\,m^{-4})$	α_∞	$\Lambda\,(m)$	$\Lambda'\,(m)$	$\rho_1\,(kg\,m^{-3})$	$N\,(Pa)$	ν	η_s	$thickness(m)$
Glass wool	0.94	40000	1.06	56×10^{-6}	110×10^{-6}	130	2200000	0	0.1	0.1

Table 2.3: Materials properties for the single layer configuration

Fig. 2.8 shows the comparison between the analytical solution and the CM calculation, for linear tetrahedra. A good agreement is obtained with a mesh of 33 nodes and 30 elements. Fig. 2.9 shows the comparison between the analytical solution and the

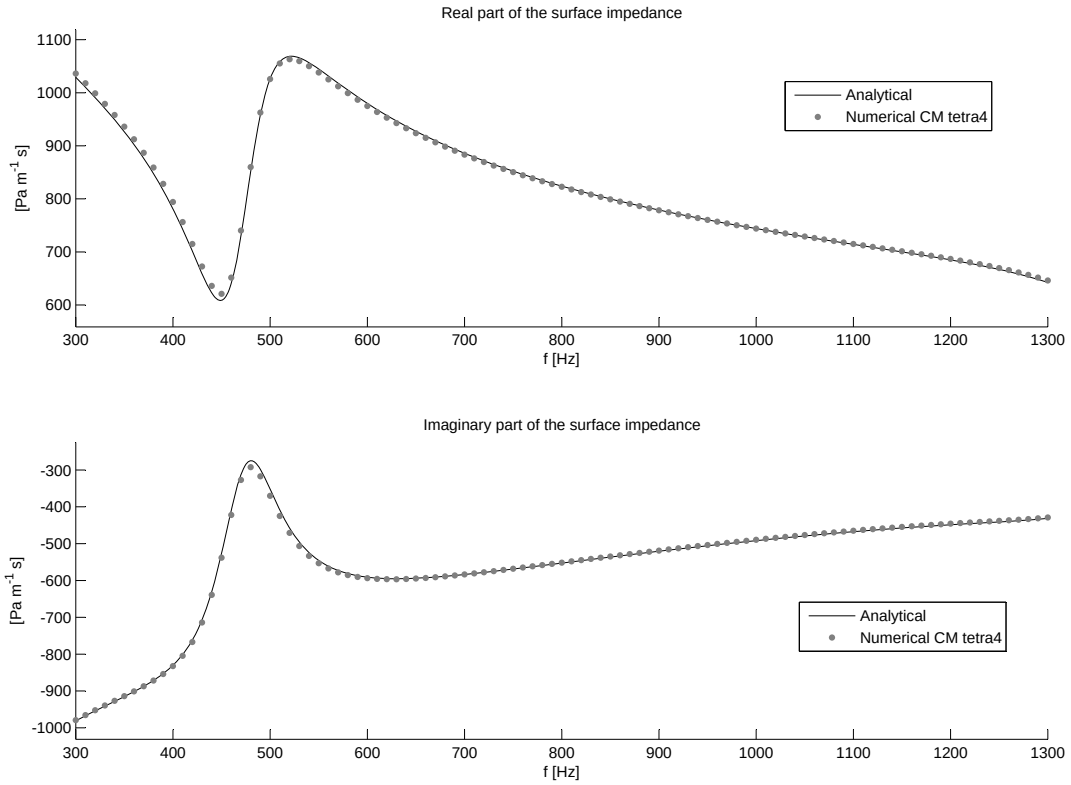

Figure 2.8: Real and imaginary part of the surface impedance at normal incidence, for a single layer configuration: comparison between analytical and numerical CM calculations with linear tetrahedral elements

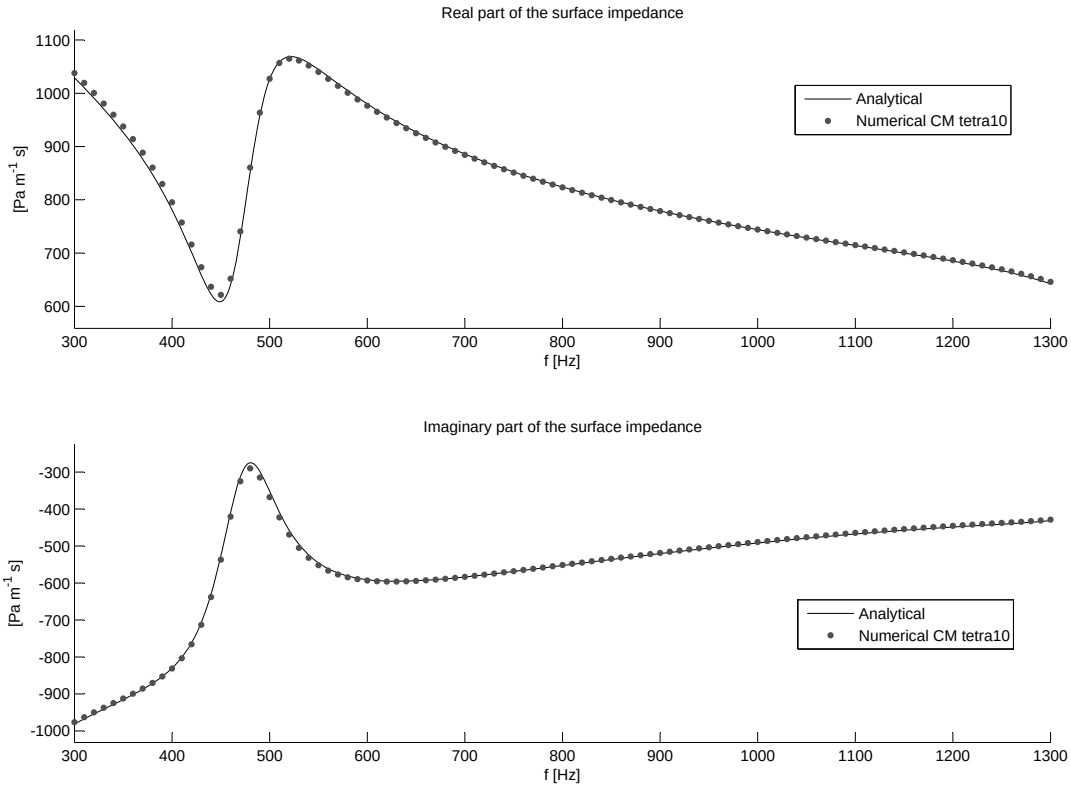

Figure 2.9: Real and imaginary part of the surface impedance at normal incidence, for a single layer configuration: comparison between analytical and numerical CM calculations with quadratic tetrahedral elements

CM calculation, for quadratic tetrahedra. A good agreement is obtained already with a mesh of 18 nodes and 15 elements. In conclusion, it is important to say that the use of tetrahedra is straightforward in the case of Cell Method. In fact, in algebraic topology the use of a simplex is natural because of duality relations between elements of the simplex, like a vertex and the opposite face. For this reason, tetrahedra have been used as cell elements, considering that the efficiency of the method is significative with this choice. In the common practice, the use of tetrahedra is necessary especially when geometries are complex and structures very thin, like in the case of automotive applications. When a FEM solver is adopted, the use of other elements (like hexahedra) would be in general preferred, in terms of efficiency and precision. However the use of tetrahedra, at least of quadratic order, is unavoidable for these complex geometries. As a result, mixed meshes are often adopted and a consistent quantity of man time is used for meshing. Since automatic meshing with tetrahedra is definitely less time consuming, the availability of a good solver for which the use of tetrahedra is natural, can be an asset in the common practice.

3 Application of the Cell Method to the case of interfaces

Compared to classical FE implementations of Biot's model, the Cell Method is much easier to implement and it allows a *natural* management of interface conditions between domains occupied by different materials, an issue that can be numerically problematic for the FE implementations of Biot's equations and that is basically related to the management of the surface boundary integrals generated by the reduction of the field equations to their weak-integral formulation (such reduction is simply not done in the Cell Method).

3.1 Interface conditions between poroelastic materials

Let us consider the interface between two different poroelastic materials A and B (Figure 3.1). Let 3 be the normal direction to the interface. $\boldsymbol{A}$ and $\boldsymbol{B}$ are two overlapping nodes of the interface (same coordinates), but $\boldsymbol{A}$ belongs to material A and $\boldsymbol{B}$ to material B. Let $\mathcal{D}_{\boldsymbol{A}}$ be the dual cell on the side of material A, $\mathcal{D}_{\boldsymbol{B}}$ the dual cell on the side of material B and $\mathcal{D}_{\boldsymbol{AB}} = \mathcal{D}_{\boldsymbol{A}} \cup \mathcal{D}_{\boldsymbol{B}}$. Four kinematic conditions (on displacements) must be respected [1]:

$$u_1^s(\boldsymbol{A}) = u_1^s(\boldsymbol{B}), \tag{3.1a}$$

$$u_2^s(\boldsymbol{A}) = u_2^s(\boldsymbol{B}), \tag{3.1b}$$

$$u_3^s(\boldsymbol{A}) = u_3^s(\boldsymbol{B}) \tag{3.1c}$$

and the fluid flux conservation:

$$\phi_A(u_3^f(\boldsymbol{A}) - u_3^s(\boldsymbol{A})) = \phi_B(u_3^f(\boldsymbol{B}) - u_3^s(\boldsymbol{B})). \tag{3.2}$$

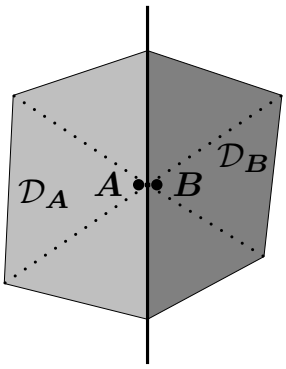

Figure 3.1: Scheme of the interface between two porous materials, denoted as A and B: nodes $\boldsymbol{A}$ and $\boldsymbol{B}$ are geometrically coincident. The dual cells are indicated in gray; the dotted lines show parts of the dual cells belonging to different primal cells.

Four stress conditions (on forces) must be respected:

$$\sigma^s_{13}(\boldsymbol{A}) = \sigma^s_{13}(\boldsymbol{B}), \tag{3.3a}$$

$$\sigma^s_{23}(\boldsymbol{A}) = \sigma^s_{23}(\boldsymbol{B}), \tag{3.3b}$$

the pressure conservation:

$$\frac{\sigma^f_{33}(\boldsymbol{A})}{\phi_A} = \frac{\sigma^f_{33}(\boldsymbol{B})}{\phi_B} \tag{3.4}$$

and the total stress conservation:

$$\sigma^s_{33}(\boldsymbol{A}) + \sigma^f_{33}(\boldsymbol{A}) = \sigma^s_{33}(\boldsymbol{B}) + \sigma^f_{33}(\boldsymbol{B}). \tag{3.5}$$

Conditions on primal variables cause modifications on the columns of the global assembled dynamic stiffness matrix (by rearranging relations between displacements, the unknowns), while conditions on dual variables cause modifications of the rows (by rearranging equilibrium equations).

3.1.1 Specific equilibrium equations

The equilibrium equations have to be respected for the dual cell $\mathcal{D}_{\boldsymbol{AB}}$; these equations are 6, corresponding to the 6 solid and fluid DOFs, while nodes $\boldsymbol{A}$ and $\boldsymbol{B}$ count in total 12 DOFs. The equilibrium equations have to be respected also for both nodes $\boldsymbol{A}$ and $\boldsymbol{B}$,

for the dual cells $\mathcal{D}_{\boldsymbol{A}}$ and $\mathcal{D}_{\boldsymbol{B}}$ (12 equations for 12 DOFs), when considering separately the contribution of forces to the two nodes.

The equilibrium equations are obtained by calculating the elementary matrices and by assembling the system, a process that in the case of the Cell Method implies a global force equilibrium. In the particular case of a poroelastic-poroelastic interface, nodes $\boldsymbol{A}$ and $\boldsymbol{B}$ are separated even if geometrically coincident, because discontinuities on some DOFs are present at the interface surface. For this reason, at the interface surface some stresses are present, representing actions between $\mathcal{D}_{\boldsymbol{A}}$ and $\mathcal{D}_{\boldsymbol{B}}$.

The equilibrium for $\mathcal{D}_{\boldsymbol{A}}$ and $\mathcal{D}_{\boldsymbol{B}}$ gives respectively:

$$F^p_{K,i}(\boldsymbol{A}) + F^p_{D,i}(\boldsymbol{A}) + F^p_{M,i}(\boldsymbol{A}) + R^p_i(\boldsymbol{A}) = F^p_{E,i}(\boldsymbol{A}), \quad i = 1,2,3; \quad p = s, f \tag{3.6a}$$

$$F^p_{K,i}(\boldsymbol{B}) + F^p_{D,i}(\boldsymbol{B}) + F^p_{M,i}(\boldsymbol{B}) + R^p_i(\boldsymbol{B}) = F^p_{E,i}(\boldsymbol{B}), \quad i = 1,2,3; \quad p = s, f \tag{3.6b}$$

where F_E is the total external force and F_K represents the stiffness force, F_D the damping force and F_M the inertial force, acting on the dual cell and calculated through the creation of elementary matrices. The stiffness force F_K does not take into account elastic forces acting at the interface when the elementary matrix is created. In fact, if we consider node $\boldsymbol{A}$, only the mutual actions between $\mathcal{D}_{\boldsymbol{A}}$ and dual cells belonging to the primal cells of which node $\boldsymbol{A}$ is a node, are taken into account. Analogous considerations apply reciprocally to node $\boldsymbol{B}$. For this reason, the stresses at the interface, that do not necessarily elide due to interface conditions, are represented by the terms called R.

To calculate $R^p_i(\boldsymbol{A})$ and $R^p_i(\boldsymbol{B})$, the interface area is considered. The stress acting on the dual cell $\mathcal{D}_{\boldsymbol{A}}$ in the direction normal to the interface are $\sigma^s_{13}(\boldsymbol{A})$, $\sigma^s_{23}(\boldsymbol{A})$ and $\sigma^s_{33}(\boldsymbol{A})$ for the solid phase and $\sigma^f_{33}(\boldsymbol{A})$ for the fluid phase. Similarly, $\sigma^s_{13}(\boldsymbol{B})$, $\sigma^s_{23}(\boldsymbol{B})$ and $\sigma^s_{33}(\boldsymbol{B})$ for the solid phase and $\sigma^f_{33}(\boldsymbol{B})$ for the fluid phase act on $\mathcal{D}_{\boldsymbol{B}}$.

Other stresses acting on the in-plane $(1,2)$ directions and producing mutual forces between $\mathcal{D}_{\boldsymbol{A}}$ and $\mathcal{D}_{\boldsymbol{B}}$ are $\sigma^s_{31}(\boldsymbol{A})$, $\sigma^s_{32}(\boldsymbol{A})$, $\sigma^s_{31}(\boldsymbol{B})$ and $\sigma^s_{32}(\boldsymbol{B})$. The remaining components of the stress tensor are either zero (the tangential stresses of the fluid phase) or act on in-plane surfaces, and hence do not produce interface forces.

For a linear tetrahedron, the stress tensor is constant, but in general can vary among the element volume. Moreover, several parts of the dual cells $\mathcal{D}_{\boldsymbol{A}}$ and $\mathcal{D}_{\boldsymbol{B}}$ can belong to different primal cells. The following relations apply to calculate the forces due to the

stresses on the interface surface:

$$R^p_{i,j}(\boldsymbol{A}) = \int_{S_I(\boldsymbol{A})} \sigma^p_{i,j}(\boldsymbol{A})\,\mathrm{d}S \tag{3.7a}$$

$$R^p_{i,j}(\boldsymbol{B}) = \int_{S_I(\boldsymbol{B})} \sigma^p_{i,j}(\boldsymbol{B})\,\mathrm{d}S \tag{3.7b}$$

where $S_I(\boldsymbol{A})$ and $S_I(\boldsymbol{B})$ are the interface areas, $\boldsymbol{A}$ stands for "relative to the dual cell $\mathcal{D}_{\boldsymbol{A}}$" and $\boldsymbol{B}$ stands for "relative to the dual cell $\mathcal{D}_{\boldsymbol{B}}$". In fact, the stresses $\sigma^p_{i,j}(\boldsymbol{A})$ are function of the points of $S_I(\boldsymbol{A})$ belonging to the dual cell $\mathcal{D}_{\boldsymbol{A}}$ and the stresses $\sigma^p_{i,j}(\boldsymbol{B})$ are function of the points of $S_I(\boldsymbol{B})$ belonging to the dual cell $\mathcal{D}_{\boldsymbol{B}}$. Considering areas with sign,

$$S_I(\boldsymbol{A}) = -S_I(\boldsymbol{B}) \tag{3.8}$$

and therefore, applying equations 3.3, 3.4 and 3.5:

$$R^s_{1,3}(\boldsymbol{A}) + R^s_{1,3}(\boldsymbol{B}) = 0 \tag{3.9a}$$

$$R^s_{2,3}(\boldsymbol{A}) + R^s_{2,3}(\boldsymbol{B}) = 0 \tag{3.9b}$$

and

$$\frac{R^f_{3,3}(\boldsymbol{A})}{\phi_A} + \frac{R^f_{3,3}(\boldsymbol{B})}{\phi_B} = 0 \tag{3.10}$$

$$R^s_{3,3}(\boldsymbol{A}) + R^f_{3,3}(\boldsymbol{A}) + R^s_{3,3}(\boldsymbol{B}) + R^f_{3,3}(\boldsymbol{B}) = 0. \tag{3.11}$$

Moreover, due to symmetry conditions, $\sigma^s_{31}(\boldsymbol{A}) = \sigma^s_{13}(\boldsymbol{A})$, $\sigma^s_{32}(\boldsymbol{A}) = \sigma^s_{23}(\boldsymbol{A})$, $\sigma^s_{31}(\boldsymbol{B}) = \sigma^s_{13}(\boldsymbol{B})$ and $\sigma^s_{32}(\boldsymbol{B}) = \sigma^s_{23}(\boldsymbol{B})$ and therefore

$$R^s_{3,1}(\boldsymbol{A}) + R^s_{3,1}(\boldsymbol{B}) = 0 \tag{3.12a}$$

$$R^s_{3,2}(\boldsymbol{A}) + R^s_{3,2}(\boldsymbol{B}) = 0. \tag{3.12b}$$

Summing up the forces due to stresses on the interface conditions, one obtains the terms to insert into equations 3.6a and 3.6b:

$$R_3^s(\boldsymbol{A}) = R_{1,3}^s(\boldsymbol{A}) + R_{2,3}^s(\boldsymbol{A}) + R_{3,3}^s(\boldsymbol{A}) \tag{3.13a}$$
$$R_3^s(\boldsymbol{B}) = R_{1,3}^s(\boldsymbol{B}) + R_{2,3}^s(\boldsymbol{B}) + R_{3,3}^s(\boldsymbol{B}) \tag{3.13b}$$
$$R_3^f(\boldsymbol{A}) = R_{3,3}^f(\boldsymbol{A}) \tag{3.13c}$$
$$R_3^f(\boldsymbol{B}) = R_{3,3}^f(\boldsymbol{B}) \tag{3.13d}$$

for direction 3; for directions 1 and 2, the non zero components are:

$$R_2^s(\boldsymbol{A}) = R_{3,2}^s(\boldsymbol{A}) \tag{3.14a}$$
$$R_2^s(\boldsymbol{B}) = R_{3,2}^s(\boldsymbol{B}) \tag{3.14b}$$
$$R_1^s(\boldsymbol{A}) = R_{3,1}^s(\boldsymbol{A}) \tag{3.14c}$$
$$R_1^s(\boldsymbol{B}) = R_{3,1}^s(\boldsymbol{B}). \tag{3.14d}$$

3.1.2 Direction normal to the interface

Let us consider now the equilibrium equations on $\mathcal{D}_{\boldsymbol{A}}$ and $\mathcal{D}_{\boldsymbol{B}}$ for direction 3, involving 4 DOFs (fluid and solid DOFs for nodes $\boldsymbol{A}$ and $\boldsymbol{B}$):

$$F_3^s(\boldsymbol{A}) + R_3^s(\boldsymbol{A}) = F_{E,3}^s(\boldsymbol{A}) \tag{3.15a}$$
$$F_3^s(\boldsymbol{B}) + R_3^s(\boldsymbol{B}) = F_{E,3}^s(\boldsymbol{B}) \tag{3.15b}$$
$$F_3^f(\boldsymbol{A}) + R_3^f(\boldsymbol{A}) = F_{E,3}^f(\boldsymbol{A}) \tag{3.15c}$$
$$F_3^f(\boldsymbol{B}) + R_3^f(\boldsymbol{B}) = F_{E,3}^f(\boldsymbol{B}) \tag{3.15d}$$

using the notation

$$F_i^p(\boldsymbol{A}) = F_{K,i}^p(\boldsymbol{A}) + F_{D,i}^p(\boldsymbol{A}) + F_{M,i}^p(\boldsymbol{A}), \quad i = 1,2,3; \quad p = s,f \tag{3.16a}$$
$$F_i^p(\boldsymbol{B}) = F_{K,i}^p(\boldsymbol{B}) + F_{D,i}^p(\boldsymbol{B}) + F_{M,i}^p(\boldsymbol{B}), \quad i = 1,2,3; \quad p = s,f. \tag{3.16b}$$

Summing up the four equations 3.15 and taking into account equations 3.13 and interface conditions 3.9 and 3.11, one obtains:

$$F_3^s(\boldsymbol{A}) + F_3^s(\boldsymbol{B}) + F_3^f(\boldsymbol{A}) + F_3^f(\boldsymbol{B}) = F_{E,3}^s(\boldsymbol{A}) + F_{E,3}^s(\boldsymbol{B}) + F_{E,3}^f(\boldsymbol{A}) + F_{E,3}^f(\boldsymbol{B}); \tag{3.17}$$

summing up the last equations 3.15c and 3.15d and taking into account equations 3.13 and interface condition 3.10, one obtains:

$$\frac{F_3^f(\boldsymbol{A})}{\phi_A} + \frac{F_3^f(\boldsymbol{B})}{\phi_B} = \frac{F_{E,3}^f(\boldsymbol{A})}{\phi_A} + \frac{F_{E,3}^f(\boldsymbol{B})}{\phi_B}. \tag{3.18}$$

In most of practical situations, external forces are not present at the interface and the second term of equations 3.17 and 3.18 is zero, anyway equations have been written here for the most general case. Equations 3.17 and 3.18 represent global equilibrium equations on $\mathcal{D}_{\boldsymbol{AB}}$; the partial equilibrium equations 3.15 on $\mathcal{D}_{\boldsymbol{A}}$ and $\mathcal{D}_{\boldsymbol{B}}$ have been in fact arranged to take into account the interface conditions on forces and considering that the two direct interface conditions on displacements (equations 3.1 and 3.2) must be fulfilled.

The numerical implementation of the interface conditions for direction 3 involves two steps:

- the arrangement of the rows (conditions on forces) of the global dynamic stiffness matrix relative to the 4 solid and fluid DOFs of nodes $\boldsymbol{A}$ and $\boldsymbol{B}$, according to equations 3.17 and 3.18;
- the arrangement of the columns (conditions of displacements) of the global dynamic stiffness matrix relative to the 4 solid and fluid DOFs of nodes $\boldsymbol{A}$ and $\boldsymbol{B}$, according to equations 3.1a and 3.2, the second one written as $u_3^f(\boldsymbol{B}) = u_3^s(\boldsymbol{A})(1-\phi_A/\phi_B) + u_3^f(\boldsymbol{A})\phi_A/\phi_B$.

To this hint, after the modification of the rows and columns involved, rows and columns relative to DOFs of node $\boldsymbol{B}$ are canceled, because both solid and fluid displacement components of node $\boldsymbol{B}$ are constrained.

3.1.3 In-plane directions with respect to the interface

Using the same notation and repeating the procedure of Section 3.1.2 and taking into account equations 3.14, four equilibrium equations can be written for direction 1 for

nodes $\boldsymbol{A}$ and $\boldsymbol{B}$:

$$F_1^s(\boldsymbol{A}) + R_{3,1}^s(\boldsymbol{A}) = F_{E,1}^s(\boldsymbol{A}) \tag{3.19a}$$
$$F_1^s(\boldsymbol{B}) + R_{3,1}^s(\boldsymbol{B}) = F_{E,1}^s(\boldsymbol{B}) \tag{3.19b}$$
$$F_1^f(\boldsymbol{A}) = F_{E,1}^f(\boldsymbol{A}) \tag{3.19c}$$
$$F_1^f(\boldsymbol{B}) = F_{E,1}^f(\boldsymbol{B}) \tag{3.19d}$$

Summing the first two equations and using equation 3.9, one obtains:

$$F_1^s(\boldsymbol{A}) + F_1^s(\boldsymbol{B}) = F_{E,1}^s(\boldsymbol{A}) + F_{E,1}^s(\boldsymbol{B}). \tag{3.20}$$

Equations 3.20 and 3.19c, 3.19d represent global equilibrium equations on $\mathcal{D}_{\boldsymbol{AB}}$; the partial equilibrium equations 3.19 on $\mathcal{D}_{\boldsymbol{A}}$ and $\mathcal{D}_{\boldsymbol{B}}$ for the solid phase have been in fact arranged to take into account the interface conditions on forces and considering that the direct interface conditions on displacements (equation 3.1) must be fulfilled.

As in the case of direction 3, the numerical implementation requires the arrangement of rows and columns of the global dynamic stiffness matrix relative to the solid DOFs of nodes $\boldsymbol{A}$ and $\boldsymbol{B}$ according to equations 3.20 and 3.1, while the equilibrium equations (rows) relative to fluid DOFs of nodes $\boldsymbol{A}$ and $\boldsymbol{B}$ are not modified, according to equations 3.19c and 3.19d. At the end, the row and column relative to the solid DOF of node $\boldsymbol{B}$ are canceled, because the solid displacement components of node $\boldsymbol{B}$ is constrained. Analogous considerations are valid for direction 2.

3.2 Verification of the method

The verification of the method is presented here directly in the case of a multilayer configuration (Figure 3.2). A multilayer composed of 4 poroelastic materials (Table 3.1)

Material	ϕ	$\sigma(N\,s\,m^{-4})$	α_∞	$\Lambda\,(m)$	$\Lambda'\,(m)$	$\rho_1\,(kg\,m^{-3})$	$N\,(Pa)$	ν	η_s	$thickness(m)$
Blanket	0.98	34000	1.18	60×10^{-6}	87×10^{-6}	41	110000	0.3	0.015	4×10^{-3}
Screen	0.80	32000	2.56	6×10^{-6}	24×10^{-6}	125	1000000	0.3	0.1	0.8×10^{-3}
Foam A	0.97	87000	2.52	37×10^{-6}	119×10^{-6}	31	55000	0.3	0.055	5×10^{-3}
Foam B	0.99	65000	1.98	37×10^{-6}	121×10^{-6}	16	18000	0.3	0.1	16×10^{-3}

Table 3.1: Materials properties for the multilayer configuration.

is excited by an acoustic pressure. The poroelastic layers are plane, infinitely extended

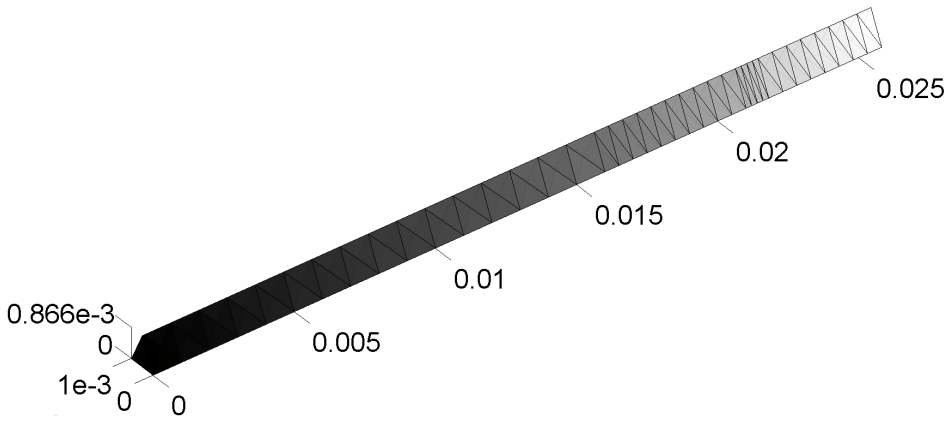

Figure 3.2: The mesh used for the verification of the method.

in the lateral directions and the last layer is bonded to a rigid impervious wall. The surface impedance calculated with the Cell Method is compared to the analytical solution obtained with the transfer matrix method (TMM) [1], that is derived from theoretical considerations and hence is used as a reference. In order to represent the condition of infinite extent, the degrees of freedom (displacements) in the lateral directions are set to zero and only the axial displacements are taken into account. Linear tetrahedral elements are used. The results are presented in Figure 3.3, showing good agreement between numerical calculation and theory.

The surface impedance is obtained by integration of the nodal displacements of the three nodes of the face excited by the acoustic pressure. Some small differences between the numerical and theoretical curves are explained considering the geometry of the system.

Even if the implementation of the interface conditions requires some theoretical and algebraic considerations, simple results come out in terms of forces and conditions on displacements. The implementation of these results is straightforward, requiring some "natural" adaptations of the equilibrium equations to take into account the interface conditions as constraints on primal (displacements) or dual variables (forces). In this way, the idea behind the Cell Method, i.e. the direct discrete application of physical laws, is maintained. The most important aspect is that all the modifications are directly referred to physical quantities defined on finite geometrical domains. Compared to Finite Elements, the implementation of interface conditions is easier and comes out naturally also in the case of a *(u-U)* formulation.

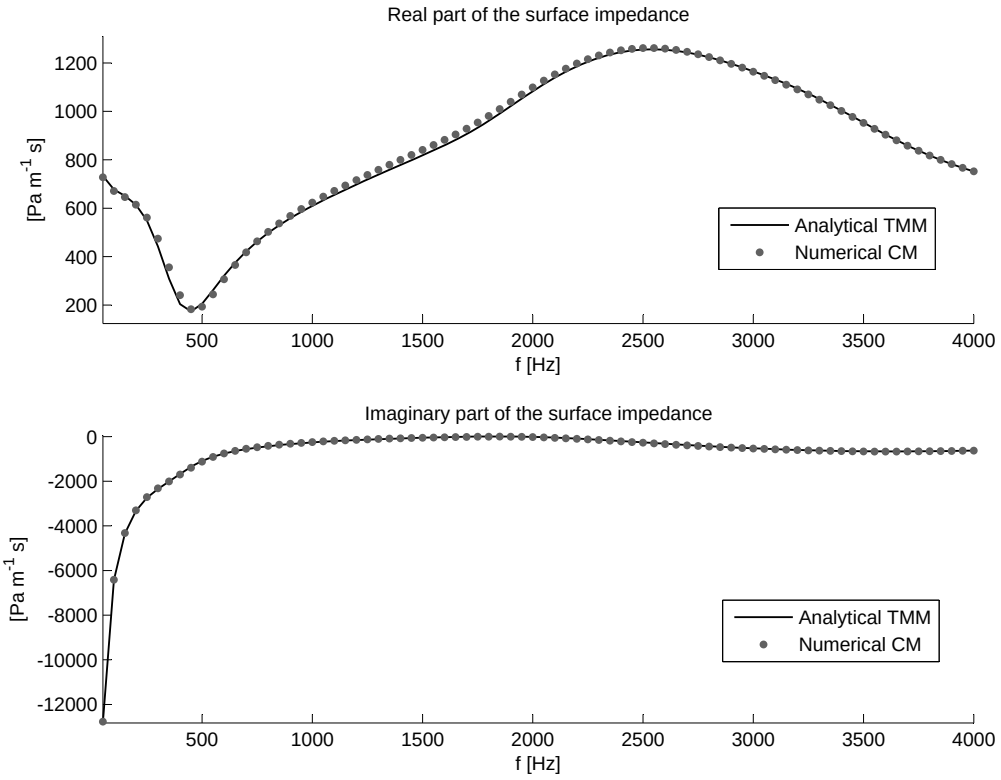

Figure 3.3: Comparison between numerical calculation and theory.

4 Sound absorption of porous materials with inclusions

Acoustical heterogeneous materials obtained through a set of porous inclusions are studied. A theoretical model based on the homogenization hypotheses introduced by Boutin [11] is presented; the inclusions are supposed periodic and the frame rigid. The idea behind the inclusion of a second acoustical porous material into the original single porosity material, is to obtain the pressure diffusion effect already observed in the double porosity case. At the same time, the main disadvantages of double porosity are faced, especially the absorption behavior at very low frequency and the lose of performances in transmission. Experimental data are obtained in Kundt Tubes of different dimensions in terms of absorption curves and compared to analytical results for representative configurations, thus validating the theoretical model.

4.1 Motivation

In order to enhance the absorption properties of these materials, several studies have investigated the case of double porosity [4, 11, 39, 40, 49]. The double porosity configuration consists in a set of periodical perforations, in the thickness direction. Under certain conditions, that are explained in Section 4.2, the perforated material can be considered as an equivalent homogeneous porous material. At first the theoretical aspects have been addressed [11, 39, 40]; lately, numerical aspects and practical applications have been studied [4, 49]. Double porosity materials have proven to be very effective for the enhancement of the absorption coefficient. However, several problems arise in practice:

- when compared to the single porosity material, the double porosity material provides an increase of the absorption coefficient at low frequency, but in general the gain is obtained above a certain frequency value. Therefore, the absorption proper-

ties are worsened at very low frequency, a range where in general the performances of single porosity materials are already not satisfactory;

- in general, the absorption curve for double porosity presents a series of ripples. The peak at lower frequency is a positive characteristic, however at higher frequency the curve shape can be quite irregular and far from a constant pattern;
- due to the perforations, for problems in which the acoustic transmission is involved, the performance of the double porosity material is worse than the single porosity one. In any case, when a general problem is addressed (e.g. a complex field like in [3] or the case of adjacent cavities) the problem can be significant.

In the case of double porosity, under certain hypotheses [40], a situation of low or high permeability contrast can be considered, depending on the microporous and mesoporous geometrical parameters (Section 4.2). When the permeability contrast is high, a pressure diffusion effect can be observed. In this case, the absorption coefficient is increased significantly in a range around a theoretical frequency, called the diffusion frequency.

As described by Horoshenkov in [28], there is growing interest in innovative solutions concerning materials for acoustical applications. Moreover, inhomogeneous materials have been considered in [17, 46]. In particular, a study about porous heterogeneous acoustic materials made up of inclusions in the thickness direction, has been addressed by Groby et al., concerning the case of inclusions in a periodical slab. In [24], a theoretical model for the pressure field equations based on the Green's functions is described and is followed by experimental verifications. The explored frequency range is very wide and comprehensive of the typical ultrasound frequencies. In our case, the range of interest is tuned for the common acoustical applications in the building or automotive fields ($50 - 4000$Hz, or narrowed to $50 - 500$Hz for some applications); moreover, the theoretical model is based on the homogenization hypotheses introduced by Boutin [11].

The idea behind the inclusion of a second poroelastic material into the original single porosity material, is to obtain the pressure diffusion effect already observed in the double porosity case, without losing performances in transmission. This goal can be obtained with heterogeneous materials, made up of periodical inclusions: experimental, analytical and numerical results for the case of absorption are shown in the present Chapter. The topic of sound transmission is addressed in Chapter 6, where positive effects of heterogeneous materials are shown in comparison to double porosity. In addition to these effects, the absorption curve, in general, shows also a more regular pattern at

higher frequencies. In this way, the three problems described above for double porosity are faced up by heterogeneous materials.

In the case of double porosity, the pressure diffusion effect is obtained through a highly resistive microporous material (together with all the problems involved in this case [39]). In fact, such a characteristic provides a large difference between the resistivity of the microporous material and the resistivity of the air in the pores, that can be approximated to zero. The same effect can be reproduced in the case of heterogeneous materials, through a high difference in the air flow resistivity between the two involved microporous materials.

4.2 Analytical model

Let us consider an heterogeneous medium composed of two poroelastic materials. Three scales are needed to describe the structure (Figure 4.1).

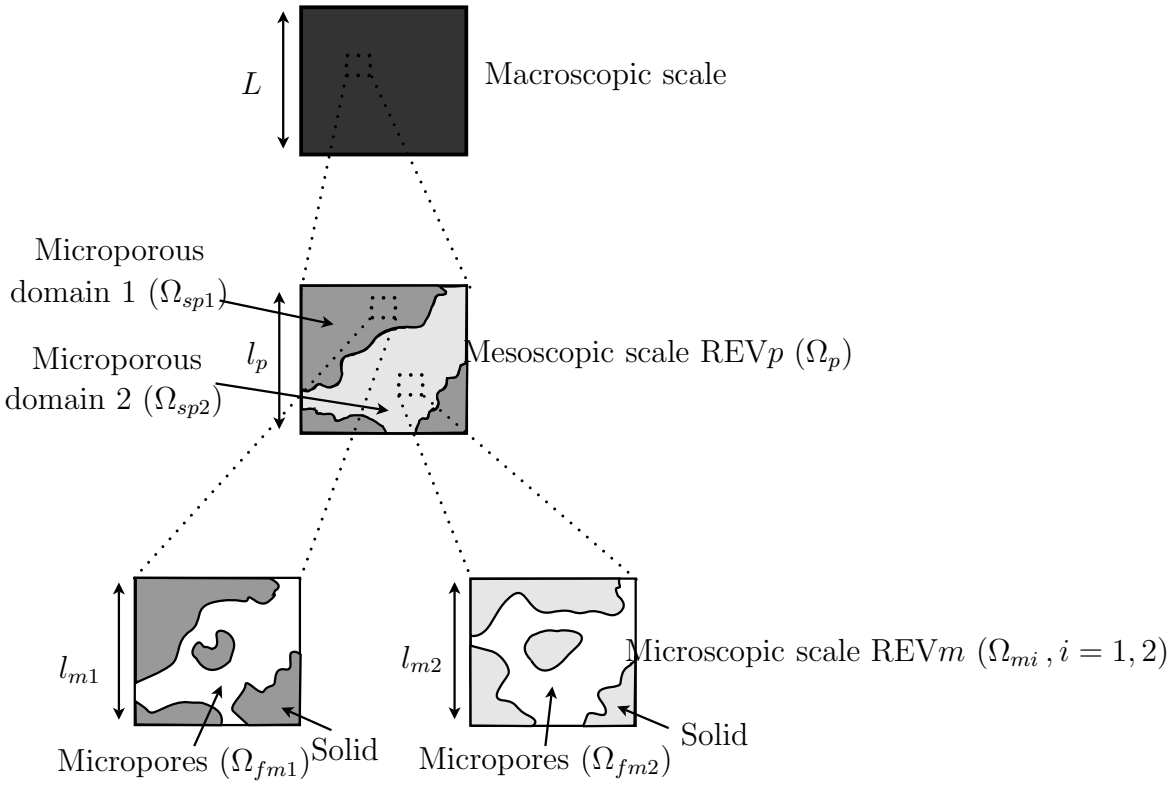

Figure 4.1: The three scales of the considered heterogeneous medium.

In what follows, it is assumed that there is a high permeability contrast between the two microporous domain 1 and 2. That is why, in all this study, the microporous domain 1 has a higher resistivity than the poroelastic inclusion (microporous domain 2).

Let L, l_p, l_{mi}, $i = 1, 2$, be, respectively, the three characteristic sizes for each level of representation: macroscopic, mesoscopic, and microscopic. In concrete terms, l_m and l_p are respectively given by the order of magnitude of the micro- and mesoheterogeneities, where as the wavelength in the material can be used to evaluate L. In what follows, the subscripts p, m, h are used to distinguish variables, respectively, related to poroelastic inclusions, micopores, and to the heterogeneous medium. In this system, one assumes the existence of two representative elementary volumes REVm and REVp defined, respectively, from the micropores and poroelastic inclusions structures. Poroelastic inclusions and micropores are supposed to be air-filled, and interconnected. The porosity of the heterogeneous medium can be written in function of porosities related to poroelastic inclusions ans micropores:

$$\phi_h = \frac{\Omega_{fm1}}{\Omega_{m1}}\frac{\Omega_{sp1}}{\Omega_p} + \frac{\Omega_{fm2}}{\Omega_{m2}}\frac{\Omega_{sp2}}{\Omega_p} = (1-\phi_p)\phi_{m1} + \phi_p\phi_{m2}, \tag{4.1}$$

where ϕ_p denotes the porosity to the fictive medium consisting of the microporous domain 1 mesoperforated with air where the microporous domain 2 (poroelastic inclusion) has been replaced by air. In order to represent the multiscale heterogeneous mediem as a homogeneous equivalent one, the first assumption that has to be made is that the characteristic size of the phenomenon is large compared to the "largest" heterogeneities. So a first separation of scales (macro/meso) must exist:

$$\frac{l_p}{L} \ll 1. \tag{4.2}$$

Moreover, a separation of scales between micro- and mesoscales must also exist:

$$\frac{l_{m1}}{l_p} \ll 1, \quad \frac{l_{m2}}{l_p} \ll 1. \tag{4.3}$$

An analytical model of the wave propagation at audible frequencies is presented in the case where (i) the medium is periodic, (ii) there is a double separation of scales between micro and meso size on the one hand and between meso and macro size on the other hand, (iii) the motion of the skeleton can be neglected. In what follows, a temporal dependency $e^{j\omega t}$ is assumed.

The considered periodic cells are represented in Figure 4.2. They consist in a heterogeneous material. Indeed, a poroelastic inclusion is considered. In the case in which the poroelastic inclusion is air Olny [39, 40] established a generalized Darcy's law similar to single porosity media involving a dynamic permeability Π_{dp} and a bulk modulus K_{dp} depending on the mesogeometry.

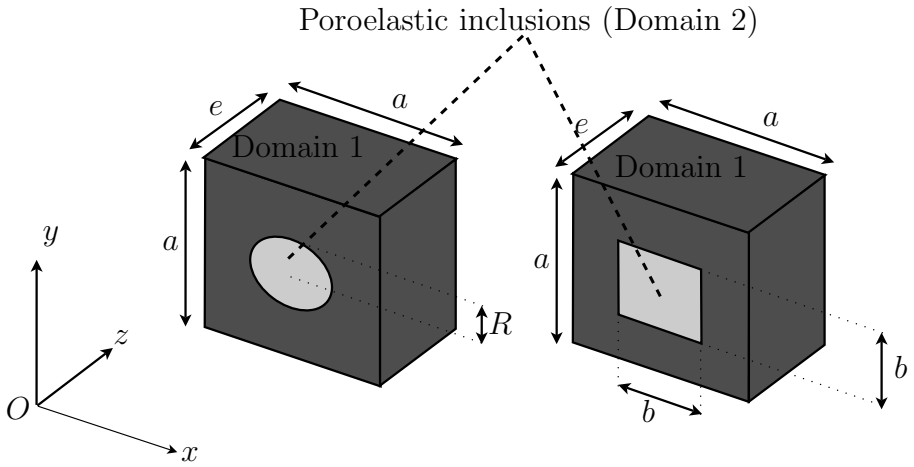

Figure 4.2: Considered periodic cells: circular or square cross-section for the poroelastic inclusion.

If one is interested in the propagation in the direction parallel to the axis z, similarly to what has been done in [39, 40], the characteristic impedance Z_c and the propagation constant k in the heterogeneous medium can be determined with homogeneization by:

$$Z_c = \sqrt{\rho_h K_h} \quad \text{and} \quad k = \omega\sqrt{\frac{\rho_h}{K_h}} \tag{4.4}$$

where the effective density ρ_h is related to the dynamic permeability Π_h by

$$\rho_h = \frac{\eta}{j\omega\Pi_h} \tag{4.5}$$

where η denotes the dynamic viscosity of the interstitial fluid. The surface impedance Z_h of a material of thickness e and backed by a material of surface impedance Z_S can then be easily calculated by

$$Z_h = Z_C \frac{Z_C - jZ_S \cot ke}{Z_S - jZ_C \cot ke} \tag{4.6}$$

where e is the thickness of the heterogeneous material. The normal incidence sound absorption coefficient is then given by

$$\alpha = \frac{4R[z_h]}{(R[z_h]+1)^2 + I[z_h]^2} \tag{4.7}$$

with $z_h = Z_h/(\rho_a c_a)$, where ρ_a and c_a are the density and sound speed in the medium in which the incident wave propagates.

4.2.1 Visco-inertial effects

Similarly to [39, 40], in the case of circular cylindrical inclusions of poroelastic inclusions, the dynamic permeability Π_h of the whole heterogeneous material in the direction normal to the material is given by:

$$\Pi_h = (1-\phi_p)\Pi_{m1} + \phi_p \Pi_{m2} \tag{4.8}$$

where $\Pi_{mi}\,, i = 1, 2$, denotes the dynamic permeability of the single porosity microporous medium i.

An approach based on a semiphenomenological model is chosen for the calculation of each $\Pi_{mi}\,, i = 1, 2$. Two approaches are possible. The first one consists in using the acoustical parameters of the Johnson et al.'s semiphenomenological model [29] (ϕ_{mi}, σ_{mi}, $\alpha_{\infty mi}$ and $\Lambda_{mi}\,, i = 1, 2$). Thus, the dynamical density of each microporous domain is [29]:

$$\Pi_{mi}(\omega) = \frac{\eta}{j\omega}\left\{\frac{\alpha_{\infty mi}\rho_0}{\phi_{mi}}\left[1 - j\frac{\sigma_{mi}\phi_{mi}}{\omega\rho_0\alpha_{\infty mi}}\sqrt{1 + j\frac{4\alpha_{\infty mi}^2\eta\rho_0\omega}{\sigma_{mi}^2\Lambda_{mi}^2\phi_{mi}^2}}\,\right]\right\}^{-1}, \quad i = 1, 2 \tag{4.9}$$

where ρ_0 is the static air density.

The second one consists in using the acoustical parameters of the Johnson-Lafarge semiphenomenological model [34] (ϕ_{mi}, σ_{mi}, $\alpha_{\infty mi}$ and $\Lambda_{mi}\,, i = 1, 2$). In this case, the dynamical density of each microporous domain is [34]:

$$\Pi_{mi}(\omega) = \frac{\Pi_{mi}(0)}{j\frac{\omega}{\omega_{\nu mi}} + \sqrt{1 + j\frac{M_{mi}}{2}\frac{\omega}{\omega_{\nu mi}}}}, \quad i = 1, 2 \tag{4.10}$$

where $\Pi_{mi}(0)$ is the static permeability of the i-th single porosity medium, given by $\Pi_{mi}(0) = \eta/\sigma_{mi}$,

$$\omega_{\nu mi} = \sigma_{mi}\phi_{mi}/(\rho_0\alpha_{\infty mi}) \tag{4.11}$$

denotes the viscous characteristic frequency of the i-th microporous medium and $M_{mi} = 8\alpha_{\infty mi}\eta/\ (\phi_{mi}\sigma_{mi}\Lambda_{mi}^2)$.

4.2.2 Thermal effects

Similarly to [39, 40], in the case of circular cylindrical inclusions of poroelastic inclusions and for high permeability contrast between the two microporous domain 1 and 2, the macroscopic dynamical bulk modulus K_h can be given by:

$$K_h = \left[\frac{\phi_p}{K_{m2}(\omega)} + (1-\phi_p)\frac{F_d\,(\omega)}{K_{m1}(\omega)}\right]^{-1} \tag{4.12}$$

K_{m1} and K_{m2} are respectively the dynamical bulk moduli of the single porosity domain 1 and the single porosity domain 2.

F_d is the ratio of the average pressure in the micropores to the pressure in the poroelastic inclusion. This function describes the pressure diffusion effects occurring when the wavelength in the porous domain becomes of the same order of magnitude that the meso-heterogeneities. This function is associated with a characteristic frequency:

$$\omega_d = \frac{(1-\phi_p)P_0}{\phi_{m1}\sigma_{m1}D(0)} \tag{4.13}$$

where $D(0)$ can be estimated by:

$$D(0) \simeq (1-\phi_p)l_p^2 \tag{4.14}$$

with l_p the size of the meso-heterogeneities ($l_p = 2R$ for circular cross-section or $l_p = b$ for square cross section).

- For frequencies such that $\omega \ll \omega_d$, F_d tends to 1 as ω decreases, the pressure is uniform in the whole material.
- For frequencies such that $\omega \gg \omega_d$, F_d tends to 0 as ω increases: the micro-pores do not participate in the macroscopic response of the material.

- For frequencies around ω_d, F_d is complex and describes dissipation effects specific to multi-scales porous materials: the pressure diffusion effects [11, 40].

An approach based on a semiphenomenological model is chosen for the calculation of K_{mi}, $i = 1, 2$. Two approaches are possible. The first one consists in using the acoustical parameters of the Champoux-Allard's semiphenomenological model [14] (ϕ_{mi} and Λ'_{mi}). Thus, the dynamical bulk modulus of the microporous domains are [14]:

$$K_{mi}(\omega) = \frac{\gamma P_0/\phi_{mi}}{\gamma - (\gamma-1)\left[1 - j\frac{8\kappa}{\Lambda'^2_{mi} C_p \rho_0 \omega}\sqrt{1 + j\frac{\Lambda'^2_{mi} C_p \rho_0 \omega}{16\kappa}}\right]^{-1}} \tag{4.15}$$

C_p denotes the specific heat at constant pressure, γ the ratio of the specific heats and κ the conductivity of the air.

The second one consists in using the acoustical parameters of the Johnson-Lafarge semiphenomenological model [34] (ϕ_{mi}, Λ'_{mi} and $\Theta_{mi}(0)$). In this case, the dynamical bulk modulus of the microporous domains are [34]:

$$K_{mi}(\omega) = \frac{\gamma P_0/\phi_{mi}}{\gamma - j(\gamma-1)\frac{\Theta_{mi}}{\delta_t^2 \phi_{mi}}} \tag{4.16}$$

where P_0 is the static ambient pressure, $\delta_t = \sqrt{\kappa/(\rho_0 C_p \omega)}$ is the thermal boundary layer thickness and Θ_{mi} denotes the dynamic thermal permeability of the i-th microporous domain, that can be computed as:

$$\Theta_{mi}(\omega) = \frac{\Theta_{mi}(0)}{j\frac{\omega}{\omega_{tmi}} + \sqrt{1 + j\frac{M'_{mi}}{2}\frac{\omega}{\omega_{tmi}}}}, \quad i = 1, 2 \tag{4.17}$$

where

$$\omega_{tmi} = \kappa\phi_{mi}/(\rho_0 C_p \Theta_{mi}(0)) \tag{4.18}$$

denotes the thermal characteristic frequency of the i-th microporous domain and $M'_{mi} = 8\Theta_{mi}(0)/\ (\phi_{mi}\Lambda'^2_{mi})$.

Case of no pressure diffusion effects

For frequencies much lower than ω_d, the scales coupling function F_d is close to 1: the pressure is uniform in the whole material, no pressure diffusion effect occurs and it is sufficient to replacing F_d by 1 in Equation (4.12).

Case of pressure diffusion effects

For frequencies such that $\omega \sim \omega_d$, the pressure in the micro and mesoscopic domains are of the same order of magnitude but differ. The dissipative effects of pressure diffusion occur, F_d takes the form [40]:

$$F_d(\omega) = 1 - j\frac{\omega}{\omega_d}\frac{D(\omega)}{D(0)} \tag{4.19}$$

where $D(\omega)$ is a function whose properties can be compared to the ones of the thermal permeability introduced by Lafarge et al [34]. It is associated with the pressure diffusion effects [39, 40] which can occur in the heterogeneous material depending on its physical properties (high permeability contrast necessary) and frequency. Those effects arise through a variation of the pressure in the micropores at the mesoscopic scale and an increase of the imaginary part of the macroscopic bulk modulus of the material thereby inducing a dramatic increase of the sound absorption. A semi-phenomenological expression of $D(\omega)$ is [40] given by:

$$D(\omega) = \frac{D(0)}{j\frac{\omega}{\omega_d} + \sqrt{1 + j\frac{M_d}{2}\frac{\omega}{\omega_d}}} \tag{4.20}$$

and the static value of D, $D(0)$, is a geometric parameter. For a circular cross-section, $D(0)$ can be evaluated analytically [49, 52]:

$$D(0) = \frac{a^2}{4\pi}\left(\ln\left(\frac{1}{\phi_p}\right) - \frac{3}{2} + 2\phi_p - \frac{\phi_p^2}{2}\right) \tag{4.21}$$

whith $\phi_p = \pi R^2/a^2$ where a is the size of the cell (Fig. 4.2). Further considerations about the parameter $D(0)$ will be given in section 4.5. The form parameter M_d introduced in

Equation (4.20) is:

$$M_d = \frac{8D(0)}{\Lambda_d^2(1-\phi_p)} \tag{4.22}$$

where

$$\Lambda_d = 2\frac{\Omega_{sp1}}{\partial\Omega_{sp1}} \tag{4.23}$$

Ω_{sp1} refers to the part of the mesoscopic representative elementary volume occupied by the microporous domain 1 and $\partial\Omega_{sp1}$ is the area of the interface between the microporous domain 1 and the microporous domain 2 in the mesoscopic representative elementary volume. So for straight circular cross-section:

$$\Lambda_d = \frac{a^2 - \pi R^2}{\pi R} \tag{4.24}$$

As discussed in [39], for finite thickness materials, the theoretical model must be corrected so that the surface $\partial\Omega_{sp1}$ should also include the surface of the microporous domain in contact with the exterior air when the heterogeneous material is backed by a rigid wall. With this thickness correction, for rigid wall termination:

$$\Lambda_d = \frac{2e(a^2 - \pi R^2)}{2e\pi R + (a^2 - \pi R)} \tag{4.25}$$

4.2.3 Example of analytical prediction

Fig. 4.3 presents an example of use of the analytical model, to predict the absorption of a layer of heterogeneous material, when compared to single and double porosity. The materials described in Section 4.3.1 are used; the thickness is 80mm and the mesoporosity is 0.31 for both double porosity and heterogeneous material. The advantages of using inclusions are shown, especially at very low frequency. Further details will be given in the following Sections, where experimental results will be presented and compared to analytical predictions.

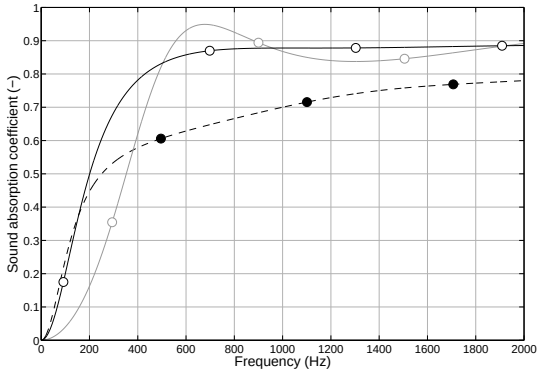

Figure 4.3: 80mm thick layer: theoretical comparison between single porosity (--●--), double porosity (—○—) and heterogeneous material with inclusions (—○—)

4.3 Materials and testing

A consistent number of experimental data and analytical calculations will be presented in Section 4.4 and compared in Section 4.5. The comparison with numerical predictions is presented in Chapter 5.

4.3.1 Materials choice

The materials initially used are named ***u*160** and ***melamine***. The first one is a foam composed of recycled materials, the second one is a well-known white melamine (Fig. 4.4). Their properties have been experimentally characterized in the ENTPE Labs and

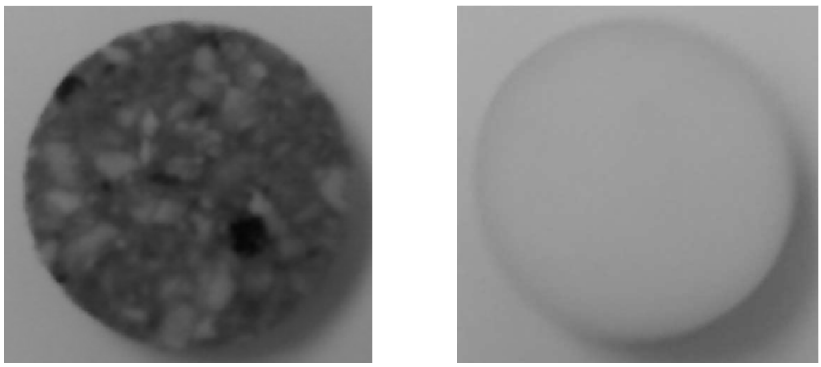

(a) *u*160 (b) *melamine*

Figure 4.4: The microporous materials

are presented in Table 4.1. The two materials have been chosen for the following reasons:

- the gap between the two materials in terms of flow resistivity, that is indicated by the analytical models as the crucial parameter for a good improvement of the sound absorption;
- the fact that *u*160 is already a quite good material in absorption: therefore the aim is to enhance its performance, especially at low frequency, where poroelastic materials are often unsatisfactory;
- the fact that the difference in flow resistivity is significant but not the biggest possible: therefore the aim is to show that a pressure diffusion effect can be obtained also in *normal* conditions and with common materials and not only in *optimal* conditions. Moreover, it must be pointed out that materials characterized by very high flow resistivity offer in theory very good absorption, but in practice are not very robust, because a small gap of air can deteriorate a lot the theoretical behavior. For those reasons, it was preferred to use materials with *ordinary* characteristics.

In addition, the microporous *u*160 is a good candidate, that respects the condition of flow viscosity [49] in the measured frequency domain (approximatively under 4500Hz). In fact, from Eq. 4.11, $\omega_{vm} = 27733\text{rad/s}$, therefore in the range $\omega < \omega_{vm}$ and the flow can be considered viscous. From a theoretical point of view, the possibility to obtain an absorption gain due to pressure diffusion mechanisms is effective.

Moreover, a second microporous material acting as a frame in the heterogeneous configuration, has been used for verification. It is a common rockwool and is here referred just as ***rockwool***. It is depicted in Fig. 4.5 and it has been used for measurements in the Big Kundt Tube (see 4.3.2). For this reason, the parameters presented in Table 4.1 are referred to the low frequency range and have been used for the analytical calculations. Details about the characterization of *rockwool* can be found in 4.3.3.

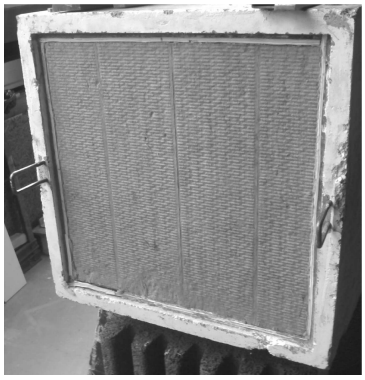

Figure 4.5: *rockwool* - measurement in the Big Kundt Tube

Material	ϕ	$\sigma(N\,s\,m^{-4})$	α_∞	$\Lambda\,(m)$	$\Lambda'\,(m)$	$\Theta(0)\,(m^2)$	$\rho_1\,(kg\,m^{-3})$	$E\,(kPa)$	ν	η_s
u160	0.90	47700	1.29	24×10^{-6}	200×10^{-6}	2.9×10^{-9}	159.8	500	0.4	0.180
melamine	0.99	10000	1.00	100×10^{-6}	200×10^{-6}	3.3×10^{-9}	8.5	235	0.3	0.066
rockwool	0.97	50000	1.07	175×10^{-6}	175×10^{-6}	3.3×10^{-9}	130	4400	0	0.1

Table 4.1: Materials properties

4.3.2 Testing instruments

The testing instruments used for the measurements of sound absorption consisted of:

- an home made standing wave tube (here named *Small Kundt Tube*, SKT - Fig. 4.6), having a circular cross-section of a 46mm diameter, on which two microphone positions are available on the top of the tube and one on the back. In this way, both absorption and dynamic density / bulk modulus measurements are possible, in a range approximately between 150 and 4300Hz;

- a B&K type 4106 standing wave tube (here named *Medium Kundt Tube*, MKT - Fig. 4.7), having a circular cross-section of a 100mm diameter, on which four microphone positions are available on the top of the tube. In this way, both absorption and transmission measurements are possible. For absorption, the available frequency range falls approximately between 150 and 2000Hz; topics about transmission will be discussed in a further report;

- an home made 5.5m long standing wave tube (here named *Big Kundt Tube*, BKT - Fig. 4.8), having a square cross-section of 600×600mm. Two peculiarities of the BKT are important for the present study: the measurable frequency range, that comprehends low frequencies (approximately between 50 and 500Hz), and the dimension of the cross-section, that permits an investigation of samples characterized by series of periodical cells. More details about the ENTPE big standing wave tube can be found in [36], p. $77 - 80$ and in [39].

Description	Cross-section shape	Cross-section dimension	Frequency range
Small Kundt Tube - SKT	circular	*diameter* = 46mm	$150 - 4300$Hz
Medium Kundt Tube - MKT	circular	*diameter* = 100mm	$150 - 2000$Hz
Big Kundt Tube - BKT	square	*edge* = 600mm	$50 - 500$Hz

Table 4.2: Different impedance tubes characteristics for the experimental measurements

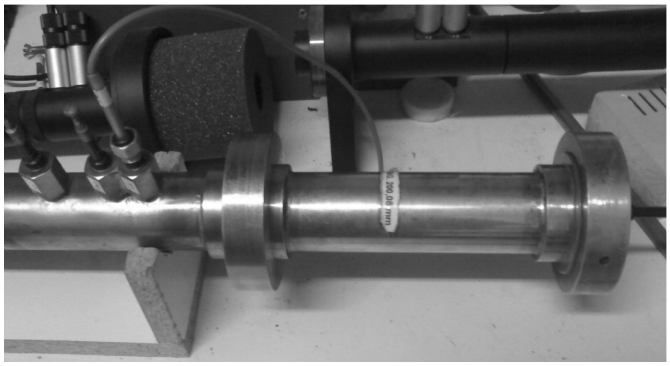

(a) Front view

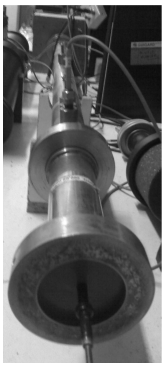

(b) Top view

Figure 4.6: Small Kundt Tube

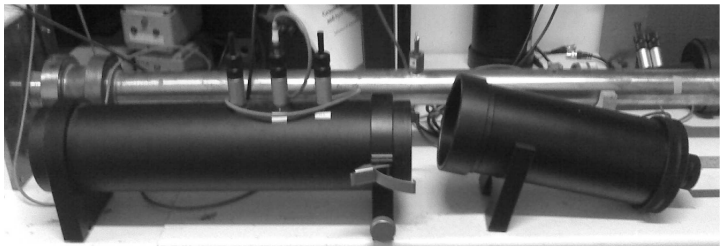

Figure 4.7: Medium Kundt Tube

Porosity and flow resistivity have been measured directly in the ENTPE Labs, as well as the mechanical parameters.

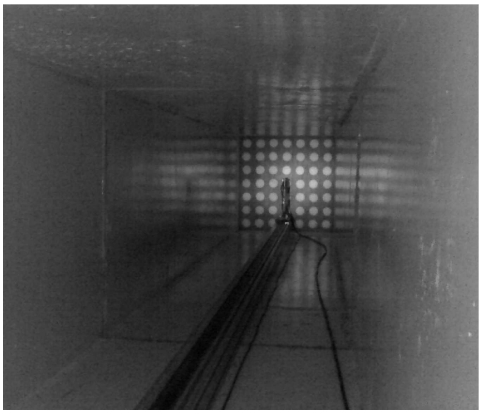

(a) Rail and microphone in the interior

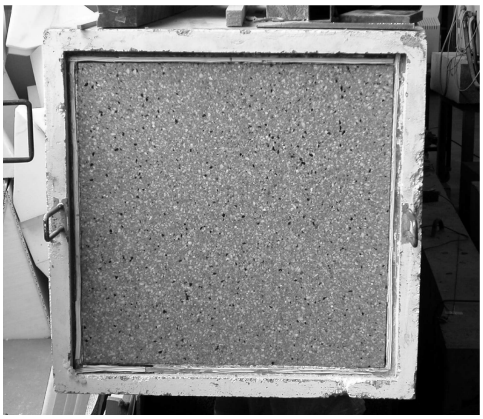

(b) Preparation of a sample of $u160$

Figure 4.8: Big Kundt Tube

4.3.3 Characterization

In this section, details about the characterization of *u*160 and *rockwool* are given. The characterization of *melamine* has not deserved any particularity.

u160

A 4.5cm thick *u*160 sample has been characterized in the Small Kundt Tube: the acoustical parameters have been obtained by inversion [41]. The double porosity model introduced by Olny and Boutin [40] uses the Johnson-Lafarge model and expresses the dynamical thermal permeability of the microporous domain directly from the static thermal permeability. Having at our disposal the instrumentation for a complete inverse characterization, a 6-parameter Johnson-Lafarge model has been used.

As well known (for example as described in [35]), the boundary conditions are very important when the sound absorption coefficient is to be determined. In this case, the size of the sample is crucial. In fact, two main problems can arise:

- a smaller sized sample causes the presence of gaps of air that lead to an overestimation of the sound absorption coefficient;
- a larger sized sample causes the compression of the material and/or a change of the nominal sliding boundary conditions.

Those effects can be observed in Fig. 4.10, where the Biot resonance frequencies are impossible to predict and where the repeatability of the curve shape is not excellent, probably due to small gaps of air or compression in the different samples. Those problems must be taken into account also when double porosity or heterogeneous materials are considered. Even if in this case the elastic behavior is not crucial for the determination of the sound absorption coefficient, the presence of gaps of air or compressed material can determine an increase of the sound absorption coefficient at some frequencies, or a shift of the theoretical resonant frequency.

When double porosity or heterogeneous materials are concerned, the layers are not any more homogeneous. Therefore, the Biot elastic properties of the single material(s) usually do not play an important role in the determination of the sound absorption coefficient. However, this behavior must be verified experimentally and when possible through FEM calculation (see next Reports).

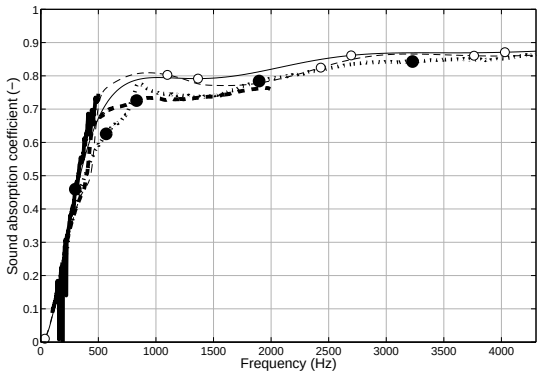

(a) 45mm thick layer: comparison between experimental data in the small (⋯●⋯), medium (–●–) and big (—●—) Kundt tube and analytical Johnson-Lafarge (—○—) and Biot (–○–) models

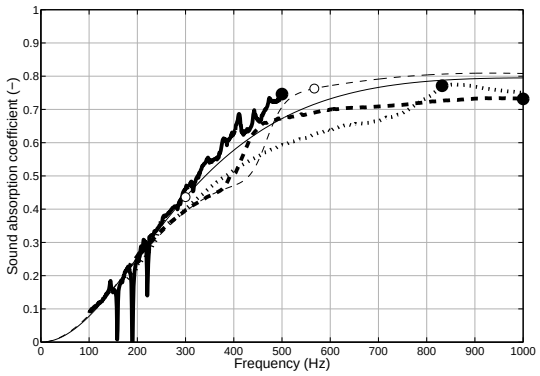

(b) 45mm thick layer - zoom of Fig. 4.9(a) at low frequency

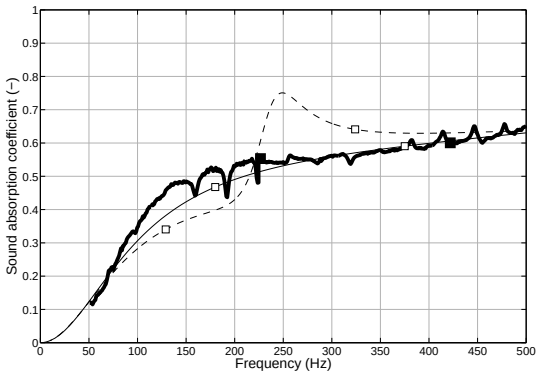

(c) 90mm thick layer: comparison between experimental data in the big (—■—) Kundt tube and analytical Johnson-Lafarge (—□—) and Biot (–□–) models

Figure 4.9: *u*160 characterization: comparison between experimental data and analytical models

rockwool

The inversion of the parameters from data obtained in the Small Kundt Tube is rather accurate: the results are presented in Fig. 4.11 for a 30mm and a 90mm thick samples. The 90mm sample is composed of three 30mm samples placed side by side. The characterization is valid in the range $10-4000$Hz and the parameters are the ones presented in Table 4.1, except from the flow resistivity σ, that assumes a value of $88000\,\mathrm{N\,s\,m^{-4}}$. The acoustical parameters are well characterized. Also the mechanical parameters show good agreement (even if a measurement in the Small Kundt Tube is not completely reliable from this point of view, as pointed out in 4.3.3) in the case of the 30mm thick sample.

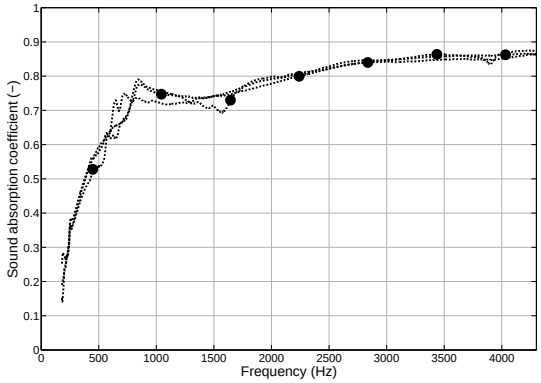

Figure 4.10: *u*160 - repeatability of the measurements in the Small Kundt Tube, for three 45mm thick samples

The disagreement in the case of the 90mm thick sample can be explained because the 90mm sample is composed of three 30mm samples placed side by side and this configuration modifies the mechanical properties.
However, when the Big Kundt Tube is concerned, the observed absorption coefficient is different in the range $0 - 500$Hz. This behavior can be explained by the following reasons:

- *rockwool* layers in the Big Kundt Tube are more rigid than *u*160 layers and, as a difference from the case of the more pliable *u*160 that fills better the tube section, small gaps of air are present on the sides of the samples;
- this effect can be taken into account by using the sound absorption measurements in the Big Kundt Tube for the characterization;
- in this context, the same base layers are used for measurements of single porosity, double porosity and heterogeneous configurations: thus, it can be stated that parameters valid for the characterization of *rockwool* in the Big Kundt Tube are reliable also for the configurations of interest for the present study.

Similar plate resonances are observed as in the case of *u*160 (Fig. 4.11(c)). The first Biot resonance is not observed in the measured frequency range. It has been assumed that the effect of the gaps of air is to modify only the resistivity of the material. This assumption is in order to simplify the problem, because a direct inversion cannot be obtained from the BKT absorption data (no third microphone is available on the back side). As a result, the parameters presented in Table 4.1 have been used for the present study.

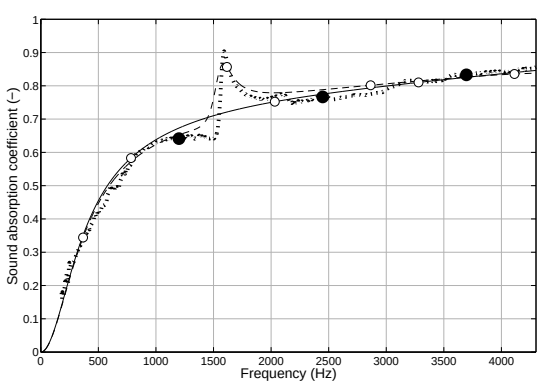

(a) 30mm thick layer: comparison between experimental data in the Small Kundt Tube (-●-) and analytical Johnson-Lafarge (—○—) and Biot (--○--) models ($\sigma = 88000 N\,s\,m^{-4}$)

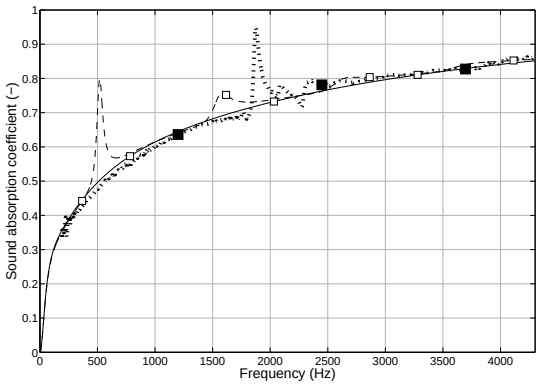

(b) 90mm thick layer: comparison between experimental data in the Small Kundt Tube (-■-) and analytical Johnson-Lafarge (—□—) and Biot (--□--) models ($\sigma = 88000 N\,s\,m^{-4}$)

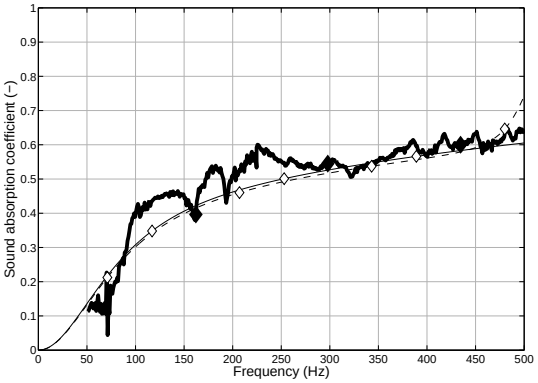

(c) 90mm thick layer: comparison between experimental data in the Big Kundt Tube (—◆—) and analytical Johnson-Lafarge (—◇—) and Biot (--◇--) models ($\sigma = 50000 N\,s\,m^{-4}$)

Figure 4.11: *rockwool* characterization: comparison between experimental data and analytical models

Moreover, as will be clear later, the behavior of *rockwool* is not very different from the one of *u*160 because the supposed difference in gap of resistivity between the couples *u*160 - *melamine* and *rockwool* - *melamine* is not as expected (the resistivities of *u*160 and *rockwool* in the BKT are very similar). However, the measurements with *rockwool* are useful to verify experimentally and confirm the results obtained with *u*160 through another material, that are presented in the following chapters.

In summary, the acoustical parameters for *u*160 and *melamine* are approximately valid at low frequency and up to 4000Hz, the characterization being made in the Small Kundt Tube and verified in the Big Kundt Tube. The acoustical parameters for *rockwool*

(more rigid and less pliable than $u160$) are characterized directly in the Big Kundt Tube and are valid only for measurements in the Big Kundt Tube, due to the difficulties of arranging the material in the big square cross-section.

The Johnson-Lafarge model has been used for the characterization and will be used also for the validation of the analytical model (Section 4.5), as in Eq. 4.10 and 4.16.

4.4 Experimental results

In this section, the results of the experimental measurements are presented. Two configurations have been tested:

- double porosity, with $u160$ as microporous material
- heterogeneous, with $u160$ as main microporous material filled up by *melamine* as inclusion

The heterogeneous case is the main issue of the present study. The case of double porosity is used as a reference. In fact, the performance of the heterogeneous material is here compared to the performance of the double porosity configuration. Moreover, in the next Sections 4.4.1, 4.4.2 and 4.4.3, the analytical model is first verified through comparison with the experimental results in the case of double porosity. As a second step, the analytical model and the comparison are extended to the heterogeneous case. The first experimental tests are performed in the Small and Medium Kundt Tubes. In those cases the external cross section of the sample is circular and only one periodic cell can be considered (Fig. 4.12), due to the small dimensions and geometry of the sample. Therefore, the hypotheses of the homogenization theory are not completely satisfied, however this simple configuration is a good approximation of a larger layer. The effect of different sized cross sections, i.e. the mesoporosity variation, can be tested. The information obtained is useful also to prepare the tests in the Big Kundt Tube, that require much more time for the preparation of the sample and for the measurement.

4.4.1 Small Kundt tube

Four different shaped samples (Tab. 4.3) have been tested.

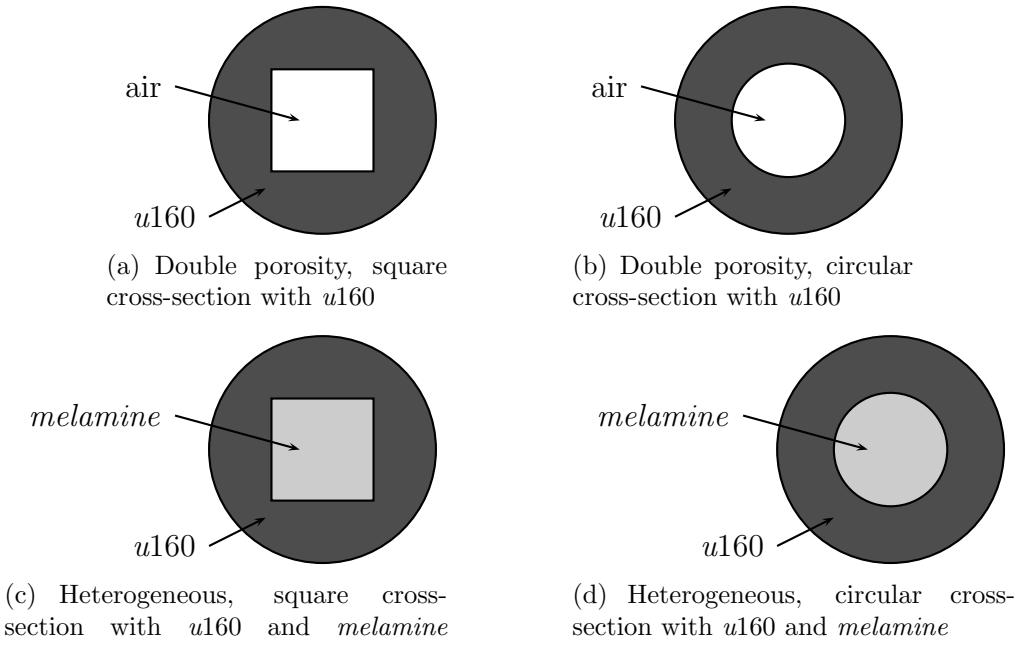

(a) Double porosity, square cross-section with *u*160

(b) Double porosity, circular cross-section with *u*160

(c) Heterogeneous, square cross-section with *u*160 and *melamine*

(d) Heterogeneous, circular cross-section with *u*160 and *melamine*

Figure 4.12: Sketch of cross-section geometries for a sample in the SKT or in the MKT, representing a single cell

Figure 4.13: Example of an heterogeneous sample (*u*160 - *melamine*) in the Medium Kundt Tube

Configuration	**External cross section**		**Internal cross section**		**Mesoporosity**	**Thickness**
	Shape	Dimension (mm)	Shape	Dimension (mm)	(-)	(mm)
A	circular	$r = 23$	square	$l = 10$	0.060	45
B	circular	$r = 23$	square	$l = 14$	0.118	45
C	circular	$r = 23$	square	$l = 25$	0.376	45
D	circular	$r = 23$	circular	$r = 14.5$	0.397	45

Table 4.3: Small Kundt Tube geometries

Effect of mesoporosity

The effect of a mesoporosity variation is represented in Fig. 4.14 and in Fig. 4.15.

It has been verified that asymmetry of the samples has little influence on the results. In the case of double porosity, increasing the size of the perforation from a 10mm edge

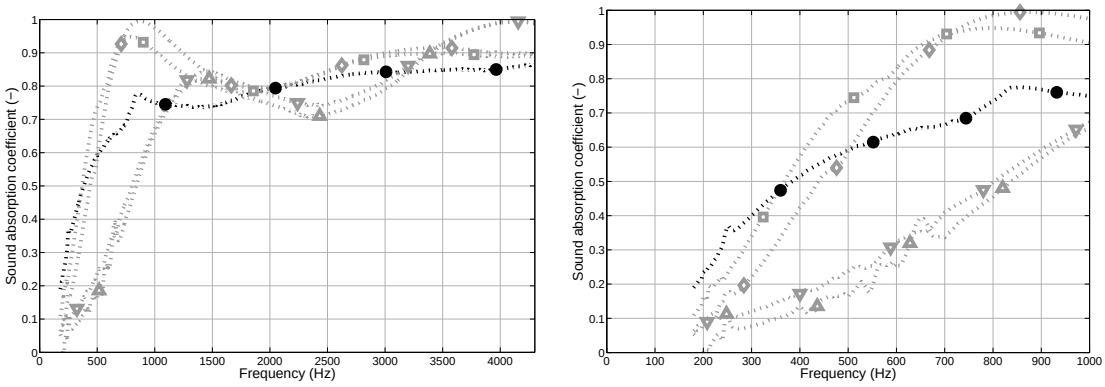

(a) Entire measured frequency range

(b) Zoom at low frequency

Figure 4.14: Small Kundt Tube, 45mm thick layer, double porosity - influence of the mesoporosity: configurations A (□), B (◇), C (△) and D (▽), compared to the homogeneous $u160$ (●)

(config. A) to a 14mm edge (config. B) provides better performances in absorption above 700Hz. However, when the perforation becomes too large (25mm edge, config. C), the absorption coefficient is decreased for a much larger frequency range and a better absorption can be obtained only above 3500Hz. Comparing configuration C and D, it can be observed that the absorption curves are very close when the mesoporosity is similar. The effect of Biot resonances is very smooth and can be observed around 500Hz for the configurations A and B. In the case of heterogeneous material, as well as for double porosity, increasing the size of the inclusion has a positive effect for higher frequencies. The sound absorption coefficient is increased above 700Hz when moving from configuration A to configuration B and above 800Hz when moving from configuration B to configuration C. Again, the size of the inclusion does not have a big effect when the mesoporosity is similar (configurations C and D). Also in this case, the effect of Biot resonances is very smooth and can be observed around 500Hz as for the configurations A and B.

The measurement for configuration D shows a well pronounced peak for frequencies around 2000Hz. This behavior could be explained as a Biot resonance, but the dimension of the peak is quite large and mostly, for configuration C the peak is less pronounced.

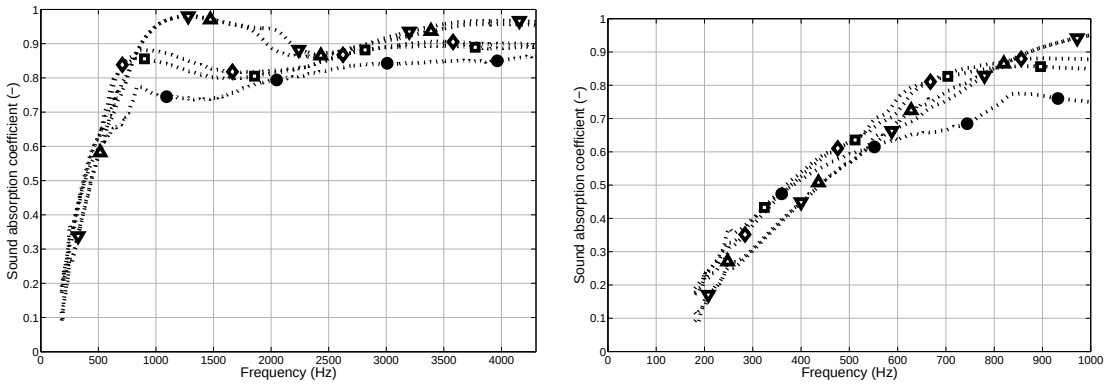

(a) Entire measured frequency range (b) Low frequency

Figure 4.15: Small Kundt Tube, 45mm thick layer, inclusion of melamine - influence of the mesoporosity: configurations A (▫), B (◇), C (△) and D (▽), compared to the homogeneous $u160$ (●)

Thus the most reliable explanation is a small gap of air that changes the curve shape. This idea will be confirmed by numerical simulations.

In both cases (double porosity and heterogeneous material) and for different configurations, the first Biot resonance of $u160$ is observed approximately between 500 and 600Hz. It has very little influence on the sound absorption coefficient trend of growth.

In general, the optimized configuration is not unique. It has to be chosen according to the frequency range of interest. Increasing the size of the inclusion, the sound absorption coefficient is improved at higher frequency, but it can be decreased at lower frequency. The optimal configuration depends on the application.

Effect of inclusions

The effect of a poroelastic inclusion compared to a perforation is represented in Fig. 4.16. The peak of absorption around 800Hz (configuration A) and 900Hz (configuration B) is higher in the case of double porosity. However, two issues clearly confirm the gain that can be obtained by the use of inclusions:

- at lower frequencies (up to $400 - 600$Hz in this case), where the performances of porous materials are usually worse, the absorption is increased if compared to double porosity and the loss to the original material is negligible or in any case smaller than in the case of double porosity;

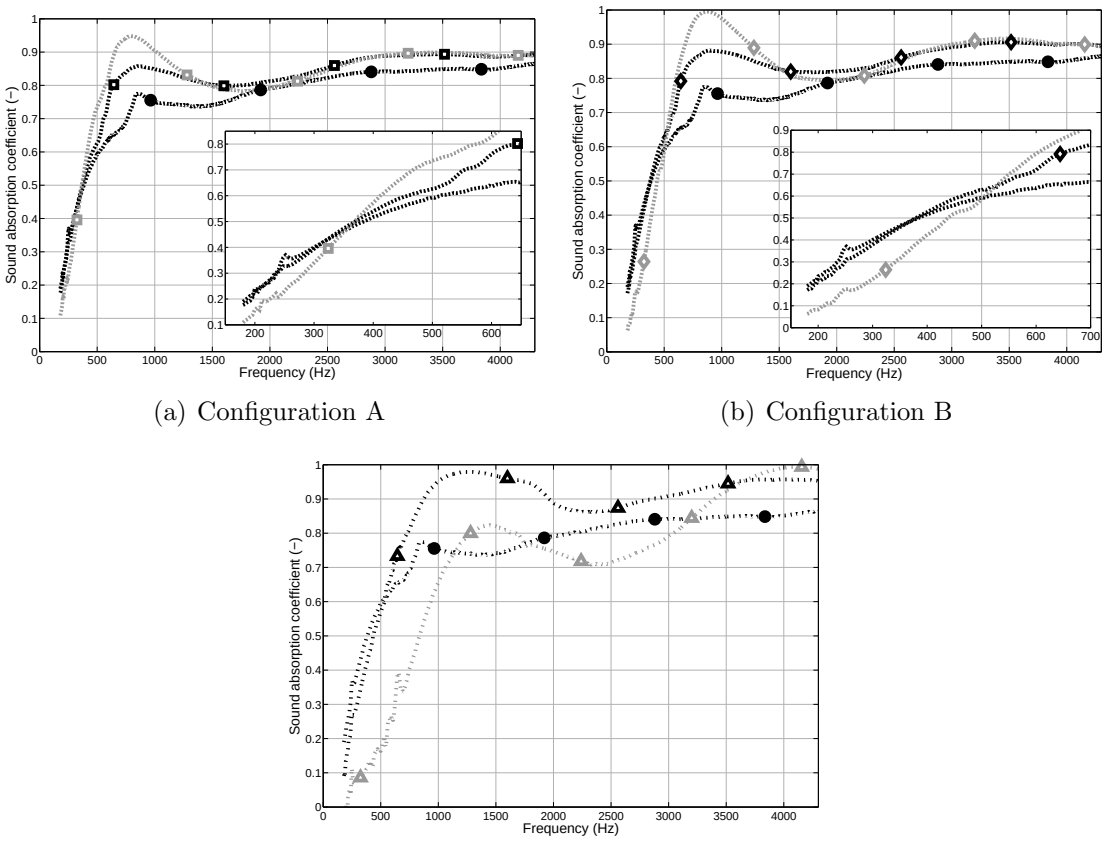

(a) Configuration A

(b) Configuration B

(c) Configuration C

Figure 4.16: Small Kundt Tube, 45mm thick layer, influence of a melamine inclusion - comparison between double porosity (dotted grey), heterogeneous material with inclusion of melamine (dotted black) and the homogeneous $u160$ (⋯●⋯). The curve markers are the same as in Fig. 4.14 and 4.15

- at higher frequencies (above 800Hz) the behavior is smoother than in the case of double porosity as the peaks and the dips are less pronounced: the global effect is better.

Moreover, for configuration C (i.e. when the size of the perforation/inclusion is larger) the sound absorption coefficient is clearly increased in the largest part of the measured frequency range (up to 3700Hz) by the use of the inclusion, if compared to the case of perforation. In this case a bigger surface participates to the pressure diffusion (Section 4.2.2), that is a positive effect. However, due to the increased size of the perforation, this effect is not sufficient to have a consistent absorption at low frequency in the case of double porosity; this result is obtained instead by the use of the inclusion, the perforation being replaced by an increased amount of material.

4.4.2 Medium Kundt tube

Four different shaped samples (Tab. 6.1) have been tested. The samples have similar

Configuration	External cross section		Internal cross section		Mesoporosity	Thickness
	Shape	Dimension (mm)	Shape	Dimension (mm)	(-)	(mm)
A	circular	$r = 50$	square	$l = 21$	0.056	45.5
B	circular	$r = 50$	square	$l = 30$	0.115	45.5
C	circular	$r = 50$	square	$l = 55.5$	0.392	45.5
D	circular	$r = 50$	circular	$r = 23$	0.212	45.5

Table 4.4: Medium Kundt Tube geometries

mesoporosity than in the case of the Small Kundt Tube. However, the size is different (therefore a different amount of material participates in the absorption process) and the sample is 45.5mm thick instead of 45mm. For those reasons, some small differences are observed.

Effect of mesoporosity

The effect of a mesoporosity variation is represented in Fig. 4.17. Asymmetry of the samples has been tested. In particular the cylinder radius was not constant. With a small gap of the air on the back, the measurement is not compromised. In order to rotate the sample and verify the asymmetry, some teflon has been used for the boundary. The results are more precise with the teflon than without and more similar to the case of the gaps on the back, but the elastic properties are modified. Comparing the results to the case of the small tube, the curves have the same shape. The sound absorption is a bit smaller than the one measured in the small tube for similar mesoporosity. This is due to the reason explained above and to the fact that mesoporosities are not exactly equal and tolerances must be taken into account. The relative difference between the configurations A and B is maintained for both double porosity and heterogeneous case. The effect of a mesoporosity variation described above is confirmed.

Effect of inclusions

The relative difference between the double porosity and heterogeneous cases are maintained for both configurations A and B. The effect of the melamine inclusion described above is confirmed.

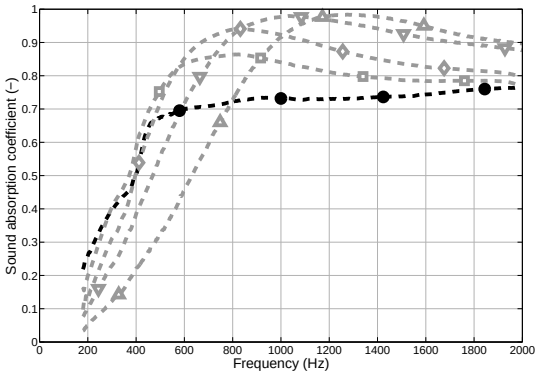

(a) Double porosity - configurations A (--□--), B (--◇--), C (--△--) and D (--▽--)

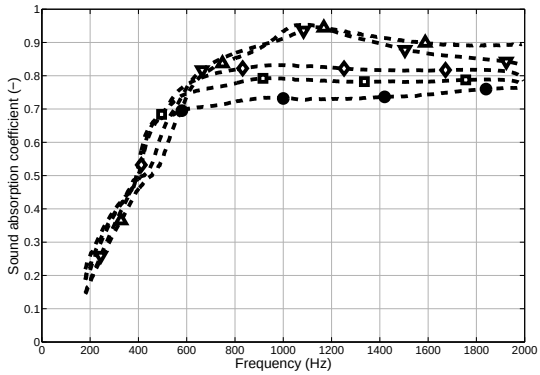

(b) U160 with a melamine inclusion - configurations A (--□--), B (--◇--), C (--△--) and D (--▽--)

Figure 4.17: Medium Kundt Tube, 45.5mm thick layer - influence of the mesoporosity: different configurations compared to the homogeneous $u160$ (···●···)

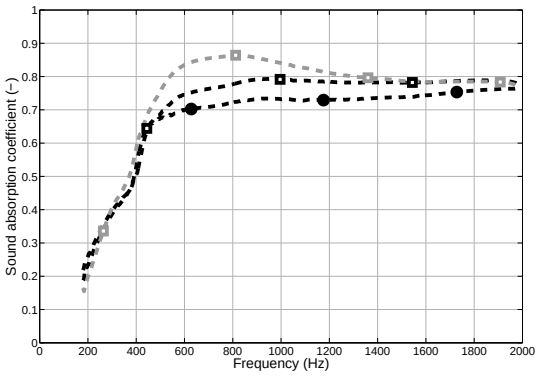

(a) Configuration A

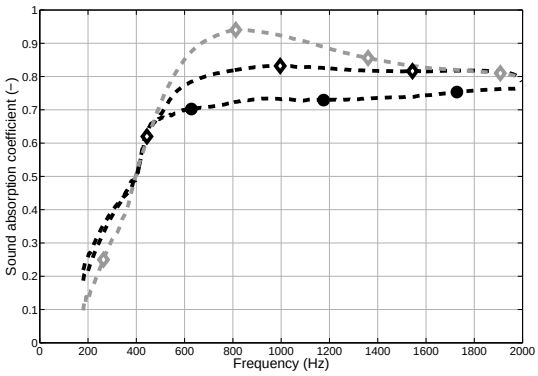

(b) Configuration B

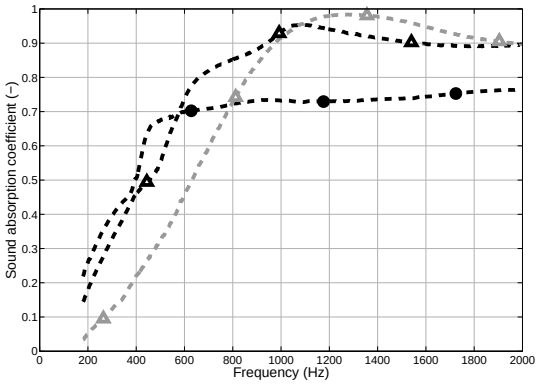

(c) Configuration C

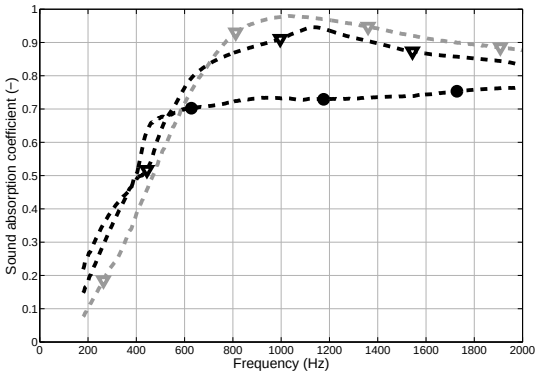

(d) Configuration D

Figure 4.18: Medium Kundt Tube, 45.5mm thick layer, influence of a melamine inclusion - comparison between double porosity (dashed grey), heterogeneous material with inclusion of melamine (dashed black) and the homogeneous $u160$ (···●···). The curve markers are the same as in Fig. 4.17(a) and 4.17(b)

Comparison between Small and Medium Kundt Tube

Tables 4.3 and 6.1 show for the two standing wave tubes very similar values of mesoporosity, in the case of square cross-section. This choice was done to verify directly the importance of mesoporosity. Increasing the absolute dimensions of the samples, at constant mesoporosity, a similar behavior is expected, due to the crucial role played by mesoporosity, as clear from the analytical model. However, a small modification in the absorption effects has to be considered, for the following reasons:

- the pressure diffusion effect depends also on the geometric dimensions (through Eq. 4.21 and 4.23) and not only on the mesoporosity;
- the condition of high or low permeability contrast depends on the dimension of the inclusions and the situation can be different between Small and Medium Kundt Tube, as will be discussed in 4.5.2;
- in practice, the boundary conditions could be slightly different in the two tubes.

For both cases of double porosity and heterogeneous material, small differences are observed when the dimensions of the sample are changed between Small and Medium Kundt Tube, confirming that the most important parameter is mesoporosity. Fig. 4.19 show that the sound absorption coefficient is quite close over the frequency range, between the cases of SKT and of MKT, when the value of mesoporosity is equal.

4.4.3 Big Kundt Tube

Experimental tests in the Big Kundt Tube are important to verify the validity of the homogenization theory [39, 40]. Only when a consistent number of cells is present, the theoretical hypotheses are valid. In the case of double porosity or heterogeneous materials with inclusions, the results obtained in the Small Kundt Tube for a single cell are revealing but it should be verified that they are preserved in the passage from a single cell to a complete layer.

Number of cells	**Cell external cross section**		**Cell internal cross section**		**Mesoporosity**
	Shape	Dimension (mm)	Shape	Dimension (mm)	(-)
6×6	square	$l = 100$	circular	$r = 29$	0.264

Table 4.5: Big Kundt Tube geometry for the samples characterized by a frame of $u160$

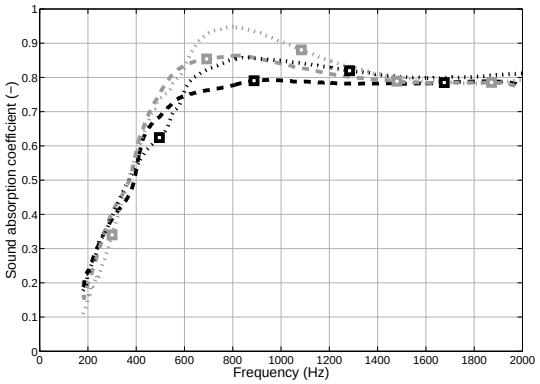

(a) Configuration A, $\phi_p = 0.06$: double porosity in the SKT (····□····) and in the MKT (– –□– –), heterogeneous material in the SKT (·–□–·) and in the MKT (– –□– –)

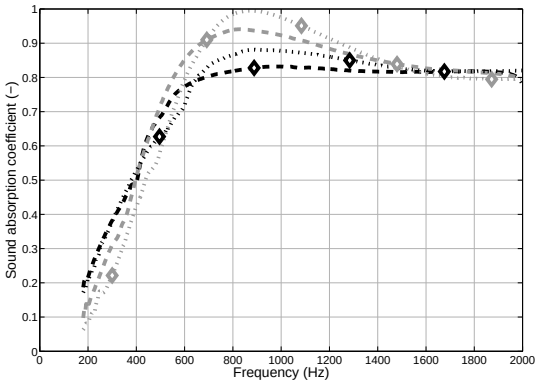

(b) Configuration B, $\phi_p = 0.12$: double porosity in the SKT (····◇····) and in the MKT (– –◇– –), heterogeneous material in the SKT (·–◇–·) and in the MKT (– –◇– –)

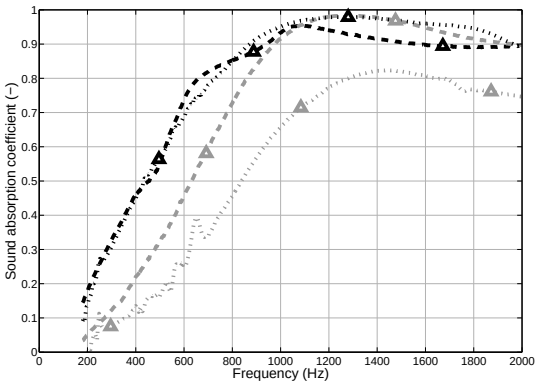

(c) Configuration C, $\phi_p = 0.38$: double porosity in the SKT (····△····) and in the MKT (– –△– –), heterogeneous material in the SKT (·–△–·) and in the MKT (– –△– –)

Figure 4.19: Influence of mesoporosity: comparison of the sound absorption coefficient measured for samples having approximately equal mesoporosity, for both double porosity and heterogeneous material

u160 as a frame material

The case with $u160$ as original microporous material to be filled with *melamine* is here presented.

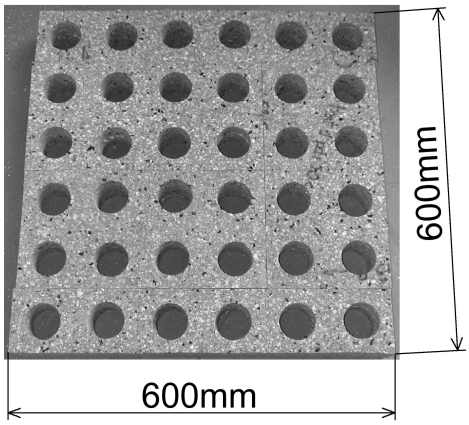

Figure 4.20: 90mm thick $u160$ sample in the Big Kundt Tube: the frame

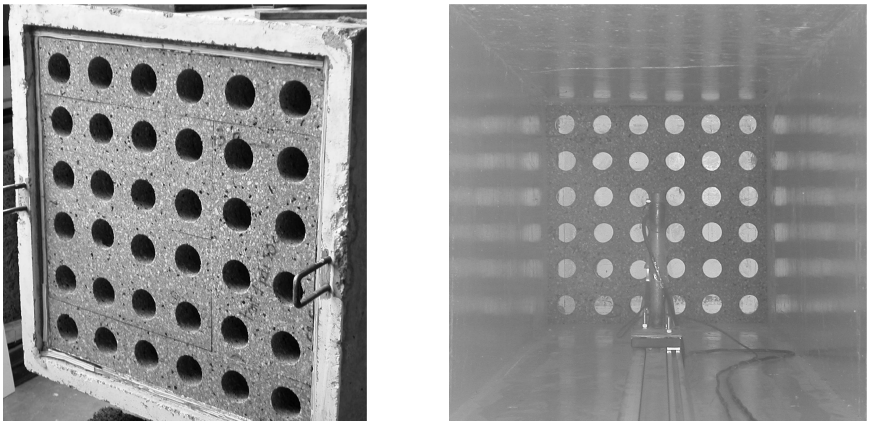

(a) Exterior view (b) Interior view

Figure 4.21: 90mm thick double porosity ($u160$) sample in the Big Kundt Tube

The cross section of the Big Kundt Tube is a 600×600mm square (see Tab. 4.5). The size of the cell (10×10mm) has been chosen to have a similar aspect ratio if compared to the samples of the middle Kundt tube. The size of the perforation has been chosen among the available values in practice, from the experience of the previous tests. A radius of 29mm represents a good compromise in mesoporosity (0.264): large enough to permit the diffusion effects, but not too large to prevent losses at low frequency.

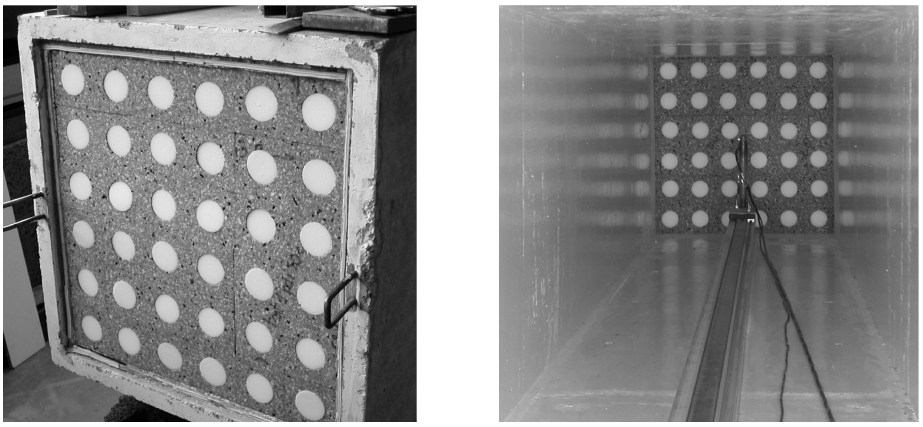

(a) Exterior view (b) Interior view

Figure 4.22: 90mm thick heterogeneous ($u160$ - *melamine*) sample in the Big Kundt Tube

The measured curves are presented in Figure 4.24. The small dips appearing in all the curves at the same frequencies, making them slightly discontinuous, can be explained as plate resonances, due to the absence of scotch at the back of the layer.

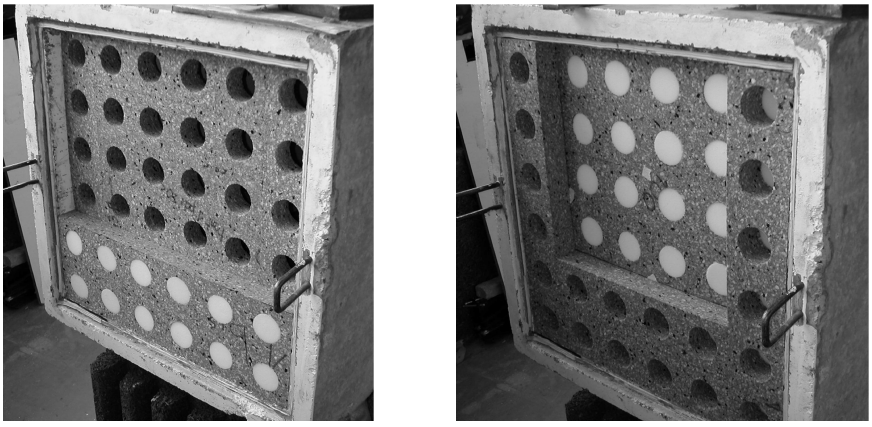

(a) Double porosity - heterogeneous (b) Heterogeneous - double porosity

Figure 4.23: Preparation of the 90mm thick heterogeneous ($u160$ - *melamine*) hybrid sample in the Big Kundt Tube

The results show a similar behavior than the one observed in the smaller Kundt tubes: the typical pattern for the double porosity curve, and a good gain for the heterogeneous material. In fact, above 350Hz double porosity provides an higher absorption coefficient, but the inclusions permit a good gain if compared to double porosity at low frequency and almost no loss to the original $u160$ layer. In general, on a larger frequency range, the heterogeneous material show the best performance.

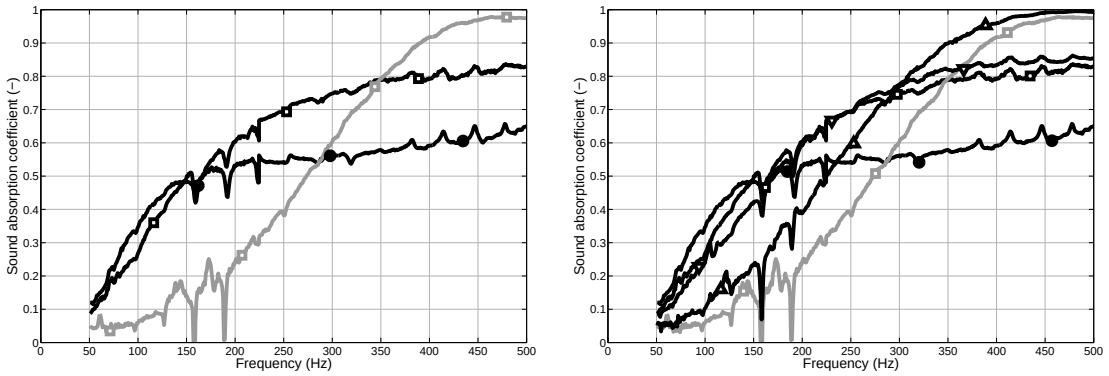

(a) Cases of double porosity (—□—) and $u160$ - *melamine* heterogeneous material (—■—), compared to the homogeneous $u160$ (—●—)

(b) As in figure 4.24(a), with two hybrid solutions: a 45mm thick double porosity layer in the front and a 45mm thick $u160$ - *melamine* heterogeneous layer in the back (—△—) and the vice versa (—▽—)

Figure 4.24: Big Kundt Tube, 90mm thick layer, influence of the inclusions

The hybrid solutions, built up by placing side by side a double porosity 45mm thick layer and an heterogeneous 45mm thick layer, appear as an interesting compromise. In this case, the measured absorption curves are between the double porosity and the heterogeneous case. The resulting curve is mainly driven by the first layer encountered by standing wave, but an improvement can be seen if compared to the original cases. As already pointed out, the optimization depends on the frequency target. For example, the hybrid —△— configuration is better than the double porosity layer for the measured frequency range, but is still worse than the original $u160$ below 230Hz. The configuration —▽— is very close to the regular heterogeneous solution: some absorption can be gained above 250Hz, but there is a small loss below 200Hz.

rockwool as a frame material

The case with *rockwool* as original microporous material to be filled with *melamine* is here presented. With this material, two different mesoporosities have been investigated, as resulting from a 90mm thick sample characterized by a 6×6 or by a 7×7 periodical cells geometry (Table 4.6 and Fig. 4.25 and 4.26). The results show a similar behavior

than the one observed for the case of $u160$: the typical pattern for the double porosity curve, and a good gain for the heterogeneous material. It has also been shown that in the case of 7×7 holes (i.e. when mesoporosity is increased if compared to the case of 6×6 holes) the configuration is closer to an optimized solution in the frequency range

Number of cells	**Cell external cross section**		**Cell internal cross section**		**Mesoporosity**
	Shape	Dimension (mm)	Shape	Dimension (mm)	(-)
6×6	square	$l = 100.0$	circular	$r = 29$	0.264
7×7	square	$l = 85.7$	circular	$r = 29$	0.360

Table 4.6: Big Kundt Tube geometry for the samples characterized by a frame of *rockwool*

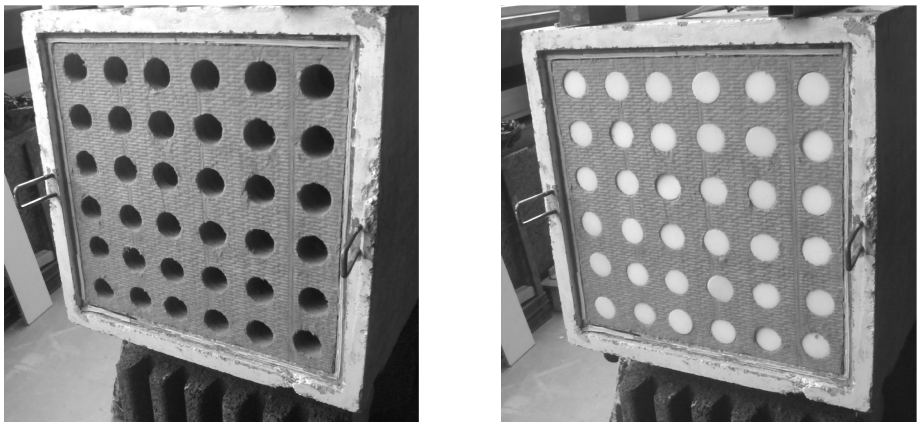

(a) Double porosity

(b) Heterogeneous (with inclusions of *melamine*)

Figure 4.25: 90mm thick 6×6 periodical cells *rockwool* sample in the Big Kundt Tube

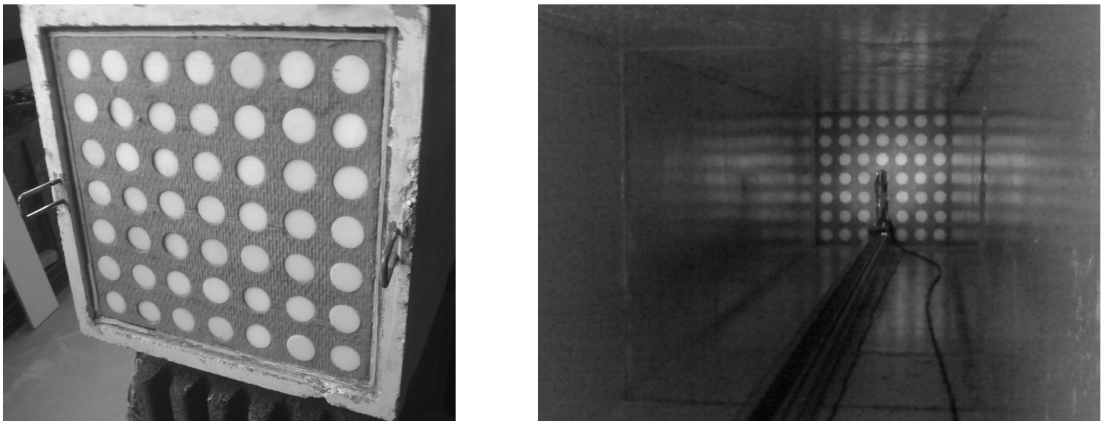

(a) Heterogeneous (with inclusions of *melamine*), exterior view

(b) Heterogeneous (with inclusions of *melamine*), interior view

Figure 4.26: 90mm thick 7×7 periodical cells *rockwool* sample in the Big Kundt Tube

$0 - 500$Hz. In fact, for these frequencies, the heterogenous curve is always above the double porosity one.

The hybrid solutions provide the same effects as discussed in 4.4.3.

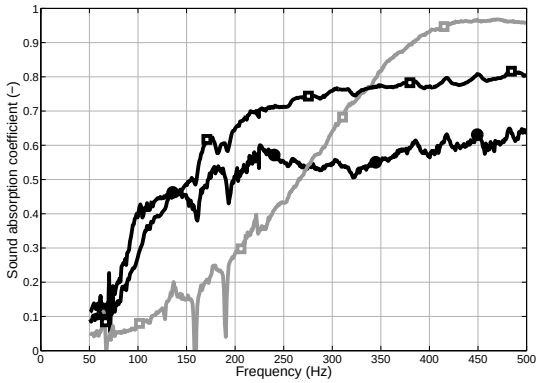

(a) Configuration with 6×6 perforations, cases of double porosity (—□—) and *rockwool* - *melamine* heterogeneous material (—□—), compared to the homogeneous *rockwool* (—●—)

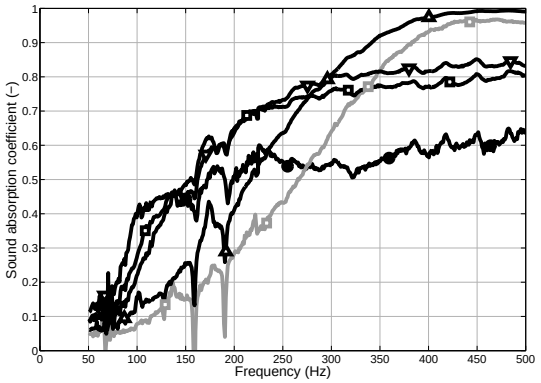

(b) As in figure 4.27(a), with two hybrid solutions: a 45mm thick double porosity layer in the front and a 45mm thick *rockwool* - *melamine* heterogeneous layer in the back (—△—) and the vice versa (—▽—)

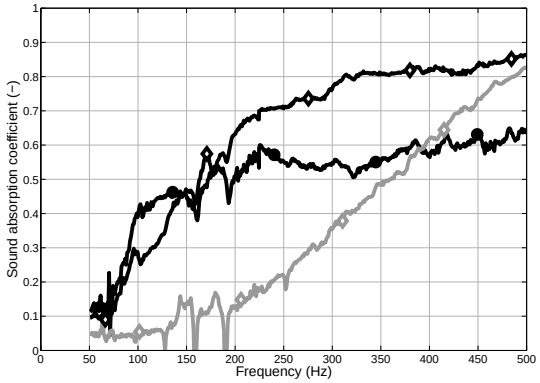

(c) Configuration with 7×7 perforations, cases of double porosity (—◇—) and *rockwool* - *melamine* heterogeneous material (—◇—), compared to the homogeneous *rockwool* (—●—)

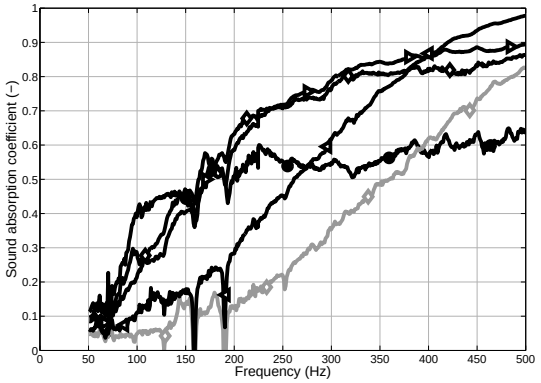

(d) As in figure 4.27(c), with two hybrid solutions: a 45mm thick double porosity layer in the front and a 45mm thick *rockwool* - *melamine* heterogeneous layer in the back (—◁—) and the vice versa (—▷—)

Figure 4.27: Big Kundt Tube, *rockwool* as frame microporous material, 90mm thick layer: influence of the inclusions

4.5 Validation of the analytical model

In the following part, the analytical model described in Chapter 4.2 is compared to the experimental data, for the measurements described in Chapter 4.4. The rigid frame Johnson-Lafarge model is used as base for the analytical prediction (see 4.2 for details). The acoustical parameters (Johnson-Lafarge model) are presented in Table 4.1. For the case of double porosity, the model described in [49] (from which the analytical model described in Chapter 4.2 is derived) is used.

4.5.1 Periodical cells in the Big Kundt Tube

The model described in Section 4.2 has been used to predict the sound absorption coefficient for the configurations tested in the Big Kundt Tube (Section 4.4.3), with $u160$ as microporous material acting as a frame.

There is a good agreement between experimental data and analytical prediction. The homogenization hypotheses of the analytical model are represented with a good approximation in the experimental data by the presence of the 6×6 network of cells. The analytical calculation refers to the case of a circular-shaped inclusion into a square-shaped cell, as in Equation 4.21: the geometrical configuration (Tab. 4.5) is well represented. A thickness of 91mm is considered instead of the 90mm nominal thickness, due to tolerances and mounting conditions.

The diffusion effect is taken into account by Eq. 4.19. For the case of double porosity the model described in [49] is taken into account; for the case of inclusions, the analytical Equations can be found in Section 4.2.
When only one layer is considered (independently from his nature, double porosity or heterogeneous material), the surface impedance Z_S in Eq. 4.6 can be considered infinite. Thus Eq. 4.6 is reduced to:

$$Z_h = -jZ_C \cot ke \tag{4.26}$$

When several layers are considered, Eq. 4.26 has to be used for the first layer, backed by a rigid wall. When other layers are added side by side, for each new layer Eq. 4.6 has to be recalculated to obtain the new surface impedance for the layer, until the last external layer. With this method, a multi-layer characterized by a number of layers as large as wanted can be calculated.

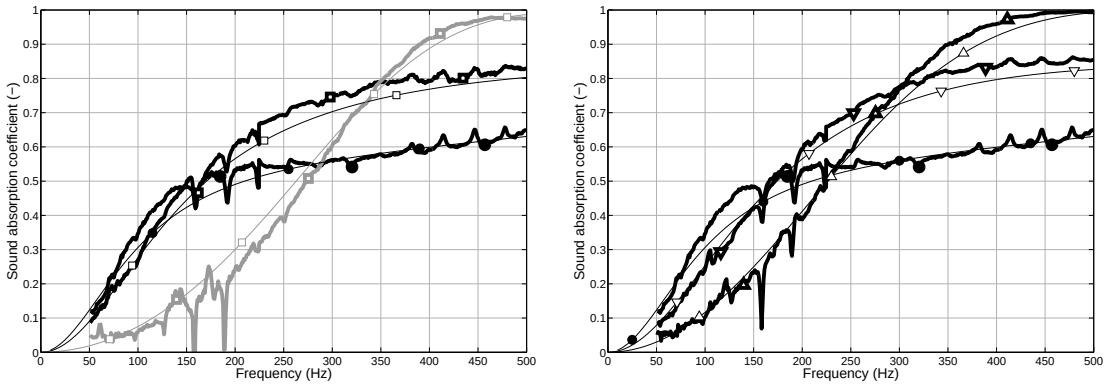

(a) Comparison between experimental (solid line) and analytical (thin line) data: single porosity *u*160 (—●— and —●—), double porosity *u*160 (—□— and —□—), heterogeneous *u*160 - *melamine* (—■— and —□—)

(b) Comparison between experimental (solid line) and analytical (thin line) data: single porosity *u*160 (—●— and —●—), hybrid configuration with double porosity *u*160 in front and heterogeneous *u*160 - *melamine* on the back (—△— and —△—), hybrid configuration in vice versa (—▽— and —▽—)

Figure 4.28: Big Kundt Tube, 90mm thick layer composed of *u*160 and *melamine* , validation

The former is the case when hybrid solutions are considered (two layers are involved): the total impedance of a 90mm thick hybrid layer is obtained by Equation 4.26 applied to the first 45mm thick layer (for example double porosity layer in Fig. 4.23(a)) and Eq. 4.6 for the second 45mm thick layer (for example double porosity layer in Fig. 4.23(a)).

The small difference between the analytical and the experimental curves in Fig. 4.28 can be ascribed to the axial tolerance of the perforations. In fact, some small misalignments are produced in practice, their effect being a small increase of the geometrical area that acts in the diffusion process and therefore a small increase of the sound absorption coefficient.

Moreover, eventual small gaps of air due to tolerances during the mounting phase, in general do not deteriorate the absorption properties. Considering these two issues, the use of inclusions should result in a robust methodology also for practical applications.

The intersections between analytical curves in Fig. 4.28(a) are approximately at the same frequencies than the corresponding intersections between experimental curves: the analytical model predicts well the frequency ranges when a configuration (double porosity, heterogeneous, etc.) is performing better than another one.

The good agreement already experienced for single layer configurations (Fig. 4.28(a)) is confirmed for the hybrid configurations also: Fig. 4.28(b).

4.5.2 Single cell in the Small Kundt Tube

The analytical calculation refers to the case of a square-shaped (configurations A, B, C from Tables 4.3) or circular-shaped (configuration D in Tables 4.3) perforation or inclusion into a circular-shaped cell. The expression for $D(0)$ (Eq. 4.21) is now adapted from the square (external) - circular (internal) case. Equivalent areas are considered: the dimension a represents the size of a square whose area is the same as the one of the circular cross-section of the Tube.

The validity of this criterion is confirmed by Tarnow paper, where the geometrical expression of Eq. 4.21 is calculated. In [34], referring to the flux analogy, the boundary conditions are imposed on a circular cell, with equivalent area, because the direct analytical integration does not exist for the case of a square cell. The results shown in this Section confirm that this choice represent a good approximation. Additional details are discussed in the conclusions (4.5.5). For configurations A and B, there is a good agreement between experimental data and analytical prediction (Fig. 4.29 and 4.30), provided that the diffusion function F_d (see 4.2.2) is set to 1. On the other hand, the prediction is worse when the complete expression for F_d, Eq. 4.19, is taken into account. These considerations are valid for both cases of double porosity and melamine inclusions. Physically, the diffusion effect is not well represented in the Small Kundt Tube. This fact can be explained by the following reasons:

- the layer is not periodic as in the Big Kundt Tube, but only one cell is considered, therefore one of the hypotheses of the homogenization theory is not respected;
- the external cross section is circular and not square, thus enlarging the difference between the real sample and an ideal periodic layer;
- in all the experimental cases, the separation between micro and meso scales is sufficient to satisfy the second homogenization hypothesis [40] that imposes at least $l_m/l_p < 10^{-1}$ (Table 4.7), but the permeability contrast in some cases is not high enough.

The last explanation is more clear if the description in [40] is considered: for $l_m/l_p \approx 10^{-1}$, there is a *low static permeability contrast* between pores and micropores; for $l_m/l_p \approx 10^{-3}$, there is a *high static permeability contrast*. Table 4.7 show that the first situation occurs clearly in the Big Kundt Tube; in the Small Kundt Tube, two different situations must be considered, due to the value of l_m/l_p that is not a priori clearly referable to one of the two situations. For configurations A and B (small perforation

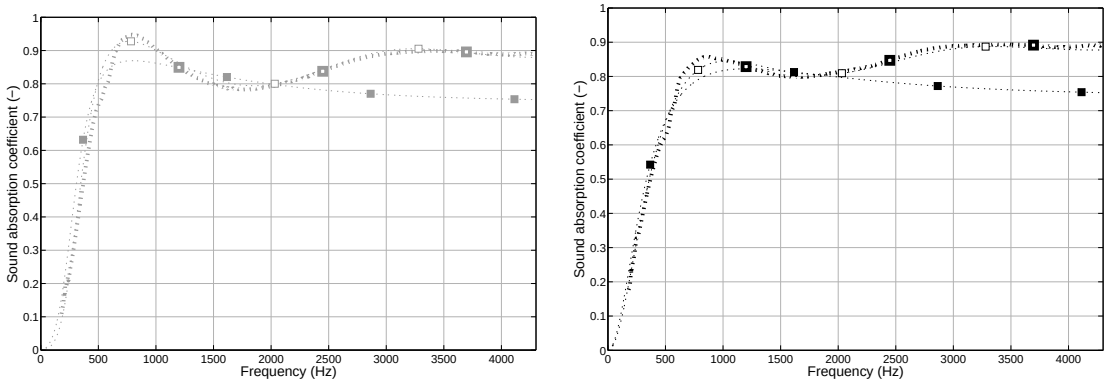

(a) Configuration A, double porosity: comparison between experimental data (----□----) and analytical model in case of $F_d = 1$ (----□----) and $F_d = F_d(\omega)$ (----■----)

(b) Configuration A, heterogeneous material: comparison between experimental data (----□----) and analytical model in case of $F_d = 1$ (----□----) and $F_d = F_d(\omega)$ (----■----)

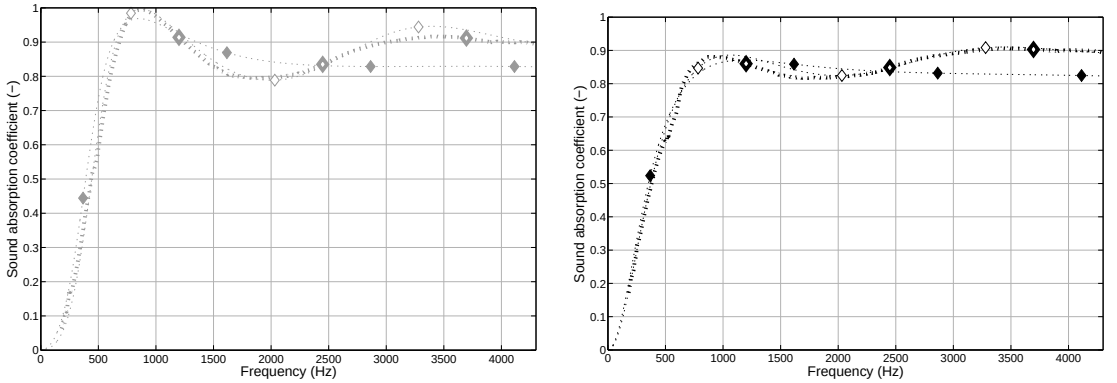

(c) Configuration B, double porosity: comparison between experimental data (----◇----) and analytical model in case of $F_d = 1$ (----◇----) and $F_d = F_d(\omega)$ (----◆----)

(d) Configuration B, heterogeneous material: comparison between experimental data (----◇----) and analytical model in case of $F_d = 1$ (----◇----) and $F_d = F_d(\omega)$ (----◆----)

Figure 4.29: Small Kundt Tube, 45mm thick layer, validation for configurations A and B

and inclusion), l_m/l_p is closer to the order 10^{-1}: in fact the prediction with $F_d = 1$ is good (Fig. 4.29). Moreover, the diffusion effect appears to be more consistent when the internal cross-section is enlarged (configurations C and D, Fig. 4.30). In this case, the separation of scales between micro and meso is more clear and the diffusion effect appears, due to the larger contact surface between *u*160 and *melamine* (or between *u*160 and air). The analytical predictions are satisfactory if the complete expression for F_d is considered.

The prediction of a *high/low static permeability contrast*, that is here evaluated through theoretical observations, will be confirmed in a further Report by the numerical calculations. In fact, a FEM model is a closer representation of the reality from this point of

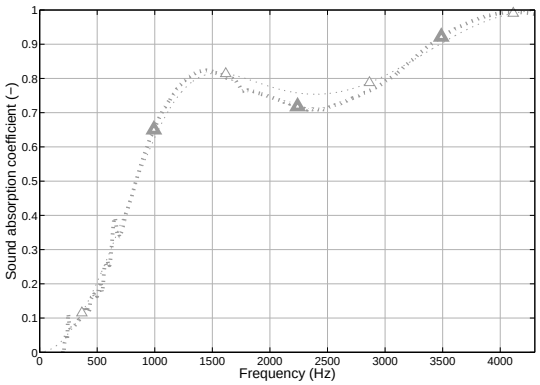

(a) Configuration C, double porosity: comparison between experimental data (----△----) and analytical model in case of $F_d = F_d(\omega)$ (----△----)

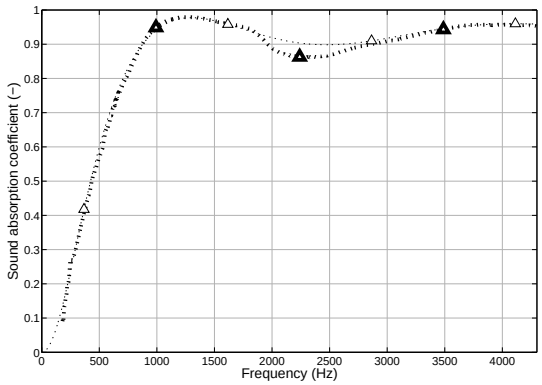

(b) Configuration C, heterogeneous material: comparison between experimental data (----▽----) and analytical model in case of $F_d = F_d(\omega)$ (----▽----)

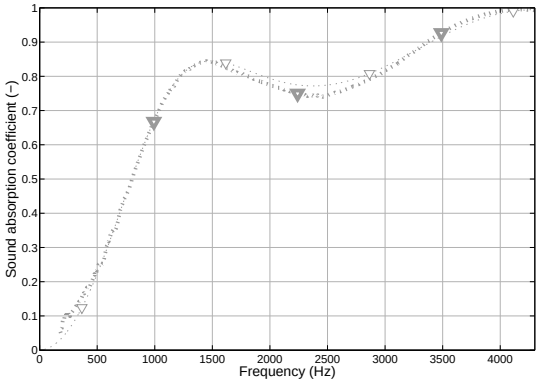

(c) Configuration D, double porosity: comparison between experimental data (----▽----) and analytical model in case of $F_d = F_d(\omega)$ (----▽----)

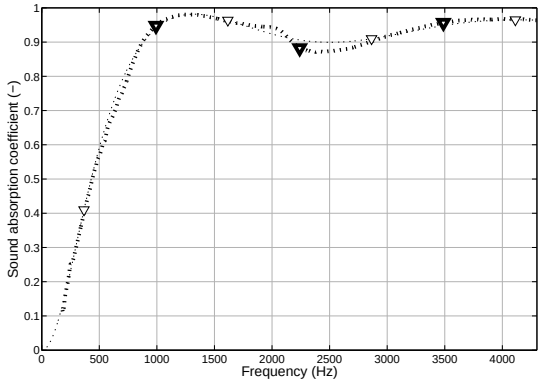

(d) Configuration D, heterogeneous material: comparison between experimental data (----▽----) and analytical model in case of $F_d = F_d(\omega)$ (----▽----)

Figure 4.30: Small Kundt Tube, 45mm thick layer, validation for configurations C and D

view, because the diffusion effect is a direct consequence of the geometrical modeling.

Another estimation of the diffusion effect is given by the wavelength in the microporous material. The key point in the case of high permeability contrast, is that the wavelength in the microporous domain is of the same order of magnitude as the mesoheterogeneities [40]. The situation is depicted in Fig. 4.31: with this criterion in the case of the Big Kundt Tube, the diffusion effect is expected already at low frequencies. On the other hand, in the Small Kundt Tube the criterion gives similar results to the analysis of the ratio l_m/l_p. For configurations A and B an eventual diffusion effect would exist only at higher frequencies in the range of interest; enlarging the mesoheterogeneities size, the diffusion can arise at lower frequencies.

Kundt Tube type	Configuration	Mesoporosity scale l_p (mm)	Interscale ratio l_m/l_p (-)	Permeability contrast	Diffusion frequency $f_d = \omega_d/2\pi$ (Hz)
Big Kundt Tube	6×6 cells	29.0	$6.9 \cdot 10^{-3}$	HIGH	1070
Small Kundt Tube	A	5.0	$8.0 \cdot 10^{-2}$	LOW	1868
Small Kundt Tube	B	7.0	$5.7 \cdot 10^{-2}$	LOW	2891
Small Kundt Tube	C	12.5	$3.2 \cdot 10^{-2}$	HIGH	11118
Small Kundt Tube	D	14.5	$2.8 \cdot 10^{-2}$	HIGH	12348
Medium Kundt Tube	A	10.5	$3.8 \cdot 10^{-2}$	LOW/HIGH	381
Medium Kundt Tube	B	15.0	$2.7 \cdot 10^{-2}$	LOW/HIGH	598
Medium Kundt Tube	C	27.8	$1.4 \cdot 10^{-2}$	HIGH	2546
Medium Kundt Tube	D	23.0	$1.7 \cdot 10^{-2}$	LOW/HIGH	1044

Table 4.7: Homogenization conditions and static permeability contrast for the different tested samples

1

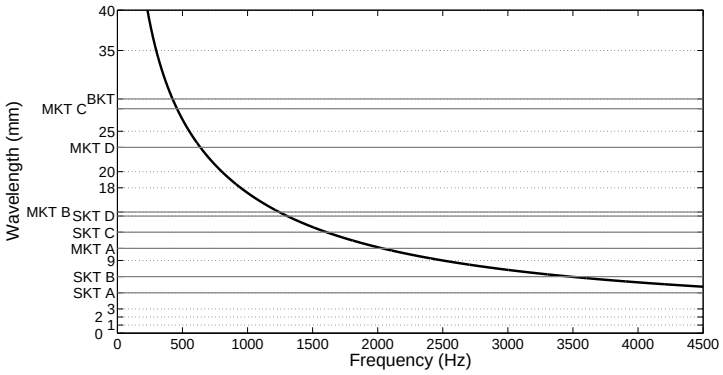

Figure 4.31: Wavelength in the $u160$ (rigid frame model) compared to the size of mesoheterogeneities: SKT refers to Small Kundt Tube, MKT to Medium and BKT to Big; A-B-C-D represent the configurations described in Tables 4.3 and 6.1.

In conclusion, even if the periodicity effect is not verified for a single circular-shaped cell, the analytical model supplies a good prediction, provided that the physical conditions (for example the ones of the experiment, for the validation case) are taken into account. The experimental analysis in the Small Kundt Tube showed anyhow interesting results, when a comparison between different configurations is done, involving different geometrical sizes and single porosity/double porosity/heterogeneous case (4.4.1). The geometrical conditions must be analyzed very carefully when an analytical model is concerned, especially about the involvement of the pressure diffusion effects. For a real application, it is strongly suggested to verify in the Big Kundt Tube the data obtained in the Small Kundt Tube, because in the former the physical hypotheses of the homogenization theory are not guaranteed.

4.5.3 Single cell in the Medium Kundt Tube

The effect described in the previous section is confirmed by the experimental/analytical comparison in the Medium Kundt Tube (Figs. 4.32 and 4.32). The analytical calculation refers to the case of a square-shaped (configurations A, B, C from Table 6.1) or circular-shaped (configuration D in Table 6.1) perforation or inclusion into a circular-shaped cell. For configurations A, B and D, it is not possible to define a clear situation between low

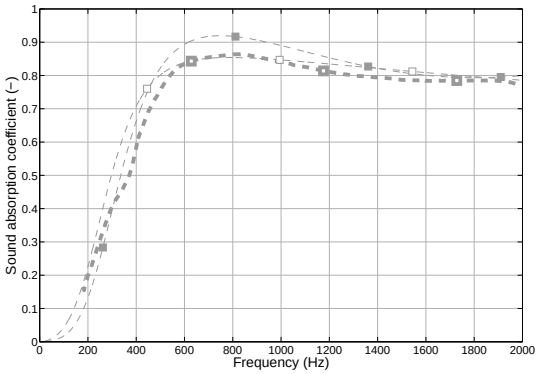

(a) Configuration A, double porosity: comparison between experimental data (--□--) and analytical model in case of $F_d = F_d(\omega)$ fixing $f_d = 1600$Hz (--□--) and $F_d = 1$ (----■----)

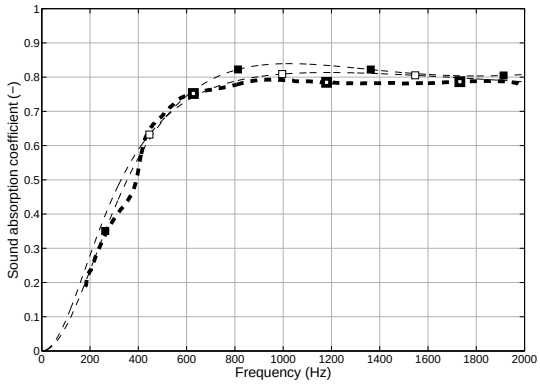

(b) Configuration A, heterogeneous material: comparison between experimental data (--■--) and analytical model in case of $F_d = F_d(\omega)$ fixing $f_d = 1600$Hz (--□--) and $F_d = 1$ (--■--)

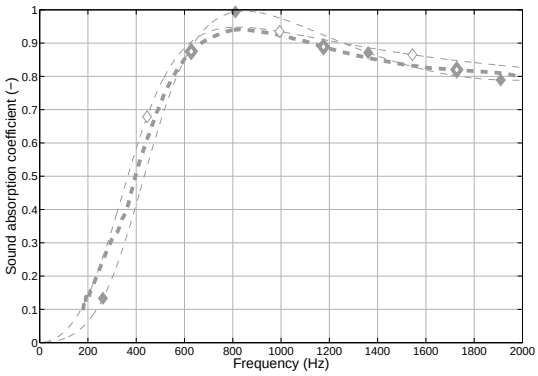

(c) Configuration B, double porosity: comparison between experimental data (--◇--) and analytical model in case of $F_d = F_d(\omega)$ fixing $f_d = 1900$Hz (--◇--) and $F_d = 1$ (--◆--)

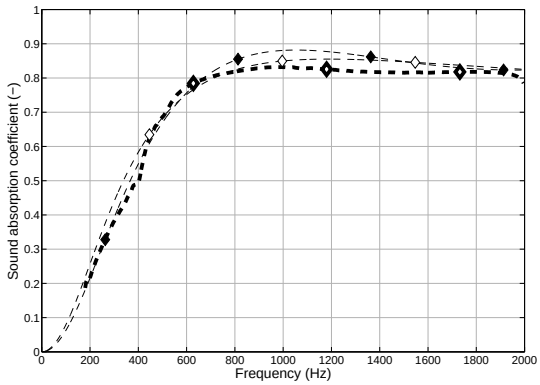

(d) Configuration B, heterogeneous material: comparison between experimental data (··◇··) and analytical model in case of $F_d = F_d(\omega)$ fixing $f_d = 1900$Hz (--◇--) and $F_d = 1$ (--◆--)

Figure 4.32: Medium Kundt Tube, 45.5mm thick layer, validation for configurations A and B

or high permeability contrast. In fact, as shown by Table 4.7, the ratio l_m/l_p is always of the order of 10^{-2}. Especially for configurations A and B, the situation is between the two cases, as Figure 4.32 show and resembles the case described by Olny [39]. The comparison

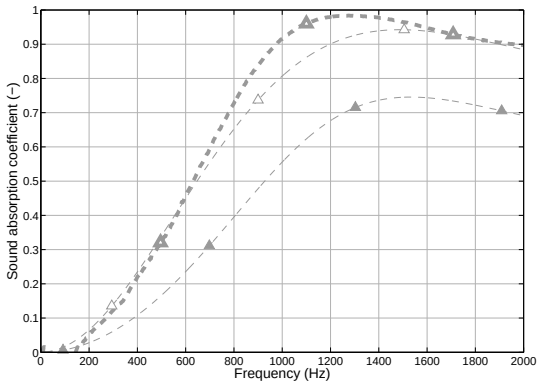

(a) Configuration C, double porosity: comparison between experimental data (--△--) and analytical model in case of $F_d = F_d(\omega)$ (--△--) and $F_d = 1$ (--▲--)

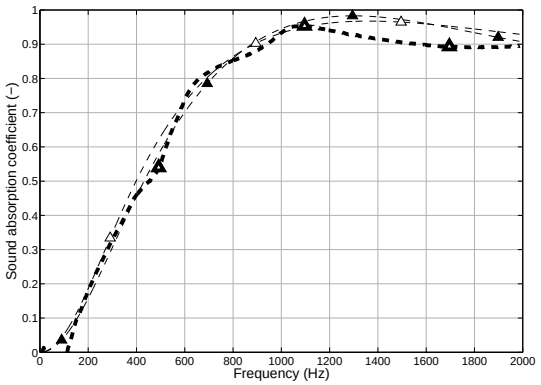

(b) Configuration C, heterogeneous material: comparison between experimental data (--△--) and analytical model in case of $F_d = F_d(\omega)$ (--△--) and $F_d = 1$ (--▲--)

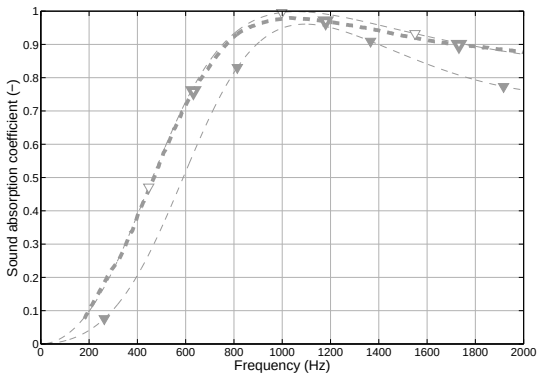

(c) Configuration D, double porosity: comparison between experimental data (--▽--) and analytical model in case of $F_d = F_d(\omega)$ fixing $f_d = 1800$Hz (--▽--) and in the generic case of $F_d = F_d(\omega)$ (--▼--), from which $f_d = 1044$Hz

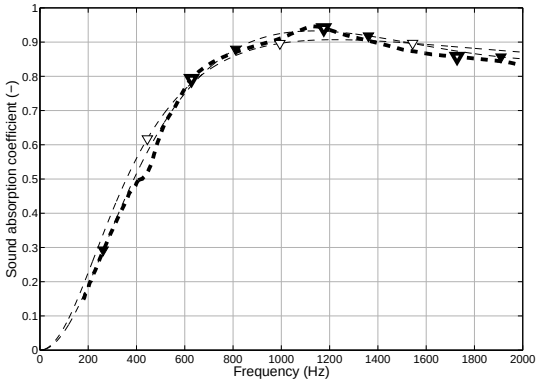

(d) Configuration D, heterogeneous material: comparison between experimental data (--▽--) and analytical model in case of $F_d = F_d(\omega)$ fixing $f_d = 1800$Hz (--▽--) and in the generic case of $F_d = F_d(\omega)$ (--▼--), from which $f_d = 1044$Hz

Figure 4.33: Medium Kundt Tube, 45.5mm thick layer, validation for configurations C and D

between the wavelength in the microporous domain and the mesoheterogeneities size confirms that the diffusion should arise at the tested frequencies. There is a pressure diffusion effect, but with the calculated diffusion frequency ω_d (Eq. 4.13) the analytical model does not provide a very good estimation. On the other hand, some diffusion is present because - differently than the configurations A and B in the Small Kundt Tube - the mesoporous dimensions are increased, the permeability contrast is not really low and considering $F_d = 1$ is not sufficient to provide a good estimation too. In this case, the model has to be validated and the effective ω_d has to be changed according to a good agreement between numerical and experimental. An easier estimation can be obtained

for configuration C, where the permeability contrast is higher and sufficient to show the modeled pressure diffusion effect, even if for double porosity the agreement is slightly worse (but in any case the best prediction can be obtained this way). In conclusion, the

Kundt Tube type	Configuration	Permeability contrast	Diffusion frequency $f_d = \omega_d/2\pi$ (Hz)	Diffusion function	Diffusion frequency adjustment	Corrected diff. freq. $\overline{f_d} = \overline{\omega_d}/2\pi$ (Hz)
Big Kundt Tube	6×6 cells	HIGH	1070	$F_d = F_d(\omega)$	NO	
Small Kundt Tube	A	LOW	1868	$F_d = 1$	NO	
Small Kundt Tube	B	LOW	2891	$F_d = 1$	NO	
Small Kundt Tube	C	HIGH	11118	$F_d = F_d(\omega)$	NO	
Small Kundt Tube	D	HIGH	12348	$F_d = F_d(\omega)$	NO	
Medium Kundt Tube	A	LOW/HIGH	381	$F_d = F_d(\omega)$	YES	1600
Medium Kundt Tube	B	LOW/HIGH	598	$F_d = F_d(\omega)$	YES	1900
Medium Kundt Tube	C	HIGH	2546	$F_d = F_d(\omega)$	NO	
Medium Kundt Tube	D	LOW/HIGH	1044	$F_d = F_d(\omega)$	YES	2200

Table 4.8: Homogenization conditions and diffusion function for the different tested samples

cases in the Big Kundt Tube (Section 4.5.1 and also next Section 4.5.4 where *rockwool* is used instead of *u*160) can be faced easily with the general analytical model. The homogenization hypotheses are respected. Referring to Figs. 4.28, 4.29, 4.29, 4.32 and 4.33, Table 4.8 provides a summary of the physical conditions to be considered in order to obtain a satisfactory match between analytical prediction and experimental data. The separation between high and low permeability contrast is not distinct in some cases, but a general trend can be predicted when the interscale ratio is taken into account. This criterion is confirmed by the curves provided in the Figs.: for low permeability contrast the diffusion function has to be fixed to 1, and for high permeability contrast it has to follow the complete analytical model, in order to get a good analytical prediction. The behavior of some samples in the Medium Kundt Tube for which the situation is not clear require to have an intermediate value for the diffusion function, by directly fixing a different diffusion frequency.

With the criteria described, the agreement between experimental data and analytical calculations is in general good for all the configurations taken into account, also for the case of a single cell in the Small or Medium Kundt Tubes.

4.5.4 Periodical cells in the Big Kundt Tube - case of rockwool

In this case the model described in Section 4.2 has been used to predict the sound absorption coefficient for the configurations tested in the Big Kundt Tube, with *rockwool* as microporous material acting as a frame.

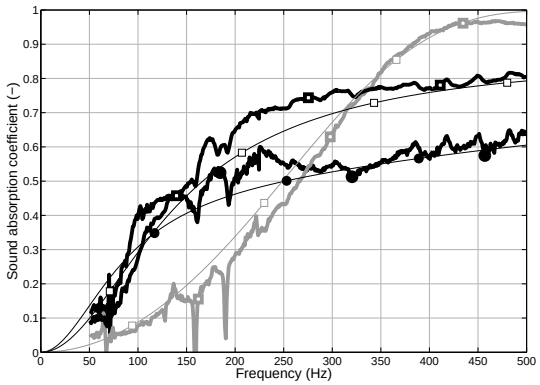

(a) 6×6 periodical cells, comparison between experimental (solid line) and analytical (thin line) data: single porosity *rockwool* (—●— and —●—), double porosity *rockwool* (—□— and —□—), heterogeneous *rockwool* - *melamine* (—□— and —□—)

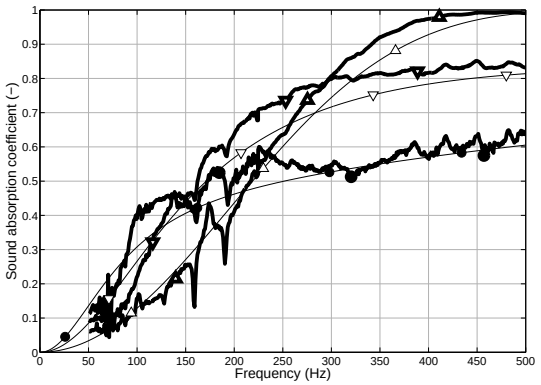

(b) 6×6 periodical cells, comparison between experimental (solid line) and analytical (thin line) data: single porosity *rockwool* (—●— and —●—), hybrid configuration with double porosity *rockwool* in front and heterogeneous *rockwool* - *melamine* on the back (—△— and —△—), hybrid configuration in vice versa (—▽— and —▽—)

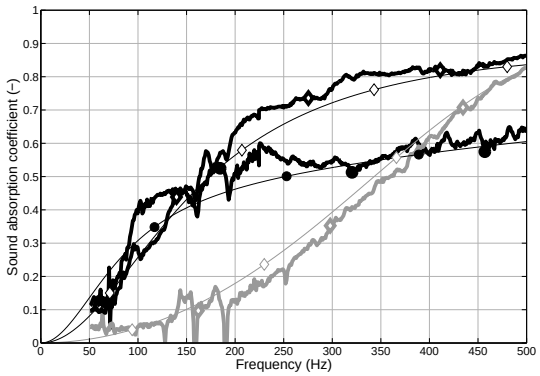

(c) 7×7 periodical cells, comparison between experimental (solid line) and analytical (thin line) data: single porosity *rockwool* (—●— and —●—), double porosity *rockwool* (—◇— and —◇—), heterogeneous *rockwool* - *melamine* (—◇— and —◇—)

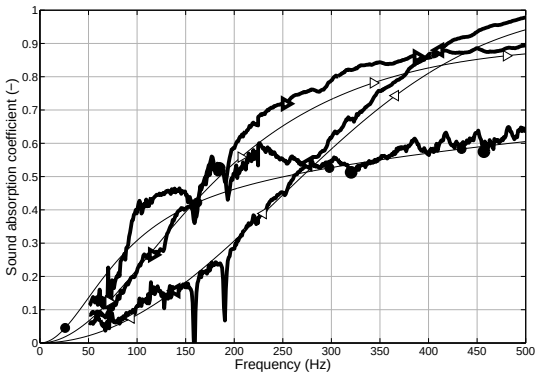

(d) 7×7 periodical cells, comparison between experimental (solid line) and analytical (thin line) data: single porosity *rockwool* (—●— and —●—), hybrid configuration with double porosity *rockwool* in front and heterogeneous *rockwool* - *melamine* on the back (—◁— and —◁—), hybrid configuration in vice versa (—▷— and —▷—)

Figure 4.34: Big Kundt Tube, 90mm thick layer composed of *rockwool* and *melamine* , validation

The results underlined in 4.5.1 are confirmed (Fig. 4.34): there is a good agreement between experimental data and analytical prediction, since the homogenization hypotheses are represented with a good approximation in the experimental data by the presence of a 6×6 and 7×7 networks of cells. The analytical model provides a good comparison

for all the configurations considered: 6×6 and 7×7, double porosity and heterogeneous material, two hybrid solutions.

As in case of $u160$, the small difference between the analytical and the experimental curves in Fig. 4.28 can be ascribed to the axial tolerance of the perforations. Some small gaps of air can lead also to this effect (as already underlined in 4.3.3, when comparing the pliability of *rockwool* to the one of $u160$), giving a slight overestimation of the experimental absorption curve.

As in case of $u160$, the intersections between analytical curves are approximately at the same frequencies than the corresponding intersections between experimental curves: the analytical model gives a good prediction when a comparison is done between different curves (e.g. cases of optimization).

4.5.5 Conclusions

The analytical model has been validated and has provided in general good agreement with the experimental results, for both cases of double porosity and in particular of heterogeneous inclusion. The results show that the extension from double porosity to inclusions is straightforward: the new analytical model for heterogeneities can be used with success, with the same characteristics and limits of the original double porosity model. For both cases, care must be taken about the physical interpretation of the pressure diffusion effects. In particular, it is important to verify:

- if the homogenization hypotheses are respected, considering the periodicity in the experimental setup and the relative micro/meso/macro dimensions;
- if the low or high permeability contrast is involved, through the analysis of the micro and meso dimensions, the analysis of the micro wavelength and the analysis of the diffusion frequency.

In some cases, as described in Sections 4.5.2 and 4.5.3, the knowledge of the pressure diffusion effects is not distinct. It would be important to have a better prediction of the effective behavior of the pressure in the system.

Some tries have already been done, in order to calculate an analytical value of $D(0)$ for different cross-sections (geometries more complicated than the square-circular case), but with no success. A simple investigation should be interesting. Using the flux analogy, a FEM calculation should be performed to obtain numerically the value of $D(0)$.

Extending this concept, the calculation could be performed for several geometries and dimensions, in order to create a simple abacus for $D(0)$. Also for this reason, the numerical calculation described in the following Chapter provide important information.

5 FEM simulation of porous materials with inclusions

The Finite Element (FEM) calculations have been performed to confirm the results obtained with the analytical predictions. In particular, the numerical simulations are used to obtain:

- a complete experimental/analytical/numerical comparison, to verify exhaustively the analytical prediction;
- an investigation of the eventual resonant effects due to the elasticity of the micro-porous materials;
- a direct simulation of the physical system, to verify that the supposed pressure diffusion effects and permeability contrast are correctly predicted.

A brief description of the numerical tools used is first given. Then, the results obtained are described and followed by conclusions.

5.1 FEM simulation

The code NOVA has been used for the simulations. The code is intended for the prediction of the vibro-acoustic behavior of elasto-poro-acoustic multilayered structures.

5.1.1 Theoretical background

The FEM code used is based on the mixed (u, p) formulation introduced by Atalla [5]. The Biot's equations are arranged to use the solid displacement and the fluid pressure

as main variables:

$$\nabla \cdot [\hat{\sigma}^s] + \omega^2 \tilde{\rho} \boldsymbol{u} + \tilde{\gamma} \nabla p = 0 \tag{5.1}$$

$$\triangle p + \omega^2 \frac{\tilde{\rho}_{22}}{R} p - \omega^2 \frac{\tilde{\rho}_{22}}{\phi^2} \tilde{\gamma} \nabla \cdot \boldsymbol{u} = 0 \tag{5.2}$$

where $[\hat{\sigma}^s]$ is a stress tensor depending only on the solid phase displacement and the following terms are defined:

$$[\hat{\sigma}^s] = \left(A - \frac{Q^2}{R} \right) \nabla \cdot \boldsymbol{u} \, [1] + 2N \, [\varepsilon^s] \tag{5.3}$$

$$\tilde{\gamma} = \phi \left(\frac{\tilde{\rho}_{12}}{\tilde{\rho}_{22}} - \frac{Q}{R} \right) \tag{5.4}$$

$$\tilde{\rho} = \tilde{\rho}_{11} - \frac{(\tilde{\rho}_{12})^2}{\tilde{\rho}_{22}}. \tag{5.5}$$

The tilde symbol over the Biot density factors indicates that the damping term is directly taken into account by the proper addition or subtraction in the expressions of ρ_{11}, $\rho 12$ and ρ_{22} [1].

This formulation allows for a reduction of the number of degrees of freedom compared to the (u, U) formulation and, in particular in the version that express directly the fluid flow , it accounts naturally for the coupling between different porous materials or between porous materials and air cavities. In fact, in this case there is no need to calculate coupling matrices between different domains of poroelastic materials or between a poroelastic material and an acoustic cavity. The calculation of the absorption coefficient is obtained in the code by applying rigid backing boundary condition on the first face of the layer, and applying a waveguide excitation on the second face. Then, the corresponding solid displacements and fluid pressures on the face excited are calculated and the sound absorption coefficient derived.

When a fluid or an equivalent fluid is involved, the Helmoltz equation is solved:

$$\triangle p + \omega^2 \frac{\rho}{K} p = 0 \tag{5.6}$$

like in the case of classical FEM solvers for acoustics.

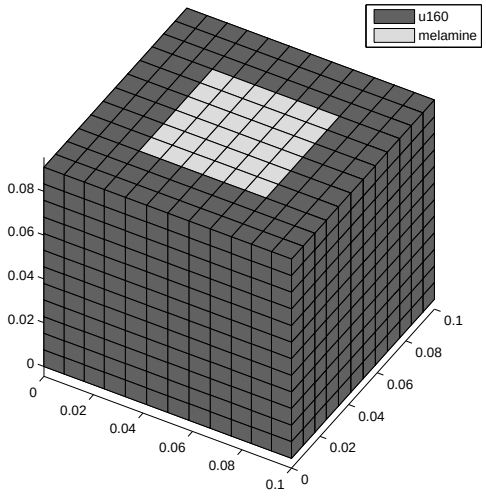

Figure 5.1: Example of a mesh for the Finite Elements calculation of an heterogeneous layer with an inclusion; in case of double porosity, the mesh of the *melamine* part is the same while the elements of the inclusion are fluid elements representing air.

5.1.2 The numerical model

The code used is intended for the prediction of the vibro-acoustic behavior of layered structures and uses simple meshing tools, that allow the discretization of the domain using brick finite elements with straight edges (the same as in [49]). In other words, two main limitations must be considered: the element type and the geometry. The restriction to planar layers does not represent a problem for the cases under study. However, with the tools available, the code can represent prismatic geometries only, derived from rectangular cuboids. $Hexa8$ (hexahedral) linear elements have been used to fill the rectangular cuboids. A circular shape would have been very difficult to represent.

For these reasons, only a simple configuration has been used, as depicted in Fig. 5.1 for the case of heterogeneous inclusions. A layer is composed of two materials and both double porosity and heterogeneous materials are considered. The external frame material is $u160$ and is represented by a poroelastic FEM modified (u, p) formulation. In case of double porosity, the internal material is air and is represented by a fluid acoustic FEM formulation based on Helmoltz equation. In case of heterogeneous inclusions, *melamine* is the internal material and is represented by a poroelastic FEM modified (u, p) formulation. The material characteristics are the same already presented in Table 4.1.

Numerical models have been constructed to represent the cases described in Chapter 4, for the Small, Medium and Big Kundt Tubes, for each of the configurations studied. The thicknesses are the same as for the measured samples. A square cross section has been used for both the external and the internal sections. The edge length is such that the surface of the model cover the same area as the samples with cross sections, i.e. to maintain equivalent areas and hence the same mesoporosity. The dimensions obtained are represented in Table 5.1 for the Small Kundt Tube, in Table 5.2 for the Medium Kundt Tube and in Table 5.3 for the Big Kundt Tube.

Referring to the wavelengths described in Chapter 4 (an approximate minimum value of 10mm, for the frequency range of interest), the rule of thumb of 6 linear elements per wavelength is difficult to respect already for the case of the Small Kundt Tube. The convergence has been verified, by using up to 15×15 elements in the in-plane directions and up to 20 elements in the thickness direction, for the configurations of Small and Middle Kundt Tubes.

For the case of the Big Kundt Tube, only one periodical cell has been represented, having the same external cross section as the 10×10mm section used for the measurements. The internal square cross section has been created maintaining an equivalent area as for the case of experimental measurements. A periodical structure composed of several cells to represent the complete 600×600mm sample area of the Big Kundt Tube has not been used, because the computational times to have a reasonable convergence would have been feasible with the available code.

Another important aspect of the model regards the boundary conditions. The boundary conditions in a Kundt Tube should ideally be of a sliding type, with no air gaps on the edges of the samples. However, in real experiments it is rather difficult to completely respect such conditions. The most important issue is to avoid air gaps; for this reason, teflon has been used for most of the experiments, when a small air gap was present, to close it. Acting this way, the sample is slightly compressed and the subsequent compression on the edges of the tube let suppose that the boundary conditions will not be of perfect sliding.

As a consequence, two different models have been constructed, to investigate the effect of boundary conditions at the edges of the sample, the first with a sliding condition and the second with a clamped condition. Moreover, to investigate the effect of materials elasticity, a third model has been calculated, where the poroelastic materials have been substituted by equivalent fluid materials with rigid frame, following the Johnson-

Champoux-Allard model. To summarize, the following are the three models used for the simulations:

- poroelastic materials, sliding boundary conditions;
- poroelastic materials, clamped boundary conditions;
- rigid frame materials, sliding boundary conditions.

For all the cases, when double porosity is concerned, air is represented as a fluid material.

Configuration	**External cross section**		**Internal cross section**		**Mesoporosity**	**Thickness**
	Shape	Dimension (mm)	Shape	Dimension (mm)	(-)	(mm)
A	square	$l = 40.76$	square	$l = 10$	0.060	45
B	square	$l = 40.76$	square	$l = 14$	0.118	45
C	square	$l = 40.76$	square	$l = 25$	0.376	45
D	square	$l = 40.76$	square	$l = 25.7$	0.397	45

Table 5.1: Dimensions of the model of figure 5.1, to represent the configurations of the Small Kundt Tube with equivalent areas and mesoporosities

Configuration	**External cross section**		**Internal cross section**		**Mesoporosity**	**Thickness**
	Shape	Dimension (mm)	Shape	Dimension (mm)	(-)	(mm)
A	square	$l = 88.62$	square	$l = 21$	0.056	45.5
B	square	$l = 88.62$	square	$l = 30$	0.115	45.5
C	square	$l = 88.62$	square	$l = 55.5$	0.392	45.5
D	square	$l = 88.62$	square	$l = 40.76$	0.212	45.5

Table 5.2: Dimensions of the model of figure 5.1, to represent the configurations of the Medium Kundt Tube with equivalent areas and mesoporosities

Number of cells	**External cross section**		**Internal cross section**		**Mesoporosity**	**Thickness**
	Shape	Dimension (mm)	Shape	Dimension (mm)	(-)	(mm)
1	square	$l = 100$	square	$l = 51.40$	0.264	90

Table 5.3: Dimensions of the model of figure 5.1, to represent the configurations of the Big Kundt Tube with equivalent areas and mesoporosities

5.2 Numerical results

The results are presented in Figures 5.2 to 5.9 for the configurations of the Small Kundt Tube, in Figures 5.10 to 5.17 for the configurations of the Medium Kundt Tube and in Figures 5.18 and 5.19 for the configurations of the Big Kundt Tube.

In the Small and Medium Kundt Tube, there is good agreement between experimental, analytical and numerical results. The fact that the curves obtained with the three different numerical models (poroelastic materials and sliding boundary conditions; poroelastic materials and clamped boundary conditions; rigid frame materials and sliding boundary conditions) are similar to each other and to the analytical curves indicate that the structural effect is not very important. The comparison is satisfactory both for the case of double porosity and of heterogeneous. From the numerical results obtained here, it is not possible to predict if the edge constraint of the experimental measurements can be considered more similar to a sliding or a clamped boundary condition. Some small differences in the elastic resonances are observed for different conditions, for example in Fig. 5.6 or 5.16, however there is not a clear relation between the experimental case and one of the assumed models.

In the Big Kundt Tube, the predictions obtained when poroelasticity is taken into account are not reliable. In fact, the resonances observed for both cases of sliding and clamped boundary conditions are not confirmed by the experimental results; at the same time, the analytical model and the numerical model in the case of rigid frame are in agreement with the experimental data. This behavior can be explained considering that the material is compressed more than in the cases of the Small or Medium Kundt Tubes: the elastic resonances are shifted out of the measured range of frequencies and the numerical poroelastic model based on elastic parameters measured on small samples is not reliable.

5.3 Remarks

FEM calculations have confirmed the agreement already observed previously between analytical and experimental data, showing in general a similar trend. The resonances measured experimentally have small effect on the general shapes of the absorption curves, therefore in the cases taken into account the assumption of rigid frame made for the

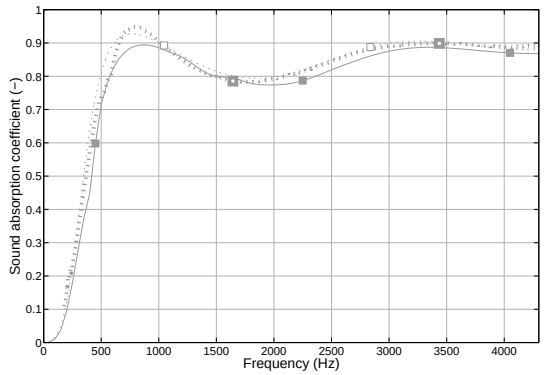

(a) Comparison between the experimental curve (⋯□⋯), the analytical curve (---□---) and the numerical curve obtained with the Biot model and sliding boundary conditions (—■—)

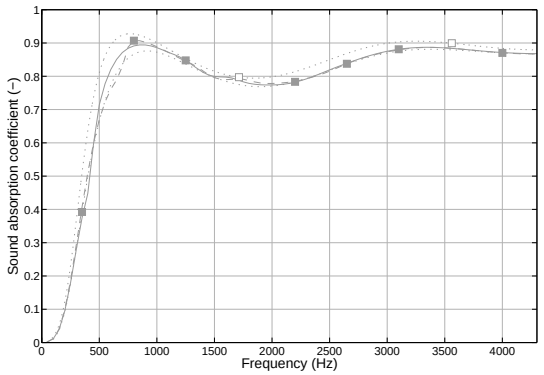

(b) Comparison between the analytical curve (---□---) and the numerical curves obtained with the Biot model and sliding boundary conditions (—■—), with the Biot model and clamped boundary conditions (--■--) and with the rigid frame model and sliding boundary conditions (---■---)

Figure 5.2: Small Kundt Tube, 45mm thick layer, *u*160 double porosity, FEM simulation for configuration A

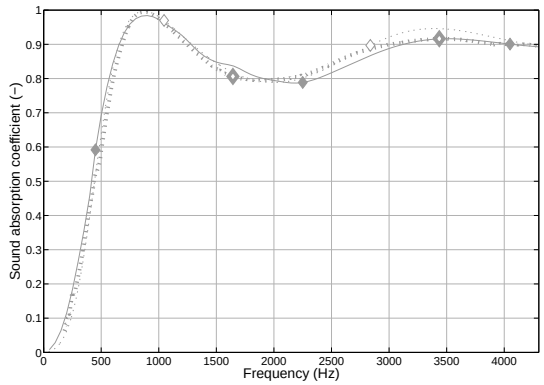

(a) Comparison between the experimental curve (⋯◇⋯), the analytical curve (---◇---) and the numerical curve obtained with the Biot model and sliding boundary conditions (—◆—)

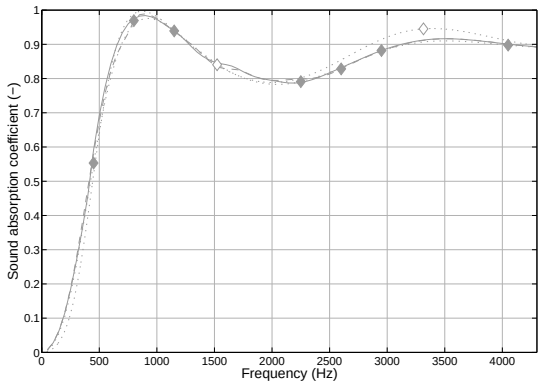

(b) Comparison between the analytical curve (---◇---) and the numerical curves obtained with the Biot model and sliding boundary conditions (—◆—), with the Biot model and clamped boundary conditions (--◆--) and with the rigid frame model and sliding boundary conditions (---◆---)

Figure 5.3: Small Kundt Tube, 45mm thick layer, *u*160 double porosity, FEM simulation for configuration B

analytical model is acceptable. With the described simplified numerical model, it is difficult to predict the elastic resonances in comparison to experimental measurements.

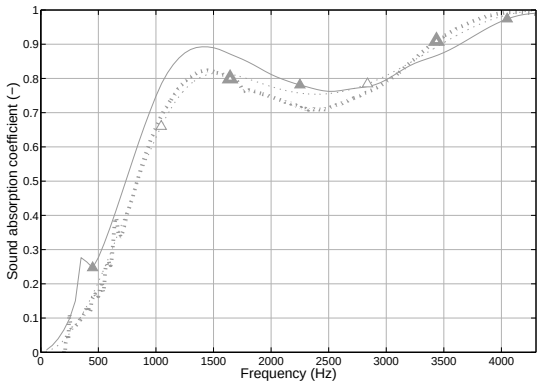

(a) Comparison between the experimental curve (⋯△⋯), the analytical curve (---△---) and the numerical curve obtained with the Biot model and sliding boundary conditions (—▲—)

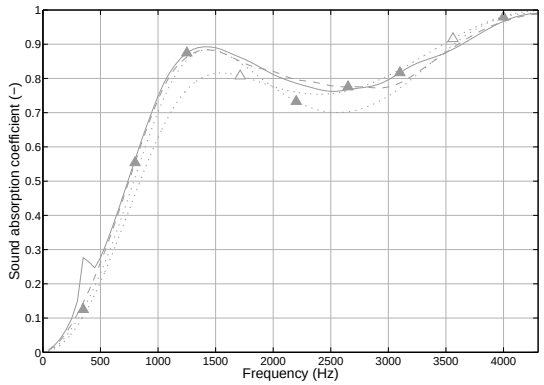

(b) Comparison between the analytical curve (---△---) and the numerical curves obtained with the Biot model and sliding boundary conditions (—▲—), with the Biot model and clamped boundary conditions (– –▲– –) and with the rigid frame model and sliding boundary conditions (---▲---)

Figure 5.4: Small Kundt Tube, 45mm thick layer, *u*160 double porosity, FEM simulation for configuration C

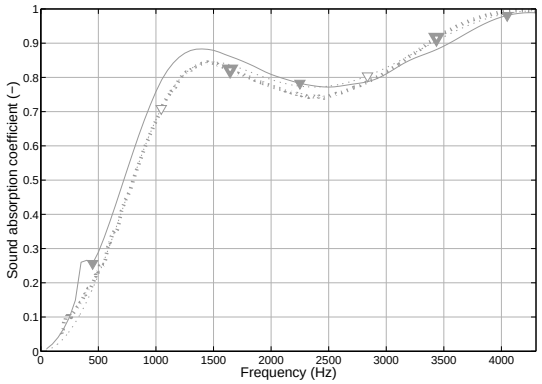

(a) Comparison between the experimental curve (⋯▽⋯), the analytical curve (---▽---) and the numerical curve obtained with the Biot model and sliding boundary conditions (—▼—)

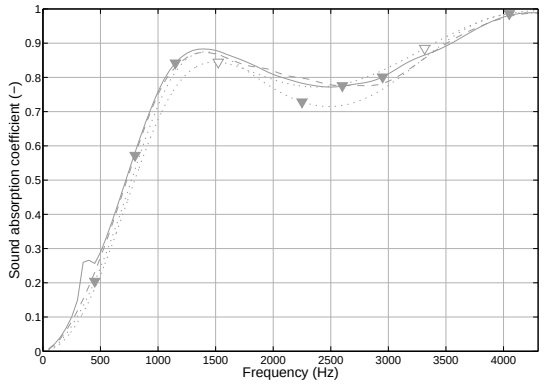

(b) Comparison between the analytical curve (---▽---) and the numerical curves obtained with the Biot model and sliding boundary conditions (—▼—), with the Biot model and clamped boundary conditions (– –▼– –) and with the rigid frame model and sliding boundary conditions (---▼---)

Figure 5.5: Small Kundt Tube, 45mm thick layer, *u*160 double porosity, FEM simulation for configuration D

Compared to FEM simulations, the analytical calculations are much faster. However, some restrictive hypotheses are fixed for the analytical model, in particular the rigid frame assumption, the periodical structure and the separation of scales. It is important,

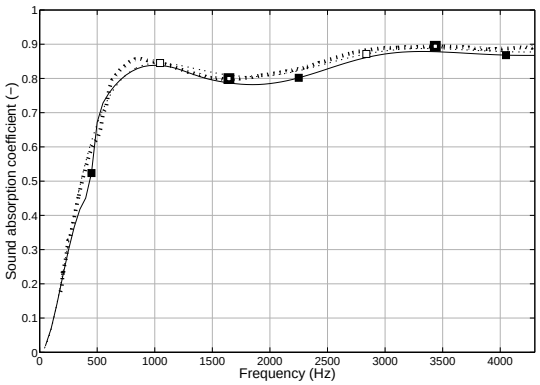

(a) Comparison between the experimental curve (▪▪▪□▪▪▪), the analytical curve (▪▪▪□▪▪▪) and the numerical curve obtained with the Biot model and sliding boundary conditions (—■—)

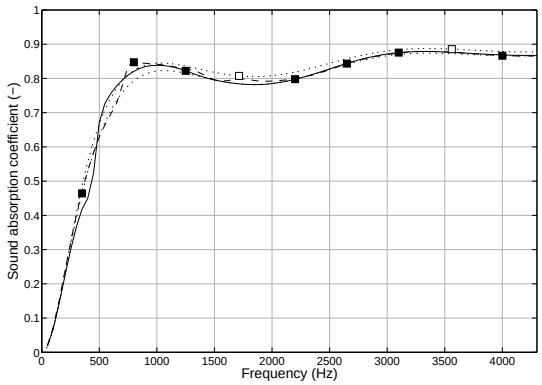

(b) Comparison between the analytical curve (▪▪▪□▪▪▪) and the numerical curves obtained with the Biot model and sliding boundary conditions (—■—), with the Biot model and clamped boundary conditions (– –■– –) and with the rigid frame model and sliding boundary conditions (▪▪▪■▪▪▪)

Figure 5.6: Small Kundt Tube, 45mm thick layer, heterogeneous *u*160 with *melamine* inclusions, FEM simulation for configuration A

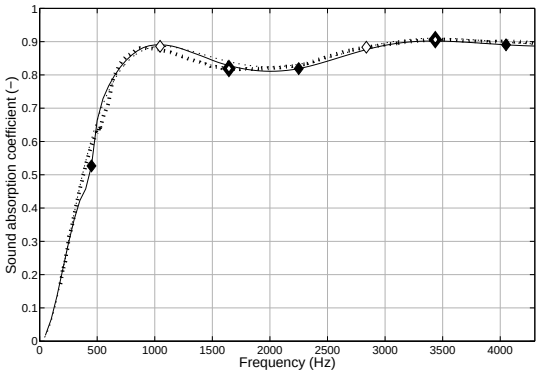

(a) Comparison between the experimental curve (▪▪▪◇▪▪▪), the analytical curve (▪▪▪◇▪▪▪) and the numerical curve obtained with the Biot model and sliding boundary conditions (—◆—)

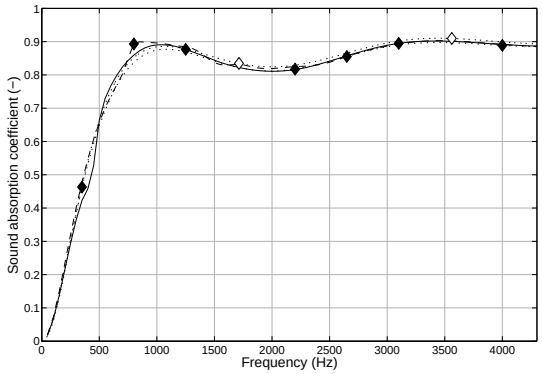

(b) Comparison between the analytical curve (▪▪▪◇▪▪▪) and the numerical curves obtained with the Biot model and sliding boundary conditions (—◆—), with the Biot model and clamped boundary conditions (– –◆– –) and with the rigid frame model and sliding boundary conditions (▪▪▪◆▪▪▪)

Figure 5.7: Small Kundt Tube, 45mm thick layer, heterogeneous *u*160 with *melamine* inclusions, FEM simulation for configuration B

in general, to verify that the pressure diffusion effects and the hypotheses about the permeability contrast.

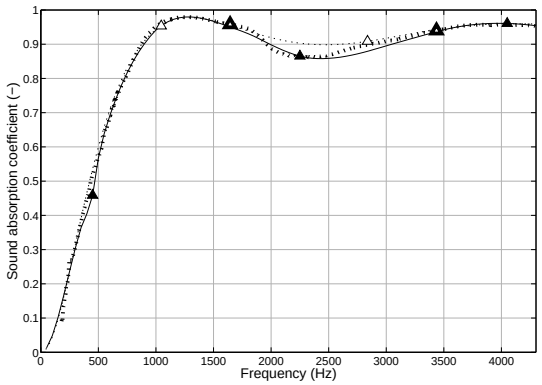

(a) Comparison between the experimental curve (▪▪△▪▪), the analytical curve (▪▪△▪▪) and the numerical curve obtained with the Biot model and sliding boundary conditions (—▲—)

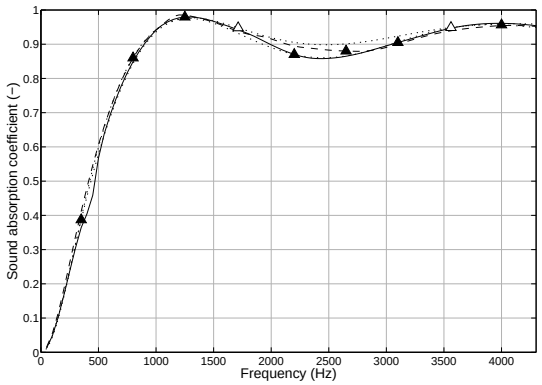

(b) Comparison between the analytical curve (▪▪△▪▪) and the numerical curves obtained with the Biot model and sliding boundary conditions (—▲—), with the Biot model and clamped boundary conditions (– –▲– –) and with the rigid frame model and sliding boundary conditions (▪▪▲▪▪)

Figure 5.8: Small Kundt Tube, 45mm thick layer, heterogeneous *u*160 with *melamine* inclusions, FEM simulation for configuration C

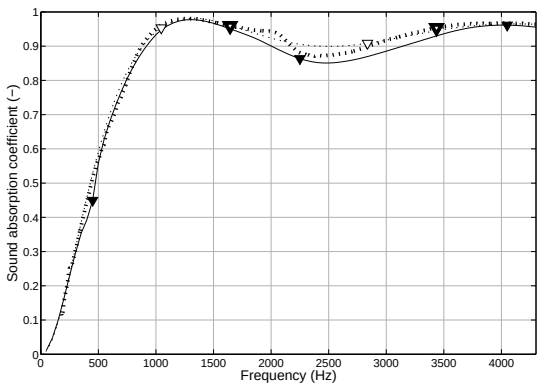

(a) Comparison between the experimental curve (▪▪▽▪▪), the analytical curve (▪▪▽▪▪) and the numerical curve obtained with the Biot model and sliding boundary conditions (—▼—)

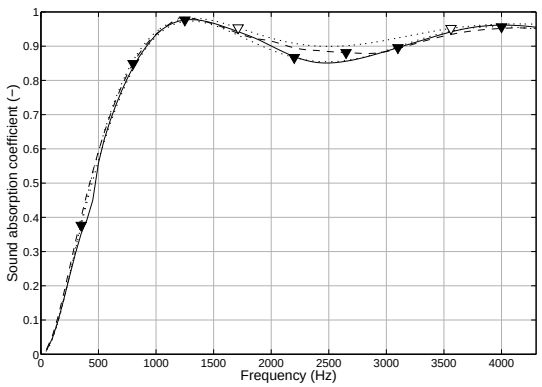

(b) Comparison between the analytical curve (▪▪▽▪▪) and the numerical curves obtained with the Biot model and sliding boundary conditions (—▼—), with the Biot model and clamped boundary conditions (– –▼– –) and with the rigid frame model and sliding boundary conditions (▪▪▼▪▪)

Figure 5.9: Small Kundt Tube, 45mm thick layer, heterogeneous *u*160 with *melamine* inclusions, FEM simulation for configuration D

On the other side, even if FEM calculations can reproduce the real structure in more precisely, there could be some limitations in the numerical model, for example in the geometry. The best practice is to obtain a satisfactory agreement between experimental,

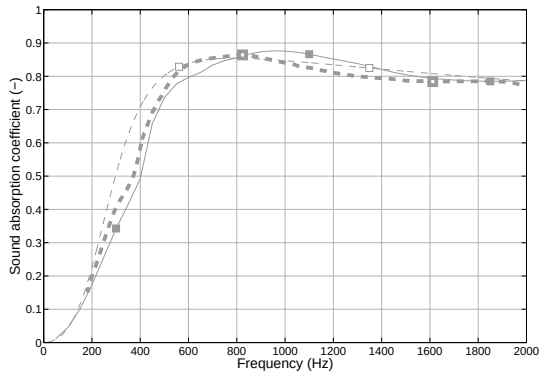

(a) Comparison between the experimental curve (–□–), the analytical curve (––□––) and the numerical curve obtained with the Biot model and sliding boundary conditions (—■—)

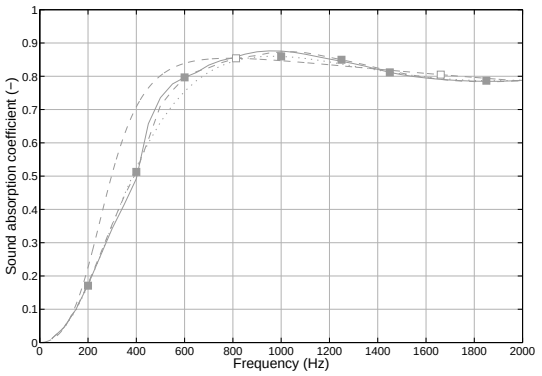

(b) Comparison between the analytical curve (––□––) and the numerical curves obtained with the Biot model and sliding boundary conditions (—■—), with the Biot model and clamped boundary conditions (––■––) and with the rigid frame model and sliding boundary conditions (----■----)

Figure 5.10: Medium Kundt Tube, 45.5mm thick layer, $u160$ double porosity, FEM simulation for configuration A

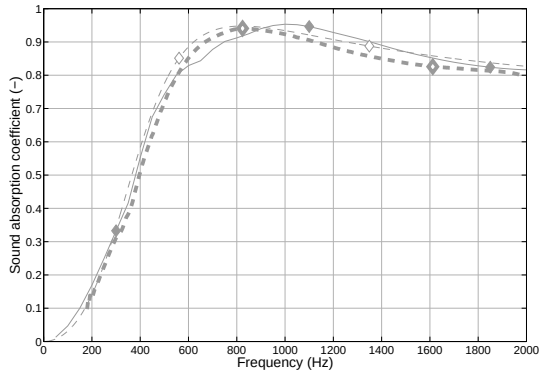

(a) Comparison between the experimental curve (–◇–), the analytical curve (––◇––) and the numerical curve obtained with the Biot model and sliding boundary conditions (—◆—)

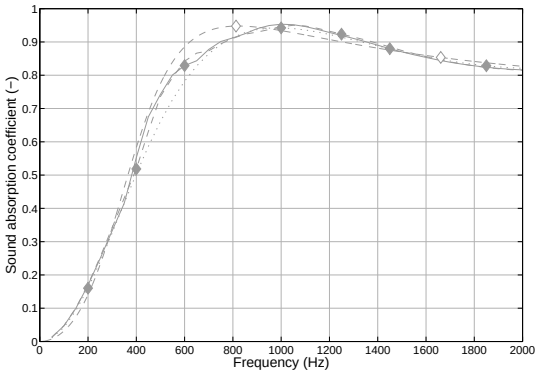

(b) Comparison between the analytical curve (––◇––) and the numerical curves obtained with the Biot model and sliding boundary conditions (—◆—), with the Biot model and clamped boundary conditions (––◆––) and with the rigid frame model and sliding boundary conditions (----◆----)

Figure 5.11: Medium Kundt Tube, 45.5mm thick layer, $u160$ double porosity, FEM simulation for configuration B

analytical and at least a representative FEM simulation taking into account eventual doubtful aspects (for example elastic effects). Then the analytical model can be used for prediction and for optimization, for example to find the best configuration of an

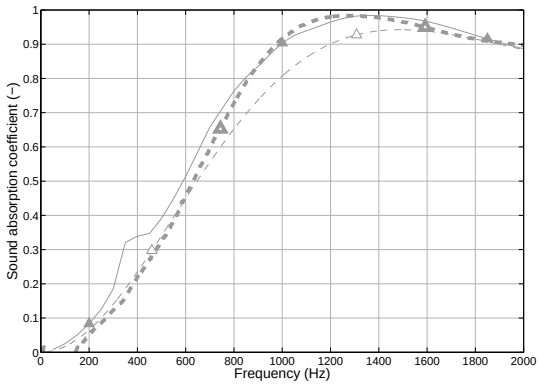

(a) Comparison between the experimental curve (--△--), the analytical curve (--△--) and the numerical curve obtained with the Biot model and sliding boundary conditions (—▲—)

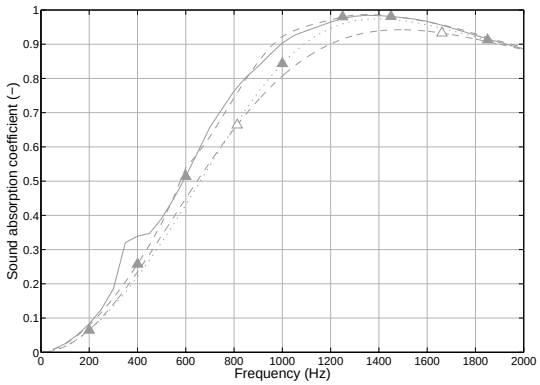

(b) Comparison between the analytical curve (--△--) and the numerical curves obtained with the Biot model and sliding boundary conditions (—▲—), with the Biot model and clamped boundary conditions (--▲--) and with the rigid frame model and sliding boundary conditions (---▲---)

Figure 5.12: Medium Kundt Tube, 45.5mm thick layer, *u*160 double porosity, FEM simulation for configuration C

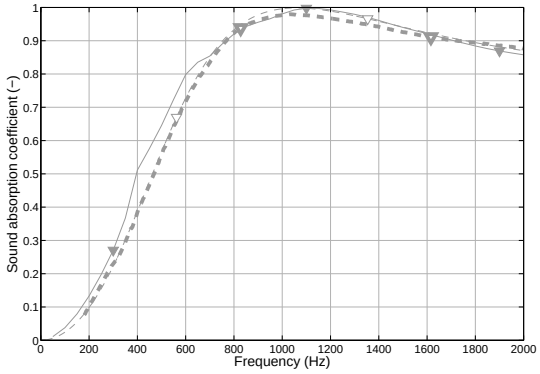

(a) Comparison between the experimental curve (--▽--), the analytical curve (--▽--) and the numerical curve obtained with the Biot model and sliding boundary conditions (—▼—)

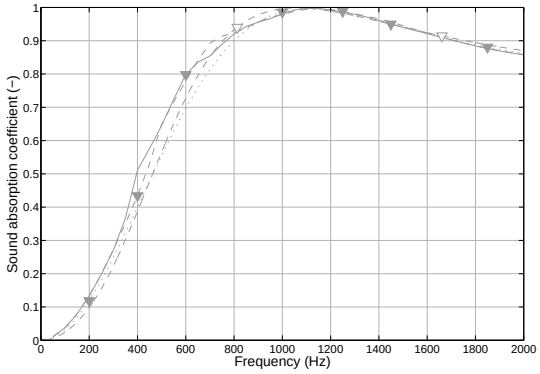

(b) Comparison between the analytical curve (--▽--) and the numerical curves obtained with the Biot model and sliding boundary conditions (—▼—), with the Biot model and clamped boundary conditions (--▼--) and with the rigid frame model and sliding boundary conditions (---▼---)

Figure 5.13: Medium Kundt Tube, 45.5mm thick layer, *u*160 double porosity, FEM simulation for configuration D

heterogeneous layer for a particular application. In the case of optimization, in fact, a huge number of calculations could be required and the use of numerical simulations would not be recommended for configurations involving a huge number of degrees of freedom.

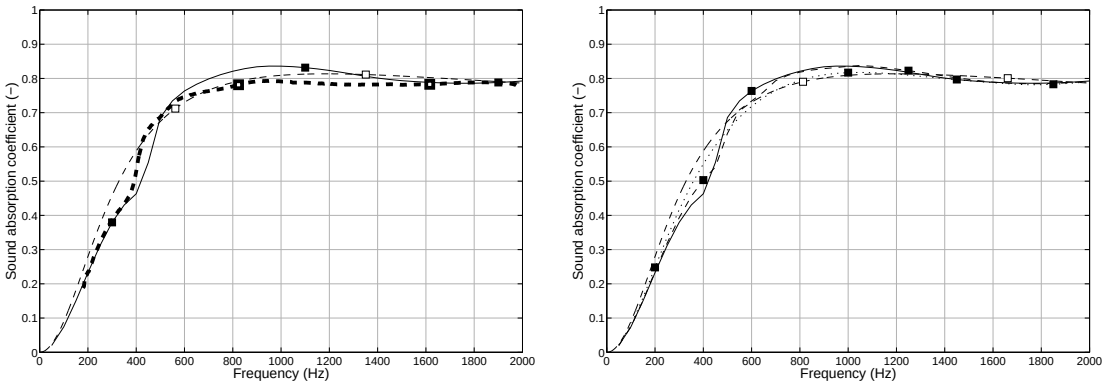

(a) Comparison between the experimental curve (–■–), the analytical curve (–□–) and the numerical curve obtained with the Biot model and sliding boundary conditions (—■—)

(b) Comparison between the analytical curve (–□–) and the numerical curves obtained with the Biot model and sliding boundary conditions (—■—), with the Biot model and clamped boundary conditions (–■–) and with the rigid frame model and sliding boundary conditions (---■---)

Figure 5.14: Medium Kundt Tube, 45.5mm thick layer, heterogeneous *u*160 with *melamine* inclusions, FEM simulation for configuration A

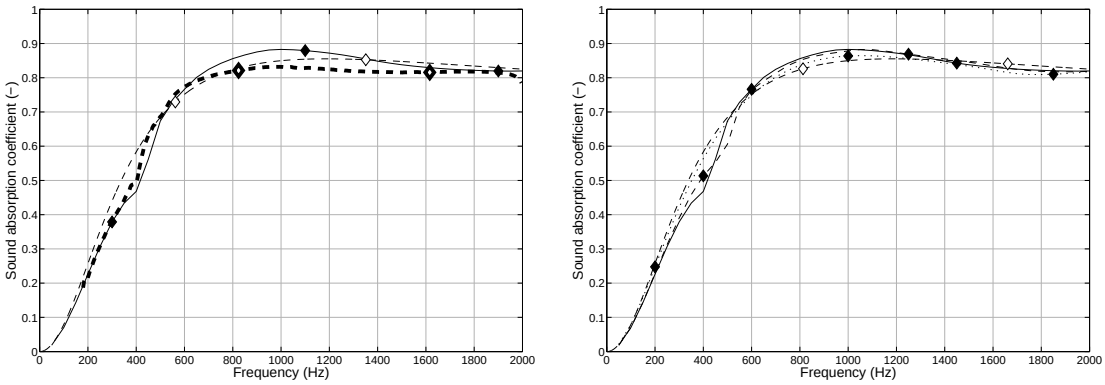

(a) Comparison between the experimental curve (–◇–), the analytical curve (–◇–) and the numerical curve obtained with the Biot model and sliding boundary conditions (—◆—)

(b) Comparison between the analytical curve (–◇–) and the numerical curves obtained with the Biot model and sliding boundary conditions (—◆—), with the Biot model and clamped boundary conditions (–◆–) and with the rigid frame model and sliding boundary conditions (---◆---)

Figure 5.15: Medium Kundt Tube, 45.5mm thick layer, heterogeneous *u*160 with *melamine* inclusions, FEM simulation for configuration B

However, in case of complicated geometries (not planar layers, or finite dimensions and irregular shapes) FEM calculations should be used.

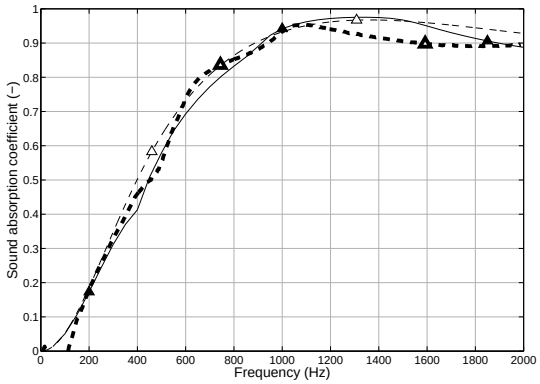

(a) Comparison between the experimental curve (--△--), the analytical curve (--△--) and the numerical curve obtained with the Biot model and sliding boundary conditions (—▲—)

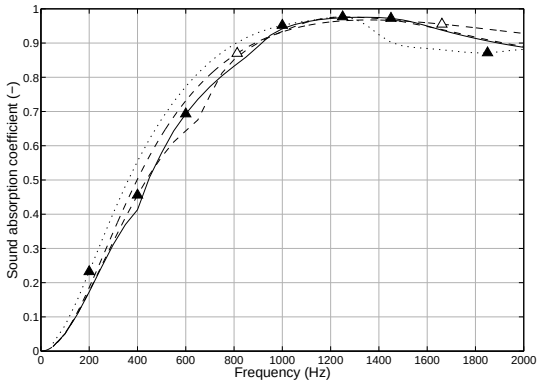

(b) Comparison between the analytical curve (--△--) and the numerical curves obtained with the Biot model and sliding boundary conditions (—▲—), with the Biot model and clamped boundary conditions (--▲--) and with the rigid frame model and sliding boundary conditions (---▲---)

Figure 5.16: Medium Kundt Tube, 45.5mm thick layer, heterogeneous *u*160 with *melamine* inclusions, FEM simulation for configuration C

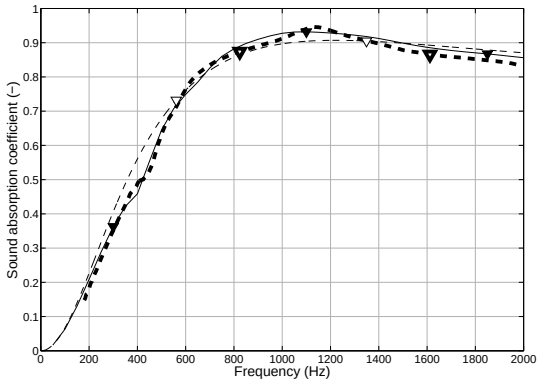

(a) Comparison between the experimental curve (--▽--), the analytical curve (--▽--) and the numerical curve obtained with the Biot model and sliding boundary conditions (—▼—)

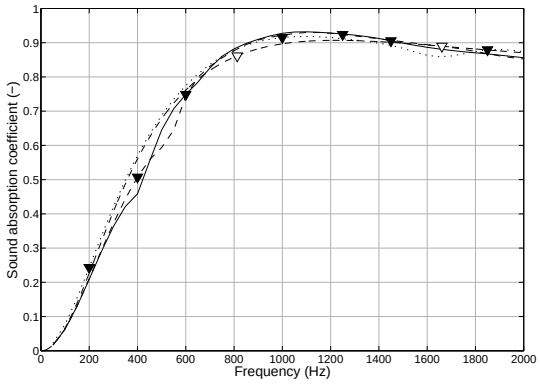

(b) Comparison between the analytical curve (--▽--) and the numerical curves obtained with the Biot model and sliding boundary conditions (—▼—), with the Biot model and clamped boundary conditions (--▼--) and with the rigid frame model and sliding boundary conditions (---▼---)

Figure 5.17: Medium Kundt Tube, 45.5mm thick layer, heterogeneous *u*160 with *melamine* inclusions, FEM simulation for configuration D

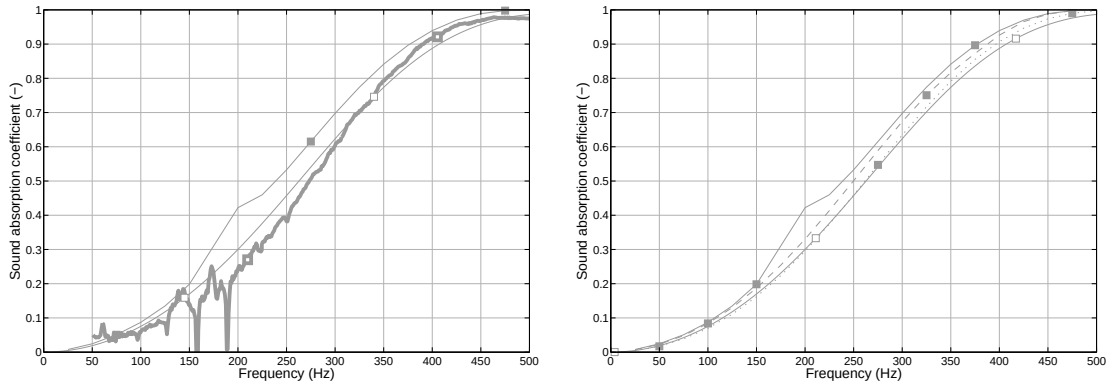

(a) Comparison between the experimental curve (—□—), the analytical curve (----□----) and the numerical curve obtained with the Biot model and sliding boundary conditions (—■—)

(b) Comparison between the analytical curve (----□----) and the numerical curves obtained with the Biot model and sliding boundary conditions (—■—), with the Biot model and clamped boundary conditions (--■--) and with the rigid frame model and sliding boundary conditions (----■----)

Figure 5.18: Big Kundt Tube, 90mm thick layer, *u*160 double porosity, FEM simulation

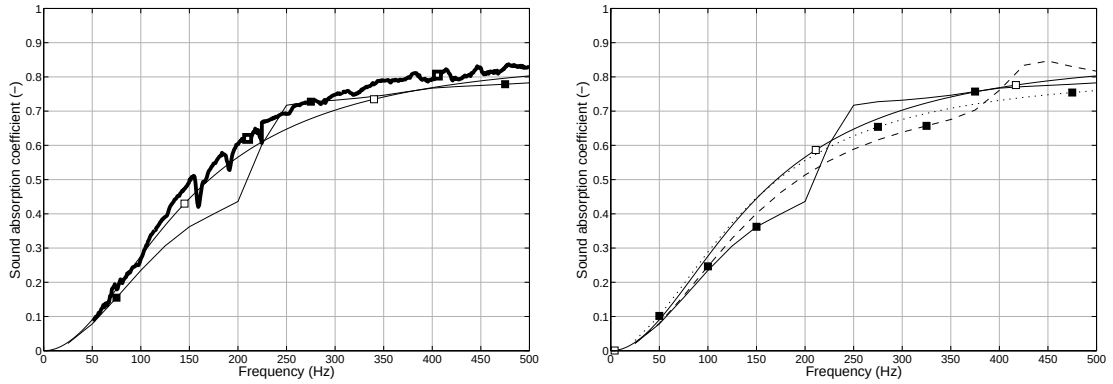

(a) Comparison between the experimental curve (—□—), the analytical curve (----□----) and the numerical curve obtained with the Biot model and sliding boundary conditions (—■—)

(b) Comparison between the analytical curve (----□----) and the numerical curves obtained with the Biot model and sliding boundary conditions (—■—), with the Biot model and clamped boundary conditions (--■--) and with the rigid frame model and sliding boundary conditions (----■----)

Figure 5.19: Big Kundt Tube, 90mm thick layer, heterogeneous *u*160 with *melamine* inclusions, FEM simulation

6 Sound transmission of porous materials with inclusions

The results obtained in Chapter 4 are here applied and extended to the case of transmission of sound. At first, the analytical model for heterogeneous materials is extended to the case of transmission. From a theoretical point of view, the calculations performed as from Section 4.2 that lead to an equivalent dynamical density ρ_h and bulk modulus K_h must be done exactly in the same way as described previously. The same hypotheses (periodicity, rigid frame) are still valid and the same theory applies, both for a double porosity layer and for an heterogeneous layer with inclusions, up to the definition of the equivalent quantities ρ_h and K_h. The main difference regards the calculation of the multilayer configuration. In fact, in this case a transfer matrix must be introduced and the transfer matrix method (TMM) must be applied. In particular, for the case of a double porosity or heterogeneous layer backed by an elastic solid, the transfer matrix for the solid must be defined and the required interface conditions must be set. Also in the following lines, like for the case of absorption, normal incidence of the acoustic wave is assumed.

Secondly, experimental results obtained in the Medium Kundt Tube with a four microphone measurement are presented. Then, analytical model is validated against experimental measurements and the comparison is commented.

6.1 Analytical model

Let us consider a system where two domains of an exterior fluid are separated by a set of n layers (for example porous or solid layers), like in Fig. 6.1. The system is supposed infinite in the in-plane directions. We are interested in the transmission of acoustic waves between the two fluid domains. The exterior fluid (air, for example) can be described through pressure p and particle normal velocity v.

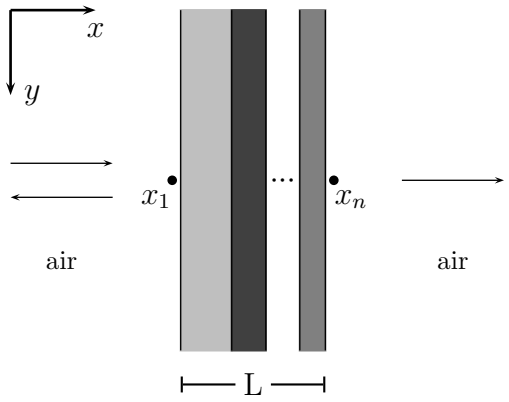

Figure 6.1: General configuration of a multilayer, in the case of a normal incident acoustic wave

6.1.1 Transmission Loss with the matrix method

At incidence x_1^a, the system is excited by a plane wave, at normal incidence. At incidence side, also a reflected wave is present. At transmission side x_n^a, a wave propagates into the infinite fluid and no reflected wave is present. This condition is reproduced in practice by an anechoic termination at the transmission side.
At incidence side, the fluid velocity potential can be written as:

$$\psi|_{x\leq x_1^a} = \left(Ae^{-jk_a x} + Be^{jk_a x}\right) e^{j\omega t} \tag{6.1}$$

where A and B are constants related to the forward and backward traveling waves and k_a is the wave number of the exterior fluid (air). The expressions for pressure p and particle normal velocity v at the incidence side can be immediately derived from the following relations valid for the fluid:

$$p = \rho_a \frac{\partial \psi}{\partial t} \tag{6.2}$$

$$\boldsymbol{v} = -\nabla\psi \tag{6.3}$$

obtaining

$$p|_{x\leq x_1^a} = j\omega\rho_a \left(Ae^{-jk_a x} + Be^{jk_a x}\right) e^{j\omega t} \tag{6.4}$$

$$v|_{x\leq x_1^a} = jk_a \left(Ae^{-jk_a x} - Be^{jk_a x}\right) e^{j\omega t}. \tag{6.5}$$

At transmission side, since no reflected wave is present, the fluid velocity potential can be written as:

$$\psi|_{x\geq x_n^a} = Ce^{-jk_a x}e^{j\omega t} \tag{6.6}$$

where C is a constant related to the transmitted wave and analogously pressure p and particle normal velocity v are derived:

$$p|_{x\geq x_n^a} = j\omega\rho_a Ce^{-jk_a x}e^{j\omega t} \tag{6.7}$$

$$v|_{x\geq x_n^a} = jk_a Ce^{-jk_a x}e^{j\omega t}. \tag{6.8}$$

If we make use of the matrix formulation, the global transfer matrix $[T]$ relates the variables at $x = x_1^a$ and at $x = x_n^a$ in the exterior fluid through:

$$\begin{bmatrix} p \\ v \end{bmatrix}_{x\leq x_1^a} = \begin{bmatrix} T_{11} & T_{12} \\ T_{21} & T_{22} \end{bmatrix} \begin{bmatrix} p \\ v \end{bmatrix}_{x\geq x_n^a}. \tag{6.9}$$

From the reciprocal conditions [1, 50] follows:

$$T_{11} = T_{12} \tag{6.10}$$

$$T_{11}T_{22} - T_{12}T_{21} = 0 \tag{6.11}$$

and, in particular, follows that the system is characterized by a unique transmission coefficient T_c and a unique reflection coefficient R_c at both sides of the layer. From equations 6.1 and 6.6 and the derived expressions for pressure and velocity, it is clear that:

$$R_c = \frac{B}{A} \qquad T_c = \frac{C}{A} \tag{6.12}$$

The transmission coefficient can be calculated starting from the transfer matrix coefficients:

$$T_c = \frac{2e^{jk_a L}}{T_{11} + T_{12}/(\rho_a c_a) + T_{12}(\rho_a c_a) + T_{22}} \tag{6.13}$$

where $Z_a = \rho_a c_a$ is the characteristic impedance of the exterior fluid (air) and L is the total thickness of the interstitial layers.
From equations 6.4, 6.5 and 6.7, 6.8 other useful relations are derived, that will be

recalled later:

$$\frac{p|_{x_1^a}}{p|_{x_n^a}} = \frac{1+R_c}{T_c} e^{jk_aL} \tag{6.14}$$

$$\frac{v|_{x_1^a}}{v|_{x_n^a}} = \frac{1-R_c}{T_c} e^{jk_aL}. \tag{6.15}$$

At the end, the transmission loss can be calculated as:

$$TL = 20 \log \left(\frac{1}{|T_c|} \right) \tag{6.16}$$

and is usually considered a measure of the transmission properties of the system under study. Therefore, it is required to determine the components of the transfer matrix of the system to calculate the transmission loss, or directly the transmission coefficient. When different layers composed of different materials are involved, interface conditions between one layer and the following are to be taken into account. Interface matrices link the variables describing the materials at different sides of the interface, by exploiting the interface conditions [1, 12].

Single layer of heterogeneous porous material with inclusions

In the case the material sample is placed alone in the Kundt tube, we can refer to a single layer configuration (Fig. 6.2(a)). Let us consider an heterogeneous material with inclusions, in the hypothesis of rigid frame, hence represented by an equivalent fluid and characterized by its characteristic impedance Z_h and its wave number k_h, that can be calculated as from the analytical model of Section 4.2. In this case the transfer matrix relates pressure and particle normal velocity at the two sides of the layer.

Pressure and velocity in the heterogeneous material can be expressed, as previously done for the case of air, considering a forward and a backward traveling wave and starting from the expression of the velocity potential:

$$\psi = \left(Ae^{-jk_hx} + Be^{jk_hx} \right) e^{j\omega t} \tag{6.17}$$

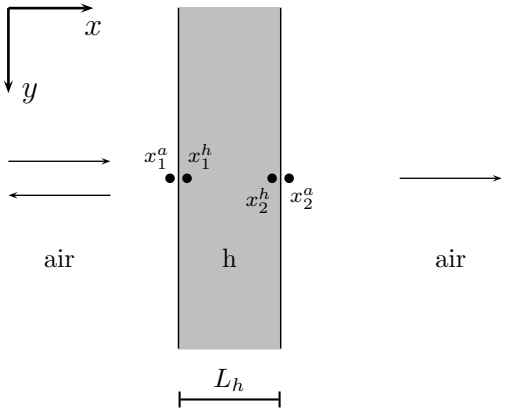

(a) Configuration with a single layer of rigid porous material (p)

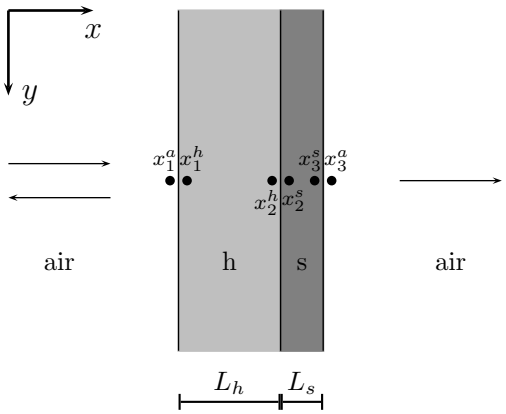

(b) Configuration with a layer of rigid porous material (p) and a layer of elastic solid (s)

Figure 6.2: Configurations for the case of transmission

obtaining

$$p = j\omega\rho_h(Ae^{-jk_hx} + Be^{jk_hx})e^{j\omega t} \tag{6.18}$$

$$v = jk_h(Ae^{-jk_hx} - Be^{jk_hx})e^{j\omega t} \tag{6.19}$$

where A and B are constants (different from the ones in Eq. 6.1) and ρ_h is the dynamic density of the heterogeneous material. These expressions are derived considering a normal incident wave. Arbitrarily fixing the origin of axes and writing equations 6.18 and 6.19 for $x_1^h = -L_h$ (being L_h the thickness of the heterogeneous layer) and $x_2^h = 0$ one

obtains:

$$\begin{bmatrix} p \\ v \end{bmatrix}_{x=-L_h} = j\omega\rho_h \begin{bmatrix} e^{jk_hL_h} & e^{-jk_hL_h} \\ \frac{1}{Z_h}e^{jk_hL_h} & \frac{1}{Z_h}e^{-jk_hL_h} \end{bmatrix} \begin{bmatrix} A \\ B \end{bmatrix} e^{j\omega t} \tag{6.20}$$

and

$$\begin{bmatrix} p \\ v \end{bmatrix}_{x=0} = j\omega\rho_h \begin{bmatrix} 1 & 1 \\ \frac{1}{Z_h} & -\frac{1}{Z_h} \end{bmatrix} \begin{bmatrix} A \\ B \end{bmatrix} e^{j\omega t} \tag{6.21}$$

where $Z_h = \frac{\omega\rho_h}{k_h} = \rho_h c_h$ is the characteristic impedance of the heterogeneous material, being c_h its wave speed.

Calculating $\left[\begin{smallmatrix} A \\ B \end{smallmatrix}\right]$ from Eq. 6.21 and then using Eq. 6.20 one obtains:

$$\begin{bmatrix} p \\ v \end{bmatrix}_{x=-L_h} = \begin{bmatrix} e^{jk_hL_h} & e^{-jk_hL_h} \\ \frac{1}{Z_h}e^{jk_hL_h} & \frac{1}{Z_h}e^{-jk_hL_h} \end{bmatrix} \begin{bmatrix} 1 & 1 \\ \frac{1}{Z_h} & -\frac{1}{Z_h} \end{bmatrix}^{-1} \begin{bmatrix} p \\ v \end{bmatrix}_{x=0} \tag{6.22}$$

and therefore the expression for the transfer matrix:

$$\left[T^h\right] = \begin{bmatrix} \cos k_hL_h & jZ_h \sin k_hL_h \\ \frac{j}{Z_h}\sin k_hL_h & \cos k_hL_h \end{bmatrix} \tag{6.23}$$

as function of k_h and Z_h, that can be obtained from the analytical model for heterogeneous materials with inclusions.

In this case the interface conditions are very simple and require the pressures and the particle normal velocities in the exterior air and in the rigid porous material to be identical at both ends of the porous layer:

$$\begin{bmatrix} p \\ v \end{bmatrix}_{x_1^a} = \begin{bmatrix} p \\ v \end{bmatrix}_{x_1^h} \quad \text{and} \quad \begin{bmatrix} p \\ v \end{bmatrix}_{x_2^h} = \begin{bmatrix} p \\ v \end{bmatrix}_{x_2^h}. \tag{6.24}$$

Therefore, considering also equations 6.9 and 6.23, the global transfer matrix can be calculated for the specific case as:

$$\left[T\right] = \left[T^h\right]. \tag{6.25}$$

Inserting the components of the matrix $[T^p]$ into Eq. 6.13, one obtains:

$$T_c = \frac{2e^{jk_aL_h}}{2\cos k_hL_h + j\sin k_hL_h\left(\frac{Z_h}{Z_a} + \frac{Z_a}{Z_h}\right)} \tag{6.26}$$

being in this case $L = L_h$.

Layer of rigid porous material backed by a solid elastic layer

In this case (depicted in Fig. 6.2(b)), a solid elastic layer is placed on the back of the heterogeneous layer depicted in Fig. 6.2(a), creating in this way a multilayer configuration. Following the transfer matrix method [1], the following quantities must be calculated:

- the transfer matrix of the rigid porous layer $\left[T^h\right]$;
- the transfer matrix of the elastic solid layer $[T^s]$

and the following relations must be considered:

- the interface conditions between air and the heterogeneous material at x_1;
- the interface conditions between the heterogeneous material and the elastic solid layer at x_2;
- the interface conditions between the elastic solid layer and air at x_3.

Transfer matrix for the elastic solid. The transfer matrix for the fluid (here equivalent fluid) has been derived in Section 6.1.1 (Eq. 6.23). The derivation of the transfer matrix for the solid in the case of a generic angle of incidence is found in [20]. An elastic solid layer as in Fig. 6.2(b) is described by four variables: the normal σ_{xx} and tangential σ_{xy} stresses and the velocities v_x and v_y in the x and y directions. Normal incidence is assumed here. As in the case of a fluid previously described, a velocity potential can be written as function of the traveling waves. In this case two waves propagate in the solid, a longitudinal and a transverse wave. In a generic 3D case, two potentials exist, such that:

$$\boldsymbol{v} = \nabla\psi_l + \nabla \times \boldsymbol{\psi}_t \tag{6.27}$$

For the generic case of a 2D semi-infinite layer, the two scalar potentials ψ_l (for the longitudinal wave) and ψ_t (for the transverse shear wave) are such that:

$$v_x = \frac{\partial \psi_l}{\partial x} + \frac{\partial \psi_t}{\partial y} \tag{6.28}$$

$$v_y = \frac{\partial \psi_l}{\partial y} - \frac{\partial \psi_t}{\partial x}; \tag{6.29}$$

these potentials satisfy the following wave equations:

$$\nabla^2 \psi_l + k_l^2 \psi_l = 0 \tag{6.30}$$

$$\nabla^2 \psi_t + k_t^2 \psi_t = 0 \tag{6.31}$$

where

$$k_l = \frac{\omega}{\sqrt{\frac{2\lambda_2+\lambda 1}{\rho_s}}} \qquad \text{and} \qquad k_t = \frac{\omega}{\sqrt{\frac{\lambda_2}{\rho_s}}} \tag{6.32}$$

are respectively the longitudinal and transverse wave numbers. Here ρ_s is the solid density and λ_1 the first and λ_2 the second Lamé constant, for which the following relations hold as functions of the Young modulus E and the Poisson's ratio ν:

$$\lambda_1 = \frac{\nu E}{(1+\nu)(1-2\nu)} \qquad \lambda_2 = N = \frac{E}{2(1+\nu)}. \tag{6.33}$$

In this case, considering the forward and backward traveling waves in the solid elastic layer and assuming normal incidence, the potentials are written:

$$\psi_l = (Ae^{-jk_l x} + Be^{jk_l x})e^{j\omega t} \tag{6.34}$$

$$\psi_t = (Ce^{-jk_t x} + De^{jk_t x})e^{j\omega t}. \tag{6.35}$$

From equations 6.28 and 6.29 one obtains:

$$v_x = -jk_l(Ae^{-jk_l x} - Be^{jk_l x})e^{j\omega t} \tag{6.36}$$

$$v_y = jk_t(Ce^{-jk_t x} - De^{jk_t x})e^{j\omega t}. \tag{6.37}$$

Similar equations are determined for the stresses. In 2D, the general stress-strain relations reduce to:

$$\begin{bmatrix} \sigma_{xx} \\ \sigma_{yy} \\ \sigma_{xy} \end{bmatrix} = \begin{bmatrix} 2\lambda_2 + \lambda_1 & \lambda_1 & 0 \\ \lambda_1 & 2\lambda_2 + \lambda_1 & 0 \\ 0 & 0 & \lambda_2 \end{bmatrix} \begin{bmatrix} e_{xx} \\ e_{yy} \\ e_{xy} \end{bmatrix}; \tag{6.38}$$

considering that $\boldsymbol{u} = \frac{\boldsymbol{v}}{j\omega}$ and using equations 6.36 and 6.37, the strains are calculated:

$$e_{xx} = \frac{jk_l^2}{\omega}(Ae^{-jk_l x} + Be^{jk_l x})e^{j\omega t} \tag{6.39}$$

$$e_{yy} = 0 \tag{6.40}$$

$$e_{xy} = -\frac{jk_t^2}{\omega}(Ce^{-jk_t x} + De^{jk_t x})e^{j\omega t} \tag{6.41}$$

and the stresses using equation 6.38:

$$\sigma_{xx} = j\omega\rho_s(Ae^{-jk_l x} + Be^{jk_l x})e^{j\omega t} \tag{6.42}$$

$$\sigma_{xy} = -j\omega\rho_s(Ce^{-jk_t x} + De^{jk_t x})e^{j\omega t}. \tag{6.43}$$

Using the Euler equations, expressions 6.42, 6.43 for the stresses and 6.36, 6.37 for the velocities can be written in a matrix fashion. In particular, the variables are expressed as functions of the quantities $A + B$, $A - B$, $C + D$ and $C - D$:

$$\begin{bmatrix} \sigma_{xx} \\ \sigma_{xy} \\ v_x \\ v_y \end{bmatrix} = \begin{bmatrix} j\omega\rho_s \cos k_l x & \omega\rho_s \sin k_l x & 0 & 0 \\ 0 & 0 & -j\omega\rho_s \cos k_t x & -\omega\rho_s \sin k_t x \\ jk_l \sin k_l x & -jk_l \cos k_l x & 0 & 0 \\ 0 & 0 & -jk_t \sin k_t x & jk_t \cos k_t x \end{bmatrix} \begin{bmatrix} A + B \\ A - B \\ C + D \\ C - D \end{bmatrix} \tag{6.44}$$

that can be directly applied to determine the transfer matrix for the elastic solid. In fact, as for the case of a fluid, the equation 6.44 is satisfied at the two sides of the solid

layer $x_2^s = 0$ and $x_3^s = L_s$ (having arbitrarily fixed the origin of the x-axis):

$$\begin{bmatrix} \sigma_{xx} \\ \sigma_{xy} \\ v_x \\ v_y \end{bmatrix}_{x=0} = \begin{bmatrix} j\omega\rho_s & 0 & 0 & 0 \\ 0 & 0 & -j\omega\rho_s & 0 \\ 0 & -jk_l & 0 & 0 \\ 0 & 0 & 0 & jk_t \end{bmatrix} \begin{bmatrix} A+B \\ A-B \\ C+D \\ C-D \end{bmatrix} \tag{6.45}$$

and

$$\begin{bmatrix} \sigma_{xx} \\ \sigma_{xy} \\ v_x \\ v_y \end{bmatrix}_{x=L_s} = \begin{bmatrix} j\omega\rho_s \cos k_l L_s & \omega\rho_s \sin k_l L_s & 0 & 0 \\ 0 & 0 & -j\omega\rho_s \cos k_t L_s & -\omega\rho_s \sin k_t L_s \\ jk_l \sin k_l L_s & -jk_l \cos k_l L_s & 0 & 0 \\ 0 & 0 & -jk_t \sin k_t L_s & jk_t \cos k_t L_s \end{bmatrix} \begin{bmatrix} A+B \\ A-B \\ C+D \\ C-D \end{bmatrix} \tag{6.46}$$

and finally, remembering that

$$\begin{bmatrix} \sigma_{xx} \\ \sigma_{xy} \\ v_x \\ v_y \end{bmatrix}_{x=0} = \left[T^s\right] \begin{bmatrix} \sigma_{xx} \\ \sigma_{xy} \\ v_x \\ v_y \end{bmatrix}_{x=L_s} \tag{6.47}$$

the transfer matrix for the elastic solid layer is calculated:

$$\left[T^s\right] = \begin{bmatrix} j\omega\rho_s & 0 & 0 & 0 \\ 0 & 0 & -j\omega\rho_s & 0 \\ 0 & -jk_l & 0 & 0 \\ 0 & 0 & 0 & jk_t \end{bmatrix} \begin{bmatrix} j\omega\rho_s \cos k_l L_s & \omega\rho_s \sin k_l L_s & 0 & 0 \\ 0 & 0 & -j\omega\rho_s \cos k_t L_s & -\omega\rho_s \sin k_t L_s \\ jk_l \sin k_l L_s & -jk_l \cos k_l L_s & 0 & 0 \\ 0 & 0 & -jk_t \sin k_t L_s & jk_t \cos k_t L_s \end{bmatrix}^{-1}. \tag{6.48}$$

Interface conditions. In the case under study (Fig. 6.2(b)), two kinds of interface conditions are involved: fluid-fluid and fluid-solid interfaces. In the case two fluids are in contact, as described in Section 6.1.1, pressure and particle normal velocity for the two fluid coincide at the interface section. In the case a fluid and a solid are in contact, the following conditions are required:

$$-p^f = \sigma^s_{xx} \tag{6.49}$$

$$v^f_x = v^s_x \tag{6.50}$$

$$0 = \sigma_{xy} \tag{6.51}$$

Referring to the interface at x_1, equations 6.49 can be written in matrix form:

$$\begin{bmatrix} 1 & 0 \\ 0 & 1 \\ 0 & 0 \end{bmatrix} \begin{bmatrix} p \\ v \end{bmatrix}_{x_2^h} + \begin{bmatrix} 1 & 0 & 0 & 0 \\ 0 & 0 & -1 & 0 \\ 0 & 1 & 0 & 0 \end{bmatrix} \begin{bmatrix} \sigma_{xx} \\ \sigma_{xy} \\ v_x \\ v_y \end{bmatrix}_{x_2^s} = \begin{bmatrix} 0 \\ 0 \\ 0 \end{bmatrix}. \tag{6.52}$$

Applying equation 6.52 to interfaces at x_2 and at x_3, the following are derived:

$$\begin{bmatrix} I_{h,s} \end{bmatrix} \begin{bmatrix} p \\ v \end{bmatrix}_{x_2^h} + \begin{bmatrix} J_{h,s} \end{bmatrix} \begin{bmatrix} \sigma_{xx} \\ \sigma_{xy} \\ v_x \\ v_y \end{bmatrix}_{x_2^s} = \begin{bmatrix} 0 \end{bmatrix} \tag{6.53}$$

$$\begin{bmatrix} I_{s,a} \end{bmatrix} \begin{bmatrix} \sigma_{xx} \\ \sigma_{xy} \\ v_x \\ v_y \end{bmatrix}_{x_3^s} + \begin{bmatrix} J_{s,a} \end{bmatrix} \begin{bmatrix} p \\ v \end{bmatrix}_{x_3^a} = \begin{bmatrix} 0 \end{bmatrix} \tag{6.54}$$

where

$$\begin{bmatrix} I_{h,s} \end{bmatrix} = \begin{bmatrix} J_{s,a} \end{bmatrix} = \begin{bmatrix} 1 & 0 \\ 0 & 1 \\ 0 & 0 \end{bmatrix} \tag{6.55}$$

and

$$\left[I_{s,a}\right] = \left[J_{h,s}\right] = \begin{bmatrix} 1 & 0 & 0 & 0 \\ 0 & 0 & -1 & 0 \\ 0 & 1 & 0 & 0 \end{bmatrix}. \tag{6.56}$$

Transmission coefficient calculation with the TMM. Using all the interface conditions and the transfer matrices, a linear system of equations can be built, the unknowns being the variables of each layer at both sides. However, in general there is a difference of 2 between the number of unknowns and the number of equations. Two additional conditions must be added to have a solution for the system: the boundary conditions at the edges of the layer. In this particular case, due to the simplicity of some interface conditions, the complete system can be slightly reduced. In fact, considering that

$$\begin{bmatrix} p \\ x \end{bmatrix}_{x_1^a} = \begin{bmatrix} p \\ x \end{bmatrix}_{x_1^h} = \left[T^h\right] \begin{bmatrix} p \\ x \end{bmatrix}_{x_2^h} \tag{6.57}$$

and that

$$\begin{bmatrix} \sigma_{xx} \\ \sigma_{xy} \\ v_x \\ v_y \end{bmatrix}_{x_2^s} = \left[T^s\right] \begin{bmatrix} \sigma_{xx} \\ \sigma_{xy} \\ v_x \\ v_y \end{bmatrix}_{x_3^s} \tag{6.58}$$

equation 6.53 can be rewritten as:

$$\left[I_{h,s}\right] \left[T^h\right]^{-1} \begin{bmatrix} p \\ v \end{bmatrix}_{x_2^h} + \left[J_{h,s}\right] \left[T^s\right] \begin{bmatrix} \sigma_{xx} \\ \sigma_{xy} \\ v_x \\ v_y \end{bmatrix}_{x_3^s} = \left[0\right]. \tag{6.59}$$

Comparing equations 6.59 and 6.54, one obtains:

$$\begin{bmatrix} \begin{bmatrix} I_{h,s} \end{bmatrix} \begin{bmatrix} T^h \end{bmatrix}^{-1} & \begin{bmatrix} J_{h,s} \end{bmatrix} \begin{bmatrix} T^s \end{bmatrix} & 0 \\ 0 & \begin{bmatrix} I_{s,a} \end{bmatrix} & \begin{bmatrix} J_{s,a} \end{bmatrix} \end{bmatrix} \begin{bmatrix} \begin{bmatrix} p \\ x \end{bmatrix}_{x_1^a} \\ \begin{bmatrix} \sigma_{xx} \\ \sigma_{xy} \\ v_x \\ v_y \end{bmatrix}_{x_3^s} \\ \begin{bmatrix} p \\ x \end{bmatrix}_{x_3^a} \end{bmatrix} = \begin{bmatrix} 0 \\ 0 \\ 0 \\ 0 \\ 0 \\ 0 \end{bmatrix} \tag{6.60}$$

i.e. a system of 6 equations in 8 unknowns. If $[D]$ is the 6×8 matrix at left hand side of equation 6.60, two lines must be added to $[D]$ to solve the system. The first boundary condition is the condition at x_3^a: at transmission side the termination is anechoic, therefore the impedance at x_3^a is known and is the impedance of air. The matrix $[D]$ must be extended at the end by adding the following equation:

$$p|_{x_3^a} - Z_a v|_{x_3^a} = 0 \tag{6.61}$$

while at the beginning it can be expanded by adding one of the equations 6.14 or 6.15:

$$p|_{x_1^a} - e^{jk_a L} \left(\frac{1+R}{T} \right) p|_{x_3^a} = 0 \tag{6.62}$$

$$v|_{x_1^a} - e^{jk_a L} \left(\frac{1-R}{T} \right) v|_{x_3^a} = 0 \tag{6.63}$$

where R_c is the reflection coefficient and T_c the transmission coefficient. In this way, the following complete square matrices are obtained:

$$\left[D_1\right] = \begin{bmatrix} 1 & 0 & 0 & \cdots & 0 & d_1 & 0 \\ & & & \left[D\right] & & & \\ 0 & 0 & 0 & \cdots & 0 & 1 & -Z_a \end{bmatrix} \quad \text{with} \quad d_1 = -e^{jk_aL}\left(\frac{1+R}{T}\right) \tag{6.64}$$

$$\left[D_2\right] = \begin{bmatrix} 0 & 1 & 0 & \cdots & 0 & 0 & d_2 \\ & & & \left[D\right] & & & \\ 0 & 0 & 0 & \cdots & 0 & 1 & -Z_a \end{bmatrix} \quad \text{with} \quad d_2 = -e^{jk_aL}\left(\frac{1-R}{T}\right) \tag{6.65}$$

where d_1 and d_2 are the two unknowns. In both cases ($[D_1]$ or $[D_2]$), the determinant of the extended square matrix must be 0 to have a non-trivial solution of the linear homogeneous system of equations. Solving $|D_1| = 0$ for d_1 and $|D_2| = 0$ for d_2, R_c and in particular T_c can be calculated:

$$R_c = \frac{d_1 - d_2}{d_1 + d_2} \tag{6.66}$$

$$T_c = -\frac{2e^{jk_aL}}{d_1 + d_2}. \tag{6.67}$$

6.2 Experimental Characterization

The experimental device used is the Medium Kundt Tube (Section 4.3.2), with an anechoic termination. The termination is effective from above 400Hz, a range where the absorption coefficient in the case of empty tube (Fig. 6.3) is higher than 0.99.
Four different shaped samples (Tab. 6.1) have been tested. Configuration D, charac-

Configuration	**External cross section**		**Internal cross section**		**Mesoporosity**	**Thickness**
	Shape	Dimension (mm)	Shape	Dimension (mm)	(-)	(mm)
A	circular	$r = 50$	square	$l = 21$	0.056	45.5
B	circular	$r = 50$	square	$l = 30$	0.115	45.5
C	circular	$r = 50$	square	$l = 55.5$	0.392	45.5
D	circular	$r = 50$	circular	$r = 23$	0.212	45.5

Table 6.1: Medium Kundt Tube geometries

terized by a circular internal cross section, does not have the same mesoporosity as

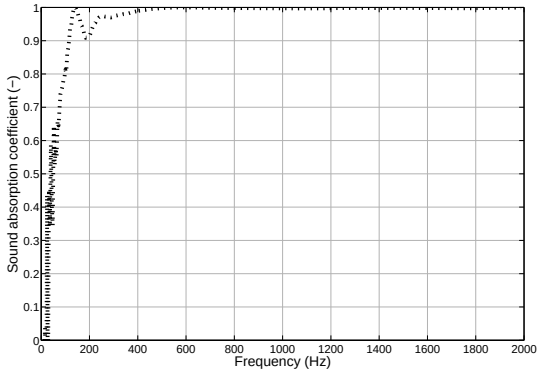

Figure 6.3: Test of the performances of the anechoic termination in the Medium Kundt Tube: the sound absorption coefficient, in case of the empty tube, assumes a value of 0.99 at 408Hz

Configuration C (as done for the Small Kundt Tube), however is here reported as well. The materials are the same used for the case of absorption: $u160$ and *melamine* (Section 4.3.1).

Two layer distributions have been measured. In the first one, the material sample is simply placed in the Kundt tube (resembling the model in Fig. 6.2(a)). The sample has been cut in the way that the diameter fits the tube (the sample position in the tube is not modified when the sample is invested by the acoustic pressure) and no air gaps are observed, but at the same time there is no relevant compression of the sample. When necessary, teflon has been used to avoid air gaps. In the second one, the material sample is backed by a thin aluminium layer (resembling the model in Fig. 6.2(b)) in order to simulate the condition of practical applications (for example the case where the material covers the walls of a box containing a noisy machine). The aluminium layer has been glued to the Kundt tube surfaces using silicone. However, in this case the experimental measurements have been performed a long time after having glued the material (one or two days later). In this way, the aluminium layer remained in place when the sample was invested by the acoustic pressure, and at silicone was flexible not to have completely clamped boundary conditions. The hypothesis of infinite layer, has been assumed acceptable in this case.

6.2.1 Material sample without backing

Effect of mesoporosity

The effect of a mesoporosity variation is represented in Fig. 6.4. In general, for both cases of double porosity and heterogeneous material with an inclusion, the Transmission Loss is decreased when increasing the mesoporosity. In fact, being the internal material less resistive (or simply being the hole increased, in the case of double porosity), the sound wave is transmitted with less resistance when the mesoporosity in increased. The TL decrease is observed on the whole frequency range. Now the effect is negative, differently from the case of absorption. When a complex structure is involved and there is interest in a good behavior both in absorption and in transmission, these results suggest to find an opportune compromise for the value of mesoporosity. The optimized value will obviously depend on the system under study, and as shown in Chapter 4 and here, will in particular depend on the materials characteristics and on the perforations geometry.

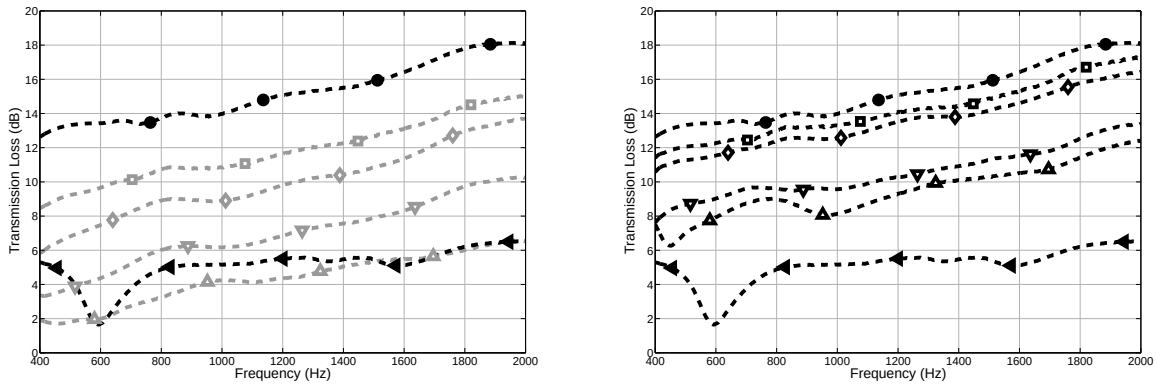

(a) Double porosity - configurations A (--□--), B (--◇--), C (--△--) and D (--▽--)

(b) U160 with a melamine inclusion - configurations A (--■--), B (--◆--), C (--▲--) and D (--▼--)

Figure 6.4: Medium Kundt Tube, 45.5mm thick layer - influence of the mesoporosity on Transmission Loss: different configurations compared to the homogeneous $u160$ (--●--) and to the homogeneous *melamine* (--◀--)

Effect of inclusions

The relative difference between the double porosity and heterogeneous cases are shown (Fig. 6.5). There is a positive effect due to the use of the inclusion. In fact, the difference

in terms of Transmission Loss between the original material and the heterogeneous material is significantly less accentuated than in the case of double porosity. As expected, heterogeneous materials always perform better in transmission than the corresponding double porosity material.

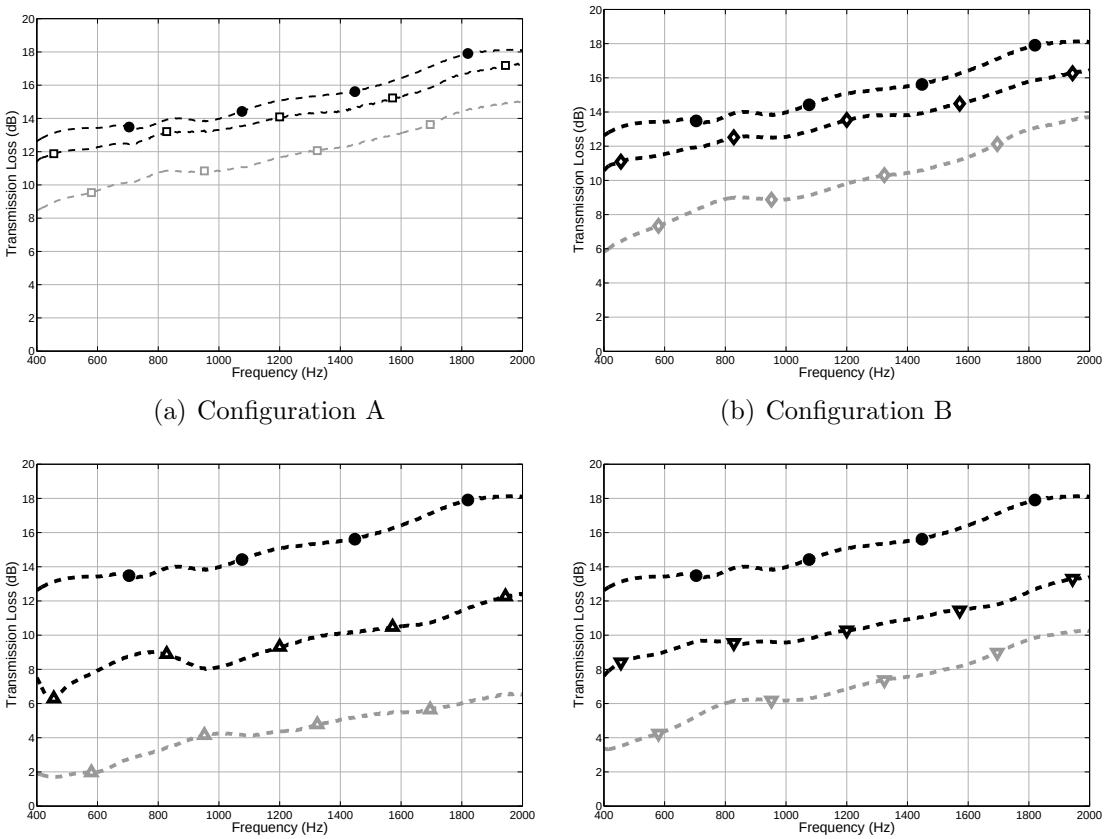

(a) Configuration A

(b) Configuration B

(c) Configuration C

(d) Configuration D

Figure 6.5: Medium Kundt Tube, 45.5mm thick layer, influence of a melamine inclusion on Transmission Loss - comparison between double porosity (dashed grey), heterogeneous material with inclusion of melamine (dashed black) and the homogeneous $u160$ (--●--). The curve markers are the same as in Fig. 6.4(a) and 6.4(b)

6.2.2 Material sample backed by an Aluminium plate

Effect of mesoporosity

The effect of a mesoporosity variation is represented in Fig. 6.6. Analogous considerations than the ones stated for the case of a sample without rigid backing can be repeated.

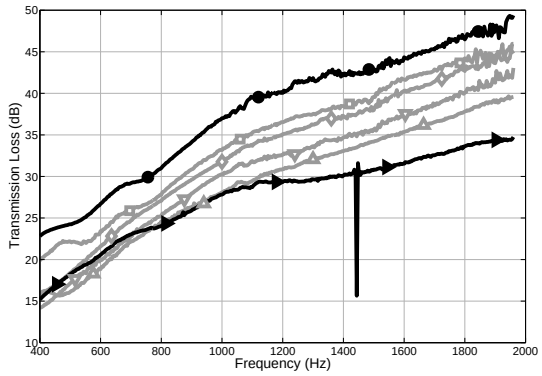

(a) Double porosity - configurations A (—□—), B (—◇—), C (—△—) and D (—▽—)

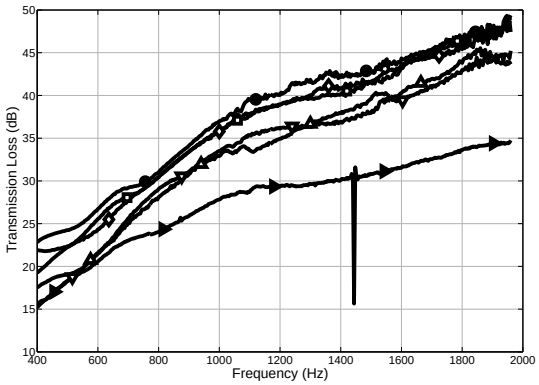

(b) U160 with a melamine inclusion - configurations A (—□—), B (—◇—), C (—△—) and D (—▽—)

Figure 6.6: Medium Kundt Tube, 45.5mm thick layer backed by an Aluminium plate - influence of the mesoporosity on Transmission Loss: different configurations compared to the homogeneous $u160$ (—●—) and to the homogeneous Aluminium plate (—▶—)

Effect of inclusions

The relative difference between the double porosity and heterogeneous cases are shown (Fig. 6.7). Analogous considerations than the ones stated for the case of a sample without rigid backing can be repeated: the positive effect of the inclusion of a porous material in case of transmission, when compared to double porosity, is confirmed also for the case of a more complex configuration where a solid elastic layer is involved.

6.3 Validation

The analytical model described in Section 6.1 is validated against the experimental measurements described in Section 6.2.

6.3.1 Material sample without backing

The comparison between analytical model and experimental measurements is presented in Figures 6.8 and 6.9. A good agreement is shown, for both cases of double porosity and heterogeneous material. In the case of absorption, the condition of an unclear permeability contrast imposed to fix a specific diffusion frequency for the configurations

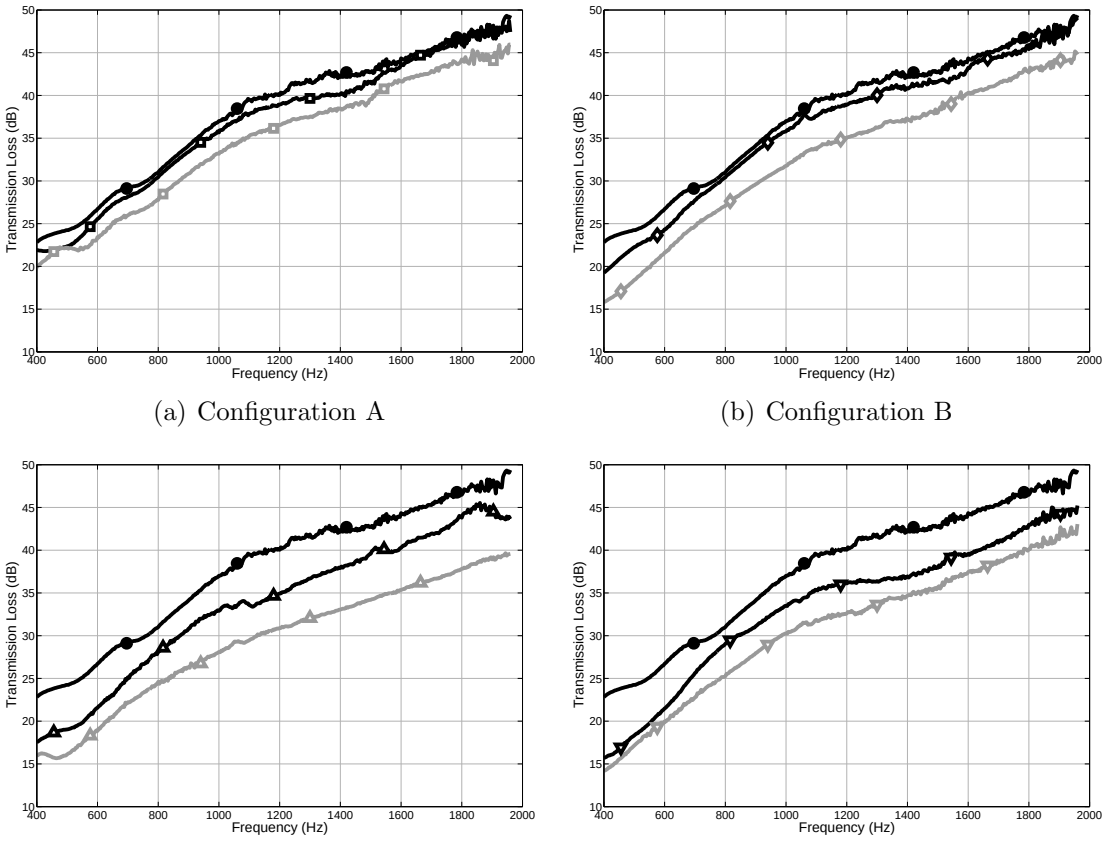

(a) Configuration A

(b) Configuration B

(c) Configuration C

(d) Configuration D

Figure 6.7: Medium Kundt Tube, 45.5mm thick layer backed by an Aluminium plate, influence of a melamine inclusion on Transmission Loss - comparison between double porosity (dashed grey), heterogeneous material with inclusion of melamine (dashed black) and the homogeneous $u160$ (—●—). The curve markers are the same as in Fig. 6.6(a) and 6.6(b)

at lower mesoporosity. Differently, in case of transmission, the agreement is satisfactory when the complete diffusion function is considered. If the function F_d is equal to 1 (no pressure diffusion effect), the comparison is not good. This fact leads to suppose that the permeability contrast is higher and consistent to the value predicted by the analytical model. This fact can be explained because in the case of transmission, a greater area of exchange is involved in the calculation of the pressure diffusion effect, being considered also the area on the transmission side that is in contact with air or with another layer (and not a rigid backing). Therefore, the diffusion function assumes different values and it can be explained in this case that the diffusion effects assume the behavior predicted by the model.

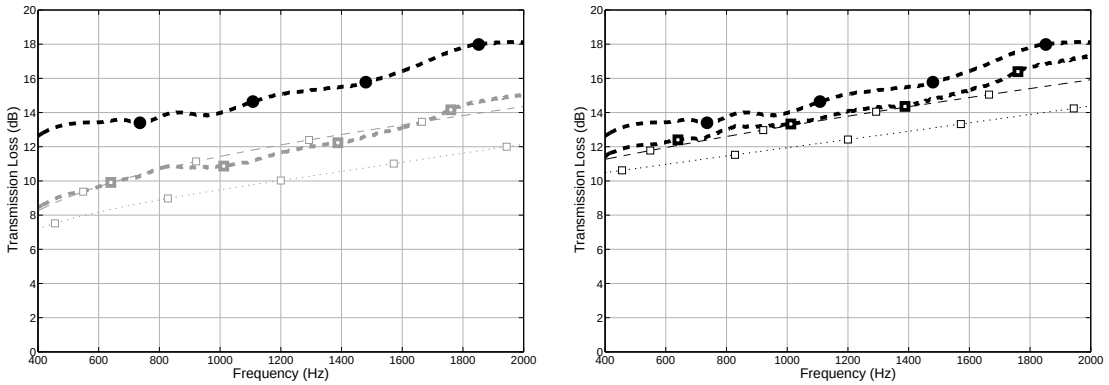

(a) Configuration A, double porosity: comparison between experimental data (–□–) and analytical model in case of $F_d = F_d(\omega)$ (––□––) and $F_d = 1$ (----□----)

(b) Configuration A, heterogeneous material: comparison between experimental data (–□–) and analytical model in case of $F_d = F_d(\omega)$ (––□––) and $F_d = 1$ (----□----)

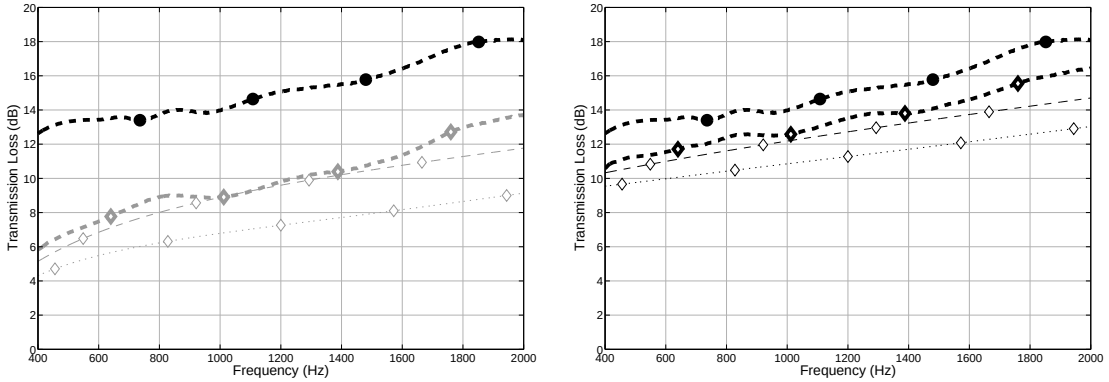

(c) Configuration B, double porosity: comparison between experimental data (–◇–) and analytical model in case of $F_d = F_d(\omega)$ (––◇––) and $F_d = 1$ (----◇----)

(d) Configuration B, heterogeneous material: comparison between experimental data (–◇–) and analytical model in case of $F_d = F_d(\omega)$ (––◇––) and $F_d = 1$ (----◇----)

Figure 6.8: Medium Kundt Tube, 45.5mm thick layer, validation for configurations A and B

6.3.2 Material sample backed by an Aluminium plate

The properties presented in Table 6.2 have been used for the Aluminium plate. Thickness and density have been measured from the used sample; the other parameters are taken from [1]. The comparison between analytical model and experimental measurements is

$\rho(kg\,m^{-3})$	$E\,(Pa)$	ν	$thickness\,(mm)$
2745	7.2×10^{10}	0.3	1

Table 6.2: Aluminium properties; the thickness is referred to the sample used for the experimental measurements

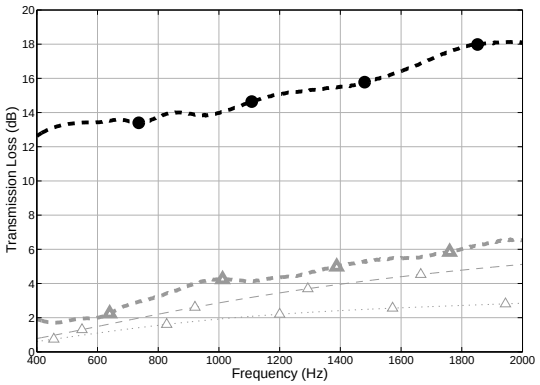

(a) Configuration C, double porosity: comparison between experimental data (--△--) and analytical model in case of $F_d = F_d(\omega)$ (--△--) and $F_d = 1$ (----△----)

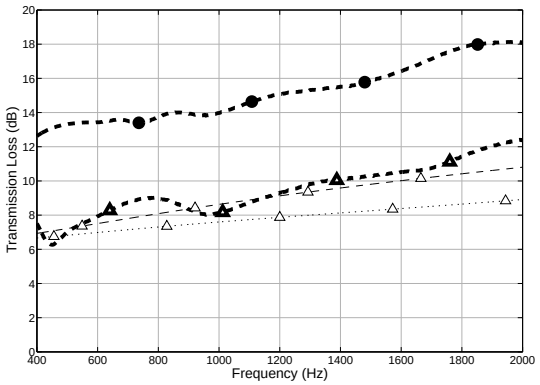

(b) Configuration C, heterogeneous material: comparison between experimental data (--△--) and analytical model in case of $F_d = F_d(\omega)$ (--△--) and $F_d = 1$ (----△----)

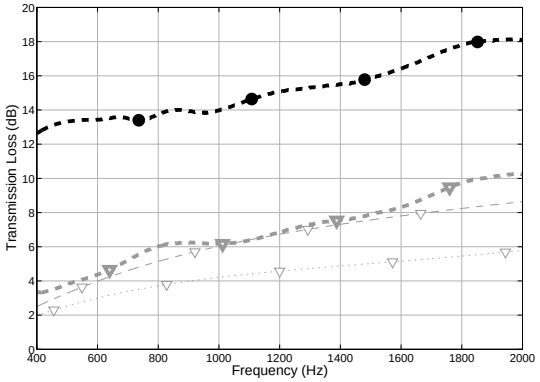

(c) Configuration D, double porosity: comparison between experimental data (--▽--) and analytical model in case of $F_d = F_d(\omega)$ (--▽--) and $F_d = 1$ (----▽----)

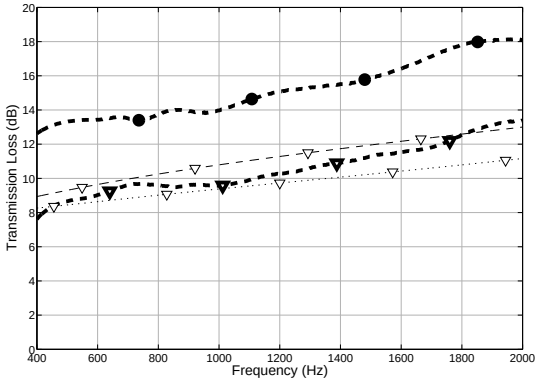

(d) Configuration D, heterogeneous material: comparison between experimental data (--▽--) and analytical model in case of $F_d = F_d(\omega)$ (--▽--) and $F_d = 1$ (----▽----)

Figure 6.9: Medium Kundt Tube, 45.5mm thick layer, validation for configurations C and D

presented in Figures 6.10 and 6.11. When a plate is present on the back of the sample, the agreement between experimental and analytical curves is still acceptable but less satisfactory. In fact, the trend of the curves is respected, however some differences are quite relevant. This behavior can be explained considering that with the introduction of the plate the system is more complicated and the boundary conditions are more difficult to control during the experimental measurements. In particular, two conditions have to be taken into account:

- the Aluminium plate has been fixed (not rigidly) to the Tube edges with silicon, to avoid air gaps; in this case, the condition on boundaries is probably in contrast with the theoretical hypothesis of infinite layer;

- the sample and the plate have not been glued for practical reasons, therefore some gaps can have had en effect on the experimental data.

Finally, it can be noticed that the agreement is better in the case of double porosity than in the case of heterogeneous material with inclusions. In any case, the trend is correct and the model can be used especially to track in theory the differences between different mesoporosities or between the double porosity and the heterogeneous configurations.

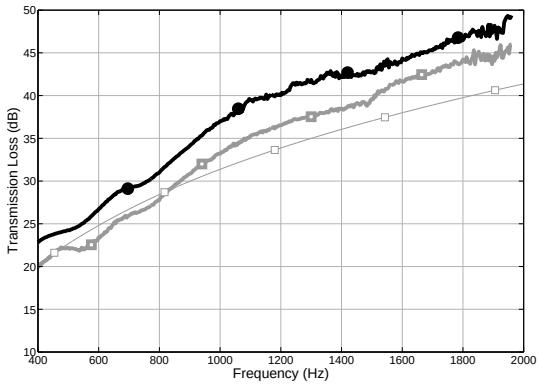

(a) Configuration A, double porosity: comparison between experimental data (—□—) and analytical model in case of $F_d = F_d(\omega)$ (—□—)

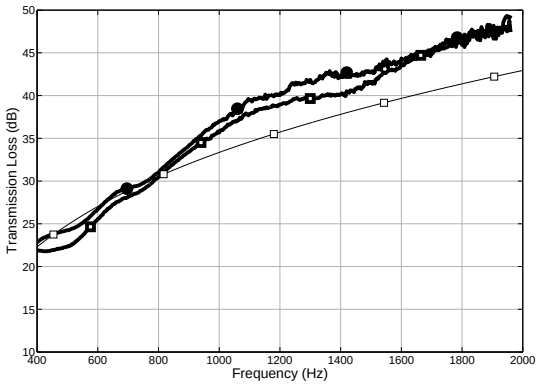

(b) Configuration A, heterogeneous material: comparison between experimental data (—□—) and analytical model in case of $F_d = F_d(\omega)$ (—□—)

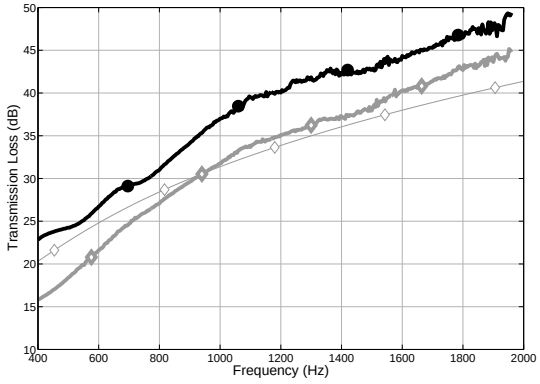

(c) Configuration B, double porosity: comparison between experimental data (—◇—) and analytical model in case of $F_d = F_d(\omega)$ (—◇—)

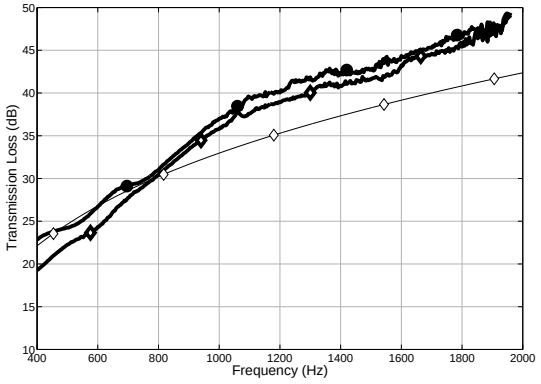

(d) Configuration B, heterogeneous material: comparison between experimental data (—◇—) and analytical model in case of $F_d = F_d(\omega)$ (—◇—)

Figure 6.10: Medium Kundt Tube, 45.5mm thick layer, validation for configurations A and B

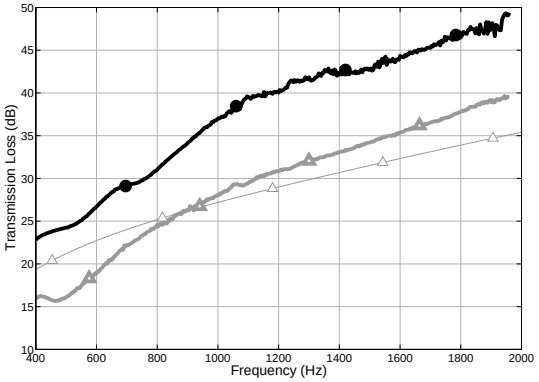

(a) Configuration C, double porosity: comparison between experimental data (—△—) and analytical model in case of $F_d = F_d(\omega)$ (—△—)

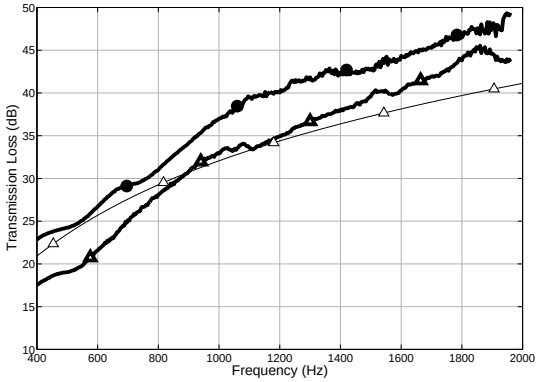

(b) Configuration C, heterogeneous material: comparison between experimental data (—△—) and analytical model in case of $F_d = F_d(\omega)$ (—△—)

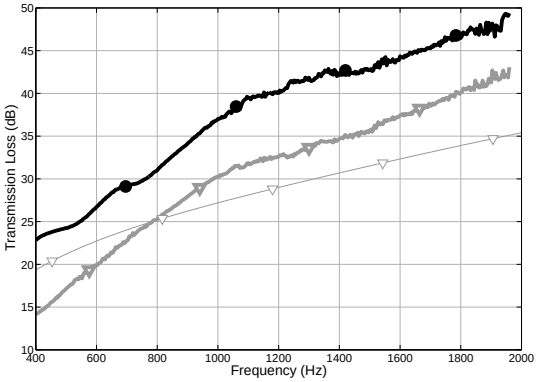

(c) Configuration D, double porosity: comparison between experimental data (—▽—) and analytical model in case of $F_d = F_d(\omega)$ (—▽—)

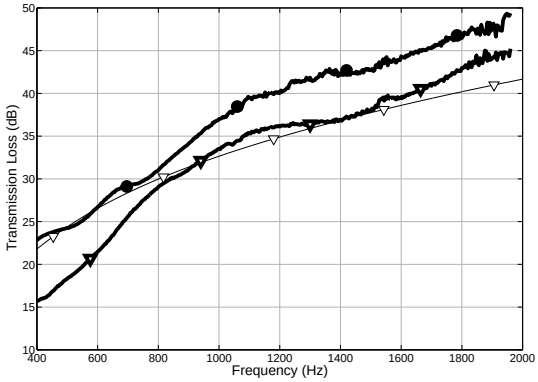

(d) Configuration D, heterogeneous material: comparison between experimental data (—▽—) and analytical model in case of $F_d = F_d(\omega)$ (—▽—)

Figure 6.11: Medium Kundt Tube, 45.5mm thick layer, validation for configurations C and D

7 Concluding remarks

The present work was focused on the study of specific numerical and analytical methods for the vibro-acoustic modelling of porous materials. Analytical methods are in general subjected to restrictive hypotheses but give the advantage of a faster computational solution. A simplified model based on the theory of double porosity has been validated for the specific case of periodic inclusions of a second poroelastic material, through comparison with experimental and numerical data. Some limitations in its validity must be considered, but the method can be used with prudence also in cases that do not respect the theoretical hypotheses (for example, the periodicity), provided that the effective physical situation is taken into account (in particular, the situation of high or low permeability contrast). However, the validation has been performed for two couples of materials and further investigations would be opportune to verify the criteria adopted in case the theoretical hypotheses are not respected. In this context, an interesting investigation could involve the analysis of the pressure diffusion function. In fact, more detailed expressions of the pressure diffusion function could take into account more general geometries than the ones considered and possibly the case of a single cell. Alternatively, numerical methods (for example Finite Elements) could be used to derive expressions of the pressure diffusion function, as the latter depends only on geometry. An abacus could be created, as function of the geometrical parameters of the cell and the perforation. Moreover, further investigations would be interesting when transmission of sound is concerned. The experimental characterization of samples backed by plates is quite complex and some more work would be suited to the comparison with the analytical solution. Another interesting study that has been partially planned will involve different concepts of hybrid solutions, creating a perforated sample with different kinds of heterogeneities, as for example the case of a perforated layer with only some holes filled by inclusions and other left void. The aim would be to verify the influence of mesoporosity, that represents a key parameter linked to the performances of the layer, also in a generalized configuration.

On the other hand, there is a need for numerical methods when real geometries are involved. In this case the issues are related mainly to computational times and convergence. In this context, the Cell Method is attractive for its easiness of implementation, for its natural management of boundary conditions and for a good expected convergence behavior, that would be worth to be investigated. At the same time, tetrahedral elements can be defined naturally, as has been done in an original way for the case of 3-D quadratic tetrahedra. This reveals to be an important issue when the human time necessary for meshing real complex geometries can be reduced. Further interesting studies would involve the management of interfaces between a porous domain and solid or fluid domains (the conditions can be derived starting from the ones defined in Chapter 3) and the application of the Cell Method to the case of inclusions, as done in Chapter 5 with Finite Elements.

A Detailed expressions for the Cell Method

A.1 Geometrical details

Given the four vertices of a tetrahedron, the vector areas for each p-th face can be defined as follows:

$$\mathbf{A}_p = (-1)^p \mathbf{A}_{qrs} \tag{A.1}$$

where $p \in [1,2,3,4]$ and $q,r,s \in [1,2,3,4]$ with $p \neq q \neq r \neq s$. The p-th face is the face opposite to the vertex p. The vector area cartesian components can be formalized as follows:

$$A_{qrs,x} = \frac{1}{2}\begin{vmatrix} 1 & y_q & z_q \\ 1 & y_r & z_r \\ 1 & y_s & z_s \end{vmatrix} \qquad A_{qrs,y} = \frac{1}{2}\begin{vmatrix} 1 & z_q & x_q \\ 1 & z_r & x_r \\ 1 & z_s & x_s \end{vmatrix} \qquad A_{qrs,z} = \frac{1}{2}\begin{vmatrix} 1 & x_q & y_q \\ 1 & x_r & y_r \\ 1 & x_s & y_s \end{vmatrix} \tag{A.2}$$

and similarly the total volume of the tetrahedral cell V_c is

$$V_c = \frac{1}{6}\begin{vmatrix} 1 & x_1 & y_1 & z_1 \\ 1 & x_2 & y_2 & z_2 \\ 1 & x_3 & y_3 & z_3 \\ 1 & x_4 & y_4 & z_4 \end{vmatrix}. \tag{A.3}$$

Also the following geometrical expression is used for the calculation of the elementary matrices:

$$6v_p = (-1)^{p+1} \begin{vmatrix} x_q & y_q & z_q \\ x_r & y_r & z_r \\ x_s & y_s & z_s \end{vmatrix} \tag{A.4}$$

where the notation is the same as above. The quantity v_p represents the volume of the tetrahedron whose vertices are the origin of the axes and the vertices belonging to the p-th face.

A.2 Shape functions for the linear tetrahedron

Superscripts are omitted because the derivation is identical for both solid and fluid phases. Eq. 2.20 must be valid at each node of the tetrahedron:

$$\begin{bmatrix} u_{p,1} \\ u_{p,2} \\ u_{p,3} \\ u_{p,4} \end{bmatrix} = \begin{bmatrix} 1 & x_1 & y_1 & z_1 \\ 1 & x_2 & y_2 & z_2 \\ 1 & x_3 & y_3 & z_3 \\ 1 & x_4 & y_4 & z_4 \end{bmatrix} \begin{bmatrix} a_p \\ b_p \\ c_p \\ d_p \end{bmatrix}, \quad p = x, y, z \tag{A.5}$$

where $u_{p,q}$ is the p-th component of the vector displacement $\mathbf{u}$ at the q-th element node. Introducing the metric linear shape functions N, we can define:

$$\begin{bmatrix} N_1 & N_2 & N_3 & N_4 \end{bmatrix} = \begin{bmatrix} 1 & x & y & z \end{bmatrix} \begin{bmatrix} 1 & x_1 & y_1 & z_1 \\ 1 & x_2 & y_2 & z_2 \\ 1 & x_3 & y_3 & z_3 \\ 1 & x_4 & y_4 & z_4 \end{bmatrix}^{-1} \tag{A.6}$$

With this notation, one can obtain:

$$u_p = \begin{bmatrix} N_1 & N_2 & N_3 & N_4 \end{bmatrix} \begin{bmatrix} u_{p,1} \\ u_{p,2} \\ u_{p,3} \\ u_{p,4} \end{bmatrix}, \quad p = x, y, z \tag{A.7}$$

and

$$\mathbf{u} = \begin{bmatrix} u_x \\ u_y \\ u_z \end{bmatrix} = \begin{bmatrix} N_1 & 0 & 0 & N_2 & 0 & 0 & N_3 & 0 & 0 & N_4 & 0 & 0 \\ 0 & N_1 & 0 & 0 & N_2 & 0 & 0 & N_3 & 0 & 0 & N_4 & 0 \\ 0 & 0 & N_1 & 0 & 0 & N_2 & 0 & 0 & N_3 & 0 & 0 & N_4 \end{bmatrix} \begin{bmatrix} u_{x,1} \\ \vdots \\ u_{z,4} \end{bmatrix} \tag{A.8}$$

that are here recalled, being the well known expressions used for linear shape functions in the Finite Elements. Eq. A.8 connects the generic displacement into the primal cell to the displacements of its nodes, described by 3 components $\times 4$ nodes $= 12$ components for each phase, in the linear tetrahedron.

A.3 Shape functions for the quadratic tetrahedron

Superscripts are omitted because the derivation is identical for both solid and fluid phases. Eq. 2.26 must be valid at each node of the tetrahedron; similarly to the linear case, the shape functions can be expressed as:

$$\begin{bmatrix} N_1 & \cdots & N_{10} \end{bmatrix} = \begin{bmatrix} 1 & \cdots & zx \end{bmatrix} \begin{bmatrix} 1 & \cdots & z_1 x_1 \\ \vdots & & \vdots \\ 1 & \cdots & z_{10} x_{10} \end{bmatrix}^{-1} \tag{A.9}$$

With this notation, one can obtain:

$$u_p = \begin{bmatrix} N_1 & \cdots & N_{10} \end{bmatrix} \begin{bmatrix} u_{p,1} \\ \vdots \\ u_{p,10} \end{bmatrix}, \quad p = x, y, z \tag{A.10}$$

and

$$\mathbf{u} = \begin{bmatrix} u_x \\ u_y \\ u_z \end{bmatrix} = \begin{bmatrix} N_1 & 0 & 0 & \cdots & N_{10} & 0 & 0 \\ 0 & N_1 & 0 & \cdots & 0 & N_{10} & 0 \\ 0 & 0 & N_1 & \cdots & 0 & 0 & N_{10} \end{bmatrix} \begin{bmatrix} u_{x,1} \\ \vdots \\ u_{z,10} \end{bmatrix} \tag{A.11}$$

Eq. A.11 connects the generic displacement into the primal cell to the displacements of its nodes, described by 3 components $\times 10$ nodes $= 30$ components for each phase, in the quadratic tetrahedron.

A.3.1 Integration of the shape functions for the quadratic tetrahedron

For the quadratic tetrahedron, the following geometrical coefficients have to be inserted into Eq. 2.29. The terms defined as:

$$\left[\bar{I}_1\right](\hat{C}_{i,\xi}) = g^3 V_c \begin{bmatrix} 1 \\ (1-\frac{3}{4}g)x_\xi + \frac{g}{4}S_{1,x} \\ (1-\frac{3}{4}g)y_\xi + \frac{g}{4}S_{1,y} \\ (1-\frac{3}{4}g)z_\xi + \frac{g}{4}S_{1,z} \\ (1-\frac{3}{2}g+\frac{3}{5}g^2)x_\xi^2 + (\frac{1}{2}g-\frac{2}{5}g^2)x_\xi S_{1,x} + \frac{1}{10}g^2 P_{1,x} + \frac{1}{10}g^2 S_{2,x} \\ (1-\frac{3}{2}g+\frac{3}{5}g^2)y_\xi^2 + (\frac{1}{2}g-\frac{2}{5}g^2)y_\xi S_{1,y} + \frac{1}{10}g^2 P_{1,y} + \frac{1}{10}g^2 S_{2,y} \\ (1-\frac{3}{2}g+\frac{3}{5}g^2)z_\xi^2 + (\frac{1}{2}g-\frac{2}{5}g^2)z_\xi S_{1,z} + \frac{1}{10}g^2 P_{1,z} + \frac{1}{10}g^2 S_{2,z} \\ (1-\frac{3}{2}g+\frac{3}{5}g^2)x_\xi y_\xi + (\frac{1}{4}g-\frac{1}{5}g^2)(x_\xi S_{1,y} + y_\xi S_{1,x}) + \frac{1}{10}g^2 P_{2,x,y} + \frac{1}{20}g^2 P_{3,x,y} \\ (1-\frac{3}{2}g+\frac{3}{5}g^2)y_\xi z_\xi + (\frac{1}{4}g-\frac{1}{5}g^2)(y_\xi S_{1,z} + z_\xi S_{1,y}) + \frac{1}{10}g^2 P_{2,y,z} + \frac{1}{20}g^2 P_{3,y,z} \\ (1-\frac{3}{2}g+\frac{3}{5}g^2)z_\xi x_\xi + (\frac{1}{4}g-\frac{1}{5}g^2)(z_\xi S_{1,x} + x_\xi S_{1,z}) + \frac{1}{10}g^2 P_{2,z,x} + \frac{1}{20}g^2 P_{3,z,x} \end{bmatrix} \tag{A.12}$$

and

$$\left[\bar{I}_2\right](\hat{C}_{i,\xi}) = V_c \begin{bmatrix} \frac{1}{4} \\ \frac{75}{576}x_\xi + \frac{23}{576}S_{1,x} \\ \frac{75}{576}y_\xi + \frac{23}{576}S_{1,y} \\ \frac{75}{576}z_\xi + \frac{23}{576}S_{1,z} \\ \frac{53}{960}x_\xi^2 + \frac{1}{20}x_\xi S_{1,x} + \frac{7}{1152}P_{1,x} + \frac{17}{1920}S_{2,x} \\ \frac{53}{960}y_\xi^2 + \frac{1}{20}y_\xi S_{1,y} + \frac{7}{1152}P_{1,y} + \frac{17}{1920}S_{2,y} \\ \frac{53}{960}z_\xi^2 + \frac{1}{20}z_\xi S_{1,z} + \frac{7}{1152}P_{1,z} + \frac{17}{1920}S_{2,z} \\ \frac{47}{640}x_\xi y_\xi + \frac{109}{5760}(x_\xi S_{1,y} + y_\xi S_{1,x}) + \frac{17}{1920}P_{2,x,y} + \frac{7}{1152}P_{3,x,y} \\ \frac{47}{640}y_\xi z_\xi + \frac{109}{5760}(y_\xi S_{1,z} + z_\xi S_{1,y}) + \frac{17}{1920}P_{2,y,z} + \frac{7}{1152}P_{3,y,z} \\ \frac{47}{640}z_\xi x_\xi + \frac{109}{5760}(z_\xi S_{1,x} + x_\xi S_{1,z}) + \frac{17}{1920}P_{2,z,x} + \frac{7}{1152}P_{3,z,x} \end{bmatrix} \tag{A.13}$$

where

$$\begin{aligned} S_{1,x} &= x_{\xi'} + x_{\xi''} + x_{\xi'''} & S_{2,x} &= x_{\xi'}^2 + x_{\xi''}^2 + x_{\xi'''}^2 \\ S_{1,y} &= y_{\xi'} + y_{\xi''} + y_{\xi'''} & S_{2,y} &= y_{\xi'}^2 + y_{\xi''}^2 + y_{\xi'''}^2 \\ S_{1,z} &= z_{\xi'} + z_{\xi''} + z_{\xi'''} & S_{2,z} &= z_{\xi'}^2 + z_{\xi''}^2 + z_{\xi'''}^2 \\ P_{1,x} &= x_{\xi'}x_{\xi''} + x_{\xi'}x_{\xi'''} + x_{\xi''}x_{\xi'''} & P_{2,x,y} &= x_{\xi'}y_{\xi'} + x_{\xi''}y_{\xi''} + x_{\xi'''}y_{\xi'''} \\ P_{1,y} &= y_{\xi'}y_{\xi''} + y_{\xi'}y_{\xi'''} + y_{\xi''}y_{\xi'''} & P_{2,y,z} &= y_{\xi'}z_{\xi'} + y_{\xi''}z_{\xi''} + y_{\xi'''}z_{\xi'''} \\ P_{1,z} &= z_{\xi'}z_{\xi''} + z_{\xi'}z_{\xi'''} + z_{\xi''}z_{\xi'''} & P_{2,z,x} &= z_{\xi'}x_{\xi'} + z_{\xi''}x_{\xi''} + z_{\xi'''}x_{\xi'''} \\ P_{3,x,y} &= x_{\xi'}(y_{\xi''} + y_{\xi'''}) + x_{\xi''}(y_{\xi'} + y_{\xi'''}) + x_{\xi'''}(y_{\xi'} + y_{\xi''}) \\ P_{3,y,z} &= y_{\xi'}(z_{\xi''} + z_{\xi'''}) + y_{\xi''}(z_{\xi'} + z_{\xi'''}) + y_{\xi'''}(z_{\xi'} + z_{\xi''}) \\ P_{3,z,x} &= z_{\xi'}(x_{\xi''} + x_{\xi'''}) + z_{\xi''}(x_{\xi'} + x_{\xi'''}) + z_{\xi'''}(x_{\xi'} + x_{\xi''}) \end{aligned}$$

are a formalization of the results of the integration on different parts of the quadratic tetrahedron. In Eq. A.12 and A.13, ξ represents one of the 4 nodes that are also vertices of the tetrahedron and once the node ξ is fixed, the remaining 3 nodes representing also vertices of the tetrahedron are indexed by ξ', ξ'' and ξ'''.
The expression of the vector $\left[\bar{N}_{gc}^{i,\alpha}\right]$ in Eq. 2.29 is function of the node where the integral

is calculated:

$$\left[\bar{N}_{gc}^{i,\alpha}\right] = \begin{cases} \left[\bar{I}_1\right](\hat{C}_{i,\alpha}) & \text{if } \alpha = 1,2,3,4 \\ \frac{1}{3}\left[\bar{I}_2\right](\hat{C}_{i,\beta}) + \frac{1}{3}\left[\bar{I}_2\right](\hat{C}_{i,\gamma}) - \frac{1}{3}\left[\bar{I}_1\right](\hat{C}_{i,\beta}) - \frac{1}{3}\left[\bar{I}_1\right](\hat{C}_{i,\gamma}) & \text{if } \alpha = 5,6,7,8,9,10 \end{cases} \tag{A.14}$$

In the second case, β and γ represent the 2 adjacent nodes, that are also vertices of the tetrahedron, of the node α, as follows (see Fig. 2.4 in Section 2.2.5):

α	5	6	7	8	9	10
β	1	1	1	2	3	3
γ	2	3	4	3	4	4

B Assembly process in the Cell Method

A general procedure is presented to assemble the elementary matrices to obtain the global dynamical matrix, for the case of the Biot's theory. For the Cell Method, the assembly is based on the connectivity matrix and is analogous to the case of Finite Elements, as will be demonstrated. With the notation introduced in 2.2.2, Equation 2.19 can be rewritten:

$$\sum_{i \in \mathcal{P}_k} (\mathbf{K}^s_{i,\alpha(k)} + j\omega \mathbf{D}^s_{i,\alpha(k)} - \omega^2 \mathbf{M}^s_{i,\alpha(k)}) \cdot \mathbf{u}_i = \mathbf{f_E}^s_{i,\alpha(k)} \tag{B.1}$$

$$\sum_{i \in \mathcal{P}_k} (\mathbf{K}^f_{i,\alpha(k)} + j\omega \mathbf{D}^f_{i,\alpha(k)} - \omega^2 \mathbf{M}^f_{i,\alpha(k)}) \cdot \mathbf{u}_i = \mathbf{f_E}^f_{i,\alpha(k)} \tag{B.2}$$

and is valid $\forall k \in \mathcal{D}$. In the above equations the solid and fluid phases (superscripts s and f) are separated; i is the global index for the primal cell, k is the global index for the dual cell (and therefore for the node) and α is the local index for the dual cell (and therefore for the node). The link between the local and global notation is expressed by $\alpha(k)$. $\mathcal{P}_k$ is the the set of primal cells that contain the k-th node.

The above equations can be rewritten:

$$\sum_{i \in \mathcal{P}_1} \mathbf{DK}^s_{i,\alpha(1)} \cdot \mathbf{u}_i = \mathbf{f_E}^s_{i,\alpha(1)} \tag{B.3}$$

$$\sum_{i \in \mathcal{P}_1} \mathbf{DK}^f_{i,\alpha(1)} \cdot \mathbf{u}_i = \mathbf{f_E}^f_{i,\alpha(1)} \tag{B.4}$$

$$\cdots$$

$$\sum_{i \in \mathcal{P}_n} \mathbf{DK}^s_{i,\alpha(n)} \cdot \mathbf{u}_i = \mathbf{f_E}^s_{i,\alpha(n)} \tag{B.5}$$

$$\sum_{i \in \mathcal{P}_n} \mathbf{DK}^f_{i,\alpha(n)} \cdot \mathbf{u}_i = \mathbf{f_E}^f_{i,\alpha(n)} \tag{B.6}$$

where n is the number of dual cells and

$$\mathbf{DK}^s_{i,\alpha(k)} = \mathbf{K}^s_{i,\alpha(k)} + j\omega\mathbf{D}^s_{i,\alpha(k)} - \omega^2\mathbf{M}^s_{i,\alpha(k)} \tag{B.7}$$

$$\mathbf{DK}^f_{i,\alpha(k)} = \mathbf{K}^f_{i,\alpha(k)} + j\omega\mathbf{D}^f_{i,\alpha(k)} - \omega^2\mathbf{M}^f_{i,\alpha(k)} \tag{B.8}$$

are the dynamical stiffness matrices for the solid and fluid phases. In order to switch between local and global coordinates, the local connectivity matrix $\mathbf{W}_i$ is introduced:

$$\mathbf{u}_i = \mathbf{W}_i \cdot \mathbf{U} \tag{B.9}$$

where $\mathbf{U}$ is the global displacement vector, containing all the solid and fluid degrees of freedom of the system. Being $\mathbf{u}_i$ the vector of the local solid and fluid displacements (i.e. the displacements of the considered cell), $\mathbf{W}_i$ is a sparse $m \times n$ matrix, where m is the number of degrees of freedom of the cell, filled by ones only in the positions where there is correspondence between local and global enumeration. The following quantities are defined:

$$\mathbf{A}^s_{i,\alpha(k)} = \mathbf{DK}^s_{i,\alpha(k)} \cdot \mathbf{W}_i \tag{B.10}$$

$$\mathbf{A}^f_{i,\alpha(k)} = \mathbf{DK}^f_{i,\alpha(k)} \cdot \mathbf{W}_i. \tag{B.11}$$

Writing Equations B.3 and following in a different order (first the solid, then the fluid degrees of freedom) and using Equations B.9 and B.10, one gets:

$$\left(\sum_{i\in\mathcal{P}_1} \mathbf{A}^s_{i,\alpha(1)}\right) \cdot \mathbf{U} = \mathbf{f}_{\mathbf{E}}{}^s_{i,\alpha(1)} \tag{B.12}$$

$$\cdots$$

$$\left(\sum_{i\in\mathcal{P}_n} \mathbf{A}^s_{i,\alpha(n)}\right) \cdot \mathbf{U} = \mathbf{f}_{\mathbf{E}}{}^s_{i,\alpha(n)} \tag{B.13}$$

$$\left(\sum_{i\in\mathcal{P}_1} \mathbf{A}^f_{i,\alpha(1)}\right) \cdot \mathbf{U} = \mathbf{f}_{\mathbf{E}}{}^f_{i,\alpha(1)} \tag{B.14}$$

$$\cdots$$

$$\left(\sum_{i\in\mathcal{P}_n} \mathbf{A}^f_{i,\alpha(n)}\right) \cdot \mathbf{U} = \mathbf{f}_{\mathbf{E}}{}^f_{i,\alpha(n)} \tag{B.15}$$

where the first terms can be expressed as:

$$\sum_{i\in\mathcal{P}_k} \mathbf{A}^s_{i,\alpha} = \sum_{i\in\mathcal{P}} \mathbf{w}^{s\mathsf{T}}_{i,k} \cdot \mathbf{A}_i \tag{B.16}$$

$$\sum_{i\in\mathcal{P}_k} \mathbf{A}^f_{i,\alpha} = \sum_{i\in\mathcal{P}} \mathbf{w}^{f\mathsf{T}}_{i,k} \cdot \mathbf{A}_i \tag{B.17}$$

where the matrix $\mathbf{w}_{i,k}$ takes into account the correspondence between global and local enumeration and $\mathbf{A}_i$ is a matrix containing in column the terms $\mathbf{A}_{i,\alpha(n)}$ (first solid then fluid). In this way, and applying the same considerations to the terms of kind $\mathbf{f}_{\mathbf{E}i,\alpha(1)}$, the Equations B.12 can be rewritten:

$$\left(\sum_{i\in\mathcal{P}} \mathbf{w}^{s\mathsf{T}}_{i,1} \cdot \mathbf{A}_i\right) \cdot \mathbf{U} = \sum_{i\in\mathcal{P}} \mathbf{w}^{s\mathsf{T}}_{i,1} \cdot \mathbf{f}_{\mathbf{E}i} \tag{B.18}$$

$$\cdots$$

$$\left(\sum_{i\in\mathcal{P}} \mathbf{w}^{s\mathsf{T}}_{i,n} \cdot \mathbf{A}_i\right) \cdot \mathbf{U} = \sum_{i\in\mathcal{P}} \mathbf{w}^{s\mathsf{T}}_{i,n} \cdot \mathbf{f}_{\mathbf{E}i} \tag{B.19}$$

$$\left(\sum_{i\in\mathcal{P}} \mathbf{w}^{f\mathsf{T}}_{i,1} \cdot \mathbf{A}_i\right) \cdot \mathbf{U} = \sum_{i\in\mathcal{P}} \mathbf{w}^{f\mathsf{T}}_{i,1} \cdot \mathbf{f}_{\mathbf{E}i} \tag{B.20}$$

$$\cdots$$

$$\left(\sum_{i\in\mathcal{P}} \mathbf{w}^{f\mathsf{T}}_{i,n} \cdot \mathbf{A}_i\right) \cdot \mathbf{U} = \sum_{i\in\mathcal{P}} \mathbf{w}^{f\mathsf{T}}_{i,n} \cdot \mathbf{f}_{\mathbf{E}i} \quad . \tag{B.21}$$

Writing in columns the terms of kind $\mathbf{w}$, it is easy to observe that a matrix $\mathbf{W}^{\mathsf{T}}_i$ is obtained, equal to the transpose of the matrix $\mathbf{W}_i$. It follows that Equations B.18 can be summarized in:

$$\left(\sum_{i\in\mathcal{P}} \mathbf{W}^{\mathsf{T}}_i \cdot \mathbf{DK}_{i,\alpha(k)} \cdot \mathbf{W}_i\right) \cdot \mathbf{U} = \sum_{i\in\mathcal{P}} \mathbf{W}^{\mathsf{T}}_i \cdot \mathbf{f}_{\mathbf{E}i} \tag{B.22}$$

that represent the classical expression for the assembly of the global matrix, as used in case of Finite Elements. The difference in the case of the Cell Method is that Equation B.22 has been obtained relying only on the equilibrium equations and the relationships between local and global enumerations.

Bibliography

[1] J.-F. Allard. *Propagation of sound in porous media. Modeling sound absorbing materials*. Elsevier Applied Sciences, 1993.

[2] J.F. Allard, Y. Champoux, and Depollier C. Modelization of layered sound absorbing materials with transfer matrices. *Journal of the Acoustical Society of America*, 79(6):1734–1740, 1986.

[3] N. Amirouche. Dispositifs absorbents à base de matériaux à double porosité dans des champs acoustiques complexes. *Ph.D. thesis, ENTPE-Institut National des Sciences Appliquées de Lyon, France*, 2008.

[4] N. Atalla, R. Panetton, F.C. Sgard, and X. Olny. Acoustic absorption of porous surfacing with dual porosity.. *Journal of Sound and Vibration*, 243(4):659–678, 2001.

[5] N. Atalla, R. Panneton, and P. Debegue. A mixed displacement-pressure formulation for poroelastic materials. *Journal of the Acoustical Society of America*, 104(3):1444–1452, 1998.

[6] J.-P. Balmont, C.J. Nederveen, and N. Joly. Radiation impedance of tube with different flanges: numerical and experimental investigations. *Journal of Sound and Vibration*, 2001.

[7] C. Bertolini, C. Gaudino, D. Caprioli, K. Misaji, and F. Ide. FE Analysis of a partially trimmed vehicle using poroelastic finite elements based on Biot's theory. *Proceedings of SAE Conference 2007*, 2007.

[8] M.A. Biot. Theory of propagation of elastic waves in a fluid-saturated porous solid. I Low-frequency range. *Journal of the Acoustical Society of America*, 28(2):168–178, 1956.

[9] J.S. Bolton and E.R. Green. Normal incidence sound transmission through double-panel systems lined with relatively stiff, partially reticulated polyurethane foam. *Applied Acoustics*, 39, 1993.

[10] J.S. Bolton, N.M. Shiau, and Y.J. Kang. Sound transmission through multi-panel structures lined with elastic porous materials. *Journal of Sound and Vibration*, 191(3):317–347, 1996.

[11] C. Boutin, P. Royer, and J.-L. Auriault. Acoustic absorption of porous surfacing with dual porosity.. *Special Issue on poroelasticity, International Journal of Solids and Structures*, 35, 1998.

[12] B. Brouard, D. Lafarge, and J.-F. Allard. A general method of modeling sound propagation in layered media. *Journal of Sound and Vibration*, 183(1):129–142, 1995.

[13] Y. Champoux. *Etude expérimentale du comportement acoustique des matériaux poreux à structure rigide.* Ph.D. thesis, Carleton Univeristy, Canada, 1991.

[14] Y. Champoux and J.-F. Allard. Dynamic tortuosity and bulk modulus in air-sturated porous media. *Journal of Applied Physics*, 70, 1991.

[15] L. Codecasa and F. Trevisan. Constitutive equations for discrete electromagnetic problems over polyhedral grids. *Journal of Computational Physics*, 225, 2007.

[16] F. Cosmi. Numerical solution of plane elasticity problems with the cell method. *Computer Modelling in Engineering and Science*, 2(3):365–372, 2001.

[17] L. De Ryck, Groby J.P., P. Leclaire, W. Lauriks, A. Wirgin, C. Depollier, and Z.E.A. Fellah. Acoustic wave propagation in a macroscopically inhomogeneous porous medium saturated by a fluid. *Applied Physics Letters*, 90(18):181–201, 2007.

[18] P. Debergue, R. Panneton, and N. Atalla. Boundary conditions for the weak formulation of the mixed (u,p) poroelasticity problem. *Journal of the Acoustical Society of America*, 106(5):2383–2390, 1999.

[19] E. Ferretti. Crack propagation modeling by remeshing using the cell method (cm). *Computer Modelling in Engineering and Science*, 4(1):51–72, 2003.

[20] D. Folds and C.D. Loggins. Transmission and reflection of ultrasonic waves in layered media. *Journal of the Acoustical Society of America*, 62(5):1102–1109, 1977.

[21] C. Glandier, R. Lehmann, T. Yamamoto, and Y. Kamada. Vibroacoustic FEA modeling of two layer trim systems. *Proceedings of SAE Conference 2005*, 2005.

[22] P. Göransson. A 3-D symmetric finite element formulation of the Biot equations with application to acoustic wave propagation through an elastic porous medium. *International Journal of Numerical Methods in Engineering*, 41, 1999.

[23] E. Gourdon and M. Seppi. Modelling acoustical heterogeneous materials composed of porous inclusions. *SAPEM*, 2008.

[24] J.-P. Groby, A. Wirgin, L. de Ryck, and W. Lauriks. Acoustic response of a rigid frame porous medium slab with a periodic set of inclusions. *Journal of Sound and Vibration*, arXiv:0705.2754v1, 2007.

[25] M. Heshmatzadeh and G.E. Bridges. A geometrical comparison between cell method and finite element method in electrostatics. *Computer Modelling in Engineering and Science*, 18(1):45–58, 2007.

[26] N.E. Hörlin. 3D hierarchical hp-FEM applied to elasto-acoustic modelling of layered porous media. *Journal of Sound and Vibration*, 285(1-2):341–363, 2005.

[27] N.E. Hörlin, M. Nordström, and P. Göransson. A 3-D hierarchical FE formulation of Biot's equations for elasto-acoustic modeling of porous media. *Journal of Sound and Vibration*, 245(4):633–652, 2001.

[28] K.V. Horoshenkov. Innovative applications of materials for acoustic purposes. *Applied Acoustics*, 66(6):603–605, 2005.

[29] D.L. Johnson, J. Koplik, and R. Dashen. Theory of dynamic permeability and tortuosity in fluid-saturated porous media. *Journal of Fluid Mechanics*, 1987.

[30] Y.J. Kang and J.S. Bolton. Finite element modeling of isotropic elastic porous materials coupled with acoustical finite elements. *Journal of the Acoustical Society of America*, 98(1):635–643, 1995.

[31] Y.J. Kang and J.S. Bolton. A finite element model for sound transmission through foam-lined double panel structures. *Journal of the Acoustical Society of America*, 99(5):2755–2765, 1996.

[32] Zovatto L. and Nicolini M. Improving the convergence order of the meshless approach for the cell method for numerical integration of discrete conservation laws. *International Journal for Computational Methods in Engineering Science and Me-*

chanics, 8(5):273–281, 2007.

[33] Zovatto L. and M. Nicolini. Extension of the meshless approach for the cell method to three-dimensional numerical integration of discrete conservation laws. *International Journal for Computational Methods in Engineering Science and Mechanics*, 7(2):69–79, 2006.

[34] D. Lafarge, P. Lemarinier, J.-F. Allard, and V. Tarnow. Dynamic compressibility of air in porous structures at audible frequencies. *Journal of the Acoustical Society of America*, 102(4):1995–2006, 1997.

[35] C. Langlois, R. Panneton, and N. Atalla. Polynomial relations for quasi-static mechanical characterization of isotropic poroelastic materials. *Journal of the Acoustical Society of America*, 110(6):1995–2006, 2001.

[36] R. Lanoye. Assessment of the absorption performance of sound absorbing materials: use of the trefftz's method and of a new dual particle velocity-pressure sensor. *Ph.D. thesis, Katholieke Universiteit Leuven, Belgium*, 2007.

[37] W. Lauriks, P. Mees, and J.F. Allard. The acoustic transmission through layered systems. *Journal of Sound and Vibration*, 155(1):125–132, 1992.

[38] C. Mattiussi. An analysis of finite volume, finite element, and finite difference methods using some concepts from algebraic topology. *Journal of Computational Physics*, 133, 1997.

[39] X. Olny. *Acoustic absorption of porous media with single and double porosity-modeling and experimental solution (in french).* Ph.D. thesis, ENTPE-Institut National des Sciences Appliquées de Lyon, France, 1999.

[40] X. Olny and C. Boutin. Acoustic wave propagation in double porosity media. *Journal of the Acoustical Society of America*, 114(1):73–89, 2003.

[41] X. Olny, R. Panneton, and J. Tran-Van. An indirect acoustical method for determining intrinsic parameters of porous materials. *Proc. of the Second Biot Conference on Poromechanics*, 2002.

[42] M. Pani, N. Zanette, and D. Battelino. Use of the cell method for plane elastic problems in geotechnique. *Computational Materials Science*, 26, 2003.

[43] R. Panneton and N. Atalla. Numerical prediction of sound transmission through finite multilayer systems with poroelastic material. *Journal of the Acoustical Society*

of America, 100(1):346–354, 1996.

[44] R. Panneton and N. Atalla. An efficient finite element scheme for solving the three-dimensional poroelasticity problem in acoustics. *Journal of the Acoustical Society of America*, 101(6):3287–3298, 1997.

[45] R. Panneton, N. Atalla, and J.F. Allard. A 3-d finite element model for sound transmission through a double-plate system with isotropic elastic porous materials. *Journal of the Acoustical Society of America*, 96, 1994.

[46] G. Pispola, K.V. Horoshenkov, and A. Khan. Comparison of two modeling approaches for highly heterogeneous porous media. *Journal of the Acoustical Society of America*, 121(2):961–966, 2007.

[47] S. Rigobert, F. Sgard, and N. Atalla. Investigation of the convergence of the mixed displacement-pressure formulation for three-dimensional poroelastic materials using hierarchical elements. *Journal of the Acoustical Society of America*, 114(5):2607–2617, 2003.

[48] S. Rigobert, F. Sgard, and N. Atalla. A two-field hybrid formulation for multilayers involving poroelastic, acoustic and elastic materials. *Journal of the Acoustical Society of America*, 115(6):2786–2797, 2004.

[49] F.C. Sgard, X. Olny, N. Atalla, and F. Castel. On the use of perforations to improve the sound absorption of porous materials. *Applied Acoustics*, 66, 2005.

[50] B.H. Song and J.S. Bolton. A transfer-matrix approach for estimating the characteristic impedance and wave numbers of limp and rigid porous materials. *Journal of the Acoustical Society of America*, 107(3):1131–1152, 2000.

[51] F. Taddei, M. Pani, L. Zovatto, E. Tonti, and M. Viceconti. A new meshless approach for subject-specific strain prediction in long bones: Evaluation of accuracy. *Clinical Biomechanics*, 23(9):1192–1199, 2008.

[52] V. Tarnow. Airflow resistivity of models of fibrous acoustic materials. *Journal of the Acoustical Society of America*, 100(6):3706–3713, 1996.

[53] E. Tonti. A direct discrete formulation for the wave equation. *The 4th Int. Conference on Theoretical and Computational Acoustics*, 1999.

[54] E. Tonti. A direct discrete formulation of field laws: the Cell Method. *Computer Modelling in Engineering and Science*, 2(2):237–258, 2001.

[55] E. Tonti. Finite formulation of the electromagnetic field. *Progress In Electromagnetics Research*, 32, 2001.

[56] N. Vosoughi, A.A. Salehi, and M. Shahriari. Discrete formulation for two-dimensional multigroup neutron diffusion equations. *Annals of Nuclear Energy*, 31, 2004.

[57] A. Yavari. On geometric discretization of elasticity. *Journal of Mathematical Physics*, 49, 2008.

[58] C. Zhang, M.A. Hamdi, L. Mebarek, and B. Mahieux. Influence of porous elastic components on structure and airborne noise in low and medium frequency ranges. *Proceedings of Rieter Automotive Conference 2005*, 2005.

[59] L. Zovatto and M. Nicolini. The meshless approach for the Cell Method: a new way for the numerical solution of the discrete conservation laws. *International Journal of Computational Engineering Science*, 4(4):869–880, 2003.

List of figures

List of tables